

Ph.D, Thesis

**The studies on synthesis and photocatalytic reactions
of N₂ molecule-intercalated mesoporous WO₃**

Dong Li

Doctoral Program in Advanced Materials Science and Technology

Graduate School of Science and Technology

Niigata University

-2015-

The studies on synthesis and photocatalytic reactions of N₂ molecule-intercalated mesoporous WO₃

Contents

Chapter 1 Introductory remarks

1.1 Background and purpose research	... 1
1.2 Contents of research	...2
1.3 Reference	... 5

Chapter 2 Facile and simple fabrication of an efficient nanoporous WO₃ photoanode for visible-light-driven water splitting

2.1 Introduction	... 11
2.2 Experimental section	... 13
2.3 Results and Discussion	... 15
2.4 Conclusion	... 21
2.5 Acknowledgement	... 21
2.6 Reference	... 21

Chapter 3 Unique and facile solvothermal synthesis of mesoporous WO₃ using a solid precursor and a surfactant template as a photoanode for visible-light-driven water oxidation

3.1 Background	...36
3.2 Methods	...38
3.3 Results	... 41
3.4 Conclusion	... 46
3.5 Competing interests	... 46
3.6 Authors'contributions	... 46
3.7 Acknowledgments	... 47
3.8 Reference	... 47

Chapter 4 Unique synthesis of mesoporous WO₃ by in-situ N₂ intercalation from surfactant template : Photoanode for Visible-light-driven water oxidation

4.1 Introduction	... 63
4.2 Experimental section	... 66
4.3 Results and Discussion	... 70

4.4	Conclusion	...79
4.5	Reference	... 79
 Chapter 5 Nanorod architecture of N₂-intercalated WO₃ operated in wide-range of visible-light for highly efficient photocatalytic and photoelectrochemical water oxidation		
5.1	Introduction	... 109
5.2	Experimental section	... 111
5.3	Results and Discussion	... 113
5.4	Reference	... 120
 Chapter 6 Stoichiometric Photoisomerization of Mononuclear Ruthenium(II) Monoaquo Complexes Controlling Redox Properties and Water Oxidation Catalysis		
6.1	Introduction	... 140
6.2	Experimental section	... 142
6.3	Results and Discussion	... 145
6.4	Reference	... 159
 Concluding remarks		...187
 Acknowledgments		... 190
 Appendixes		
Publication list		...191
Intercalation conference		... 192

Chapter 1 Introductory remarks

1.1 Background and purpose of research

Energy and environment issues have become significant topics that are discussed around the world. Hydrogen which is identified as an environmental friendliness and renewable fuel has been produce and expected to solve the issues. Recently, more and more attentions have been devoted to construct an artificial photosynthesis system, in which hydrogen fuel and oxygen will be produced from water by conversing abundant solar light directly.¹⁻⁵ Since development of robust catalysts with high efficient for water oxidation ($2\text{H}_2\text{O} \rightarrow \text{O}_2 + 4\text{H}^+ + 4\text{e}^-$) is considering as the key task, until now numerous organic complex catalysts^{6,7} and also such materials with narrow bandgaps including tungsten trioxide (WO_3)⁸⁻¹⁸ as photocatalysts (Figure 1-1) or photoanodes in photoelectrochemical (PEC) cell (Figure 1-2) have been reported for water oxidation.

WO_3 , an n-type semiconductor, has attracted immense attention as photocatalyst¹⁹⁻²² materials and photoanode materials in PEC cells^{8,23-29} for water oxidation because of its visible light response (bandgap, $E_g = 2.6$ to 2.8 eV), a valence band edge position thermodynamically possible for water oxidation (about 3 V versus the normal hydrogen electrode), strong absorption within solar spectrum and good photochemical stability under the acidic conditions,^{8,17,20,23,28,30-33} however, pure WO_3 exhibits low photocatalytic activity under visible light irradiation due to either its fast recombination of electron-hole pairs or high band gap which restrict from sufficient strong visible region absorption of solar spectrum. Herein, the purpose of the present research for my doctoral dissertation is that I focus on WO_3 towards improvement of the PEC water oxidation performance by fabrication of mesoporous structured WO_3 to

increase the surface area which offers a large number of water oxidation sites at the electrolyte-WO₃ interface to suppress the recombination chance of electron-hole pairs or by intercalation of nitrogen (N₂) molecule into the WO₃ lattice to lower the absorption threshold of WO₃.

1.2 Contents of research

In the second chapter, Tungsten trioxide (WO₃) films with nanoporous morphology were prepared by a facile and simple method utilizing commercially available WO₃ nanopowder with polyethylene glycol to guide porosity of a nanostructure, and the resulted photoanode was working efficiently for visible-light-driven water oxidation. The SEM observation and XRD measurement revealed formation of interparticulate nanopores between the well-connected WO₃ crystalline particles of dimension ca. 100-200 nm. The nanoporous WO₃ electroode generated a significant photoanodic current density of 1.8 mA cm⁻² due to water oxidation at 1.0 V versus Ag/AgCl on visible light irradiation ($\lambda > 390$ nm, 100 mW cm⁻²). The onset potential of the WO₃ electroode was 0.67 V versus a reversible hydrogen electrode (RHE), being lower by 0.56 V than the theoretical potential for water oxidation (1.23 V versus RHE). The incident photon to current conversion efficiency (IPCE) reached 45% at 400 nm of light wavelength and 1.04 V versus Ag/AgCl of an applied potential. The photoanodic current and photostability of the WO₃ electrode were improved by addition of Co²⁺ ions in the electrolyte solution during photoelectrocatalysis.

In the third chapter, Mesoporous tungsten trioxide (WO₃) was prepared from

tungstic acid (H_2WO_4) as a tungsten precursor with dodecylamine (DDA) as a template to guide porosity of the nanostructure by a solvothermal technique. The WO_3 sample (denoted as WO_3 -DDA) prepared with DDA was moulded on an electrode to yield efficient performance for visible-light-driven photoelectrochemical (PEC) water oxidation. Powder X-ray diffraction (XRD) data of the WO_3 -DDA sample calcined at $400\text{ }^\circ\text{C}$ indicate a crystalline framework of the mesoporous structure with disordered arrangement of pores. N_2 physisorption studies show a Brunauer-Emmett-Teller (BET) surface area up to $57\text{ m}^2\text{ g}^{-1}$ together with type IV isotherms and uniform distribution of a nanoscale pore size in the mesopore region. Scanning electron microscopy (SEM) images exhibit well-connected tiny spherical WO_3 particles with a diameter of *ca.* 5 to 20 nm composing the mesoporous network. The WO_3 -DDA electrode generated photoanodic current density of 1.1 mA cm^{-2} at 1.0 V versus Ag/AgCl under visible light irradiation, which is about three times higher than that of the untemplated WO_3 . O_2 ($1.49\text{ }\mu\text{mol}$; Faraday efficiency, 65.2%) was evolved during the 1-h photoelectrolysis for the WO_3 -DDA electrode under the conditions employed. The mesoporous electrode turned out to work more efficiently for visible-light-driven water oxidation relative to the untemplated WO_3 electrode.

In the fourth chapter, I report herein that a unique N_2 -intercalated WO_3 with a mesoporous structure was first succeed to synthesize by employing an facile one-step hydrothermal treatment procedure using dodecylamine (DDA), which was used as an nitrogen source as well as a surfactant template for formation of mesoporous structure. At first, I optimized the preparation condition including the amount of DDA and

hydrothermal preparation temperature (150°C) by N₂ physisorption experiment. And I investigated the calcination temperature-dependent experiments on XRD, EDS, Raman further comparing to the second chapter. The XRD data of N₂-intercalated WO₃ prepared with DDA exhibited higher crystallinity compared to WO₃-bulk which prepared without DDA. The existence of nitrogen element was detected from EDS and Raman results. The N₂-intercalated mesoporous WO₃ exhibit that this photoanode material was responsive to visible light of $\lambda \leq 490$ nm, which is corroborated the optical band gap (2.5 eV). This band gap of N₂-intercalated mesoporous WO₃ is narrower compared to the controlled materials (2.8 eV) prepared without a template. And also the performance of PEC water oxidation was improved. The action spectra of incident photon-to-current conversion efficiency (IPCE) exhibited that the photoanodic current of N₂-intercalated mesoporous WO₃ was generated below 490 nm for the N₂-WO₃ electrodes.

In the fifth chapter, a N₂-intercalated WO₃ (N₂-WO₃) having nano-rod structure was prepared from hydrazine-derived precursor which was synthesized from tungsten acid (H₂WO₄) and hydrazine solution (N₂H₄) as N₂ source instead of NH₃ H₂O at room temperature. An N₂-WO₃-coated electrode was prepared by simple squeeze of WO₃ paste over ITO substrates. XRD and Raman spectra suggested formation of pure monoclinic WO₃ phase and intercalation of N₂ into the WO₃ lattice. UV-visible spectra showed red shift of an absorption band edge due to N₂ intercalation, suggesting the possibility of improved visible light response. Under visible light irradiation, remarkable high O₂ evolution were observed for hydrazine-derived

N₂-WO₃ both calcined at 420°C (0.89 □ mol h⁻¹) and 550°C (3.52 □ mol h⁻¹). Under visible light irradiation significant high anodic photocurrent (1.2 mA cm⁻² at 1.0 V, 100 mW cm⁻² light intensity) was detected on cyclic voltammograms (CV) for hydrazine-derived N₂-WO₃ calcined at 420°C. This current is about 4 times higher than that of ammonium-derived N₂-WO₃ (0.3 mA cm⁻² at 1.0 V). The action spectra of incident photon-to-current conversion efficiency (IPCE) exhibited that the photoanodic current was generated below 520 nm for the N₂-WO₃ electrodes. High charge generation and large amounts of O₂ evolved with high Faradaic efficiency during photoelectrocatalysis at the N₂-WO₃ electrode were observed.

In the sixth chapter, a nanorod-structured N₂-intercalated WO₃ (N₂-WO₃) was prepared from hydrazine-derived precursor using the same procedure with the second chapter. Amount of hydrazine-dependent and calcination temperature-dependent were discussed further than the second chapter. For comparison, a N₂-intercalated WO₃ was prepared from ammonium-derived precursor which was synthesized from H₂WO₄ and ammonium solution (NH₃ H₂O) as N₂ source³⁴. Also, the a control sample was prepared from peroxo-tungstic acid (PTA) according to the method report previously³⁵

1.3 Reference

- (1) Chen, X.; Shen, S.; Guo, L.; Mao, S. S. *Chem. Rev.* **2010**, *110*, 6503.
- (2) Kamat, P. V.; Tvrđy, K.; Baker, D. R.; Radich, J. G. *Chem. Rev.* **2010**, *110*, 6664.
- (3) Lewis, N. S.; Nocera, D. G. *Proc. Natl. Acad. Sci.* **2006**, *103*, 15729.
- (4) Bard, A. J.; Fox, M. A. *Acc. Chem. Res.* **1995**, *28*, 141.

- (5) Kudo, A.; Miseki, Y. *Chem. Soc. Rev.* **2009**, 38, 253.
- (6) Yamazaki, H.; Shouji, A.; Kajita, M.; Yagi, M. *Coord. Chem. Rev.* **2010**, 254, 2483.
- (7) Dau, H.; Zaharieva, I. *Acc. Chem. Res.* **2009**, 42, 1861.
- (8) Chandra, D.; Saito, K.; Yui, T.; Yagi, M. *Angew. Chem. Int. Ed.* **2013**, 52, 12606.
- (9) Satsangi, V.; Kumari, S.; Singh, A.; Shrivastav, R.; Dass, S. *Int. J. Hydrogen Energy* **2008**, 33, 312.
- (10) Rahman, G.; Joo, O.-S. *Int. J. Hydrogen Energy* **2012**, 37, 13989.
- (11) Li, Y.; Takata, T.; Cha, D.; Takanabe, K.; Minegishi, T.; Kubota, J.; Domen, K. *Adv. Mater.* **2013**, 25, 125.
- (12) Maeda, K.; Higashi, M.; Lu, D.; Abe, R.; Domen, K. *J. Am. Chem. Soc.* **2010**, 132, 5858.
- (13) Maeda, K.; Domen, K. *Angew. Chem. Int. Ed.* **2012**, 51, 9865.
- (14) Abe, T.; Nagai, K.; Kabutomori, S.; Kaneko, M.; Tajiri, A.; Norimatsu, T. *Angew. Chem. Int. Ed.* **2006**, 45, 2778.
- (15) Abe, R.; Takata, T.; Sugihara, H.; Domen, K. *Chem. Commun.* **2005**, 3829.
- (16) Hisatomi, T.; Dotan, H.; Stefiik, M.; Sivula, K.; Rothschild, A.; Grätzel, M.; Mathews, N. *Adv. Mater.* **2012**, 24, 2699.
- (17) Chatchai, P.; Murakami, Y.; Kishioka, S.-y.; Nosaka, A. Y.; Nosaka, Y. *Electrochim. Acta* **2009**, 54, 1147.
- (18) Kim, H. G.; Borse, P. H.; Jang, J. S.; Ahn, C. W.; Jeong, E. D.; Lee, J. S. *Adv.*

Mater. **2011**, *23*, 2088.

(19) Kominami, H.; Yabutani, K.-i.; Yamamoto, T.; Kera, Y.; Ohtani, B. *J. Mater. Chem.* **2001**, *11*, 3222.

(20) Miseki, Y.; Kusama, H.; Sugihara, H.; Sayama, K. *J. Phys. Chem. Lett.* **2010**, *1*, 1196.

(21) Ma, S. S. K.; Maeda, K.; Abe, R.; Domen, K. *Energy Environ. Sci.* **2012**, *5*, 8390.

(22) Martin, D. J.; Reardon, P. J. T.; Moniz, S. J. A.; Tang, J. *J. Am. Chem. Soc.* **2014**, *136*, 12568.

(23) Yagi, M.; Maruyama, S.; Sone, K.; Nagai, K.; Norimatsu, T. *J. Solid State Chem.* **2008**, *181*, 175.

(24) Li, D.; Chandra, D.; Saito, K.; Yui, T.; Yagi, M. *Nanoscale Res. Lett.* **2014**, *9*, 542.

(25) Pihosh, Y.; Turkevych, I.; Mawatari, K.; Asai, T.; Hisatomi, T.; Uemura, J.; Tosa, M.; Shimamura, K.; Kubota, J.; Domen, K.; Kitamori, T. *Small* **2014**, *10*, 3692.

(26) Kalanur, S. S.; Hwang, Y. J.; Chae, S. Y.; Joo, O. S. *J. Mater. Chem.* **2013**, *1*, 3479.

(27) Wang, G.; Ling, Y.; Wang, H.; Yang, X.; Wang, C.; Zhang, J. Z.; Li, Y. *Energy Environ. Sci.* **2012**, *5*, 6180.

(28) Seabold, J. A.; Choi, K.-S. *Chem. Mater.* **2011**, *23*, 1105.

(29) Hill, J. C.; Choi, K.-S. *J. Phys. Chem. C* **2012**, *116*, 7612.

(30) Kim, J.; Shin, K.; Cho, S.; Lee, T.-W.; Park, J. *Energy Environ. Sci.* **2011**, *4*,

1465.

(31) Yang, B.; Zhang, Y.; Drabarek, E.; Barnes, P.; Luca, V. *Chem. Mater.* **2007**, *19*, 5664.

(32) Miseki, Y.; Fujiyoshi, S.; Gunji, T.; Sayama, K. *Catal. Sci. Tech.* **2013**, *3*, 1750.

(33) Santato, C.; Ulmann, M.; Augustynski, J. *J. Phys. Chem. B* **2001**, *105*, 936.

(34) Mi, Q.; Ping, Y.; Li, Y.; Cao, B.; Brunschwig, B. S.; Khalifah, P. G.; Galli, G. A.; Gray, H. B.; Lewis, N. S. *J. Am. Chem. Soc.* **2012**, *134*, 18318.

(35) Sayama, K.; Hayashi, H.; Arai, T.; Yanagida, M.; Gunji, T.; Sugihara, H. *Appl. Catal. B* **2010**, *94*, 150.

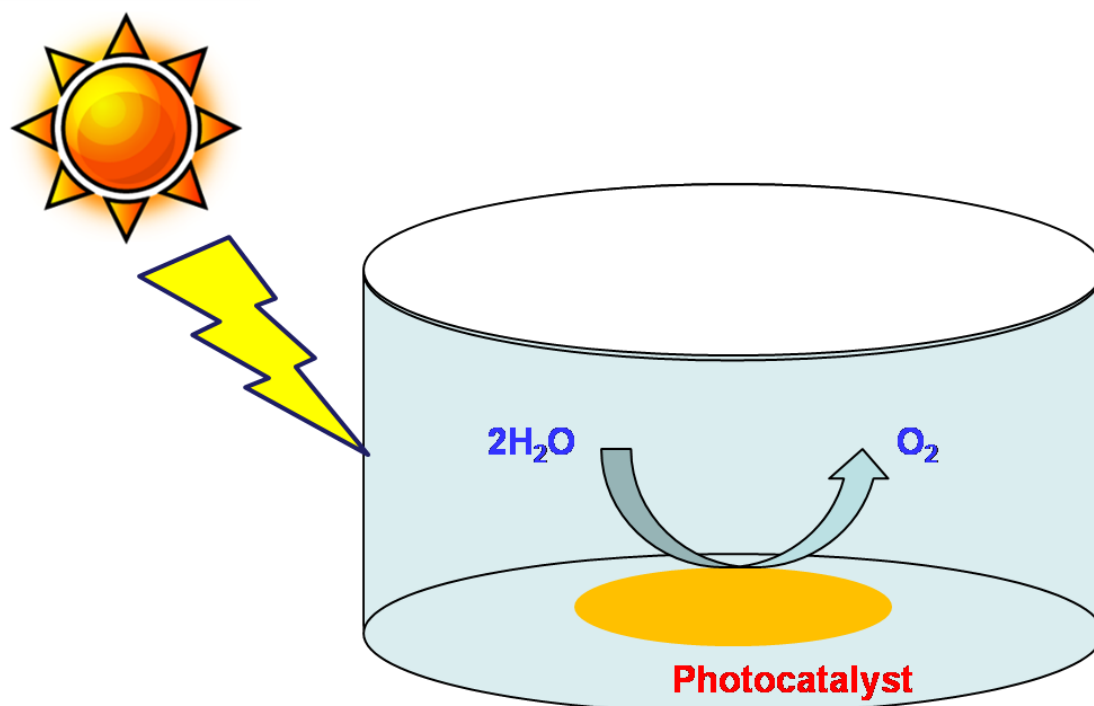


Figure 1-1 Solar oxygen production from water using a powdered photocatalyst.

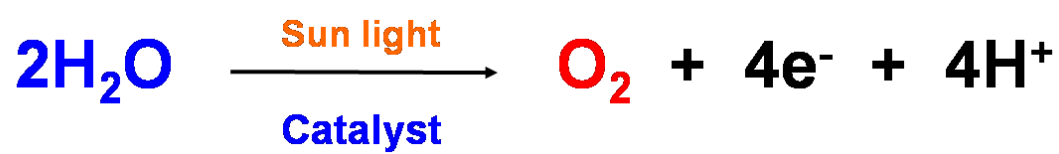
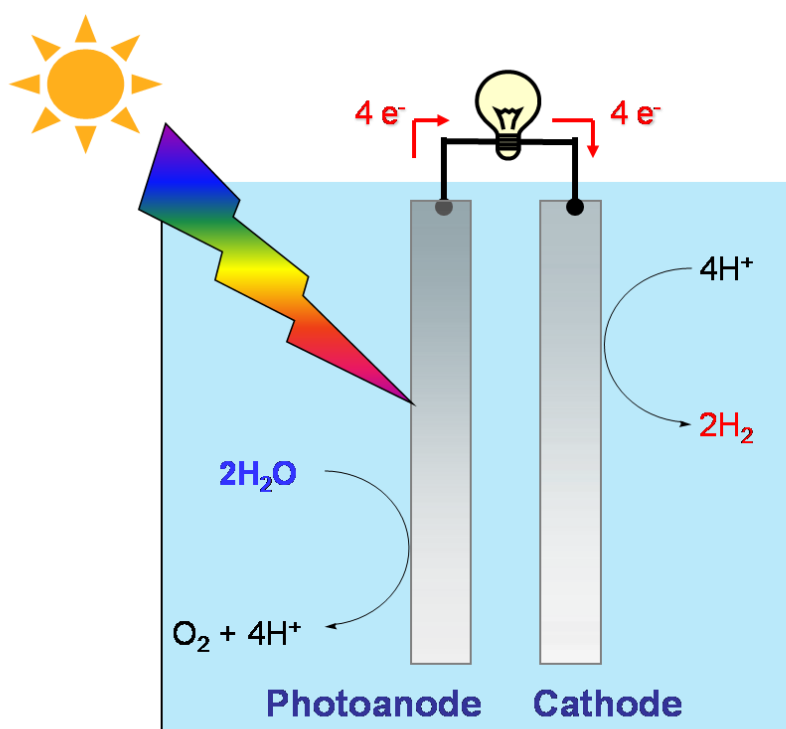


Figure 1-2 Reaction mechanism for photosynthesis system.

Chapter 2

**Facile and simple fabrication of an efficient
nanoporous WO₃ photoanode for visible-light-driven
water splitting**

Chapter 2

Facile and simple fabrication of an efficient nanoporous WO₃ photoanode for visible-light-driven water splitting

2.1 Introduction

Concern over climate change due to global warming becomes increasingly important, and in this regard hydrogen has featured prominently as a clean and renewable energy source.^[1-3] The conversion of solar energy into hydrogen represents an attractive but challenging alternative in photoelectrochemical (PEC) cells,^[4, 5] following the pioneer work on a TiO₂ photoanode for water splitting by Honda and Fujishima.^[6] Unfortunately a wide band gap of TiO₂ (3.0-3.2 eV) causes to absorb only an ultraviolet fraction of a solar spectrum (accounts for just 4% of solar irradiation) and consequently responsible for low efficiency in utilization of solar light.^[4, 7, 8] Therefore, intensive researches have been focused on materials with a relatively narrower band gap than TiO₂ to expand light absorption to a visible region. Several single component and composite materials (WO₃, Fe₂O₃, Ta₃N₅, TaON, BaZrO₃-BaTaO₂N, etc.) have been investigated to achieve efficient visible-light-driven water splitting.^[9-20]

WO₃, an n-type semiconductor has attracted immense attention as a photoanode material for water oxidation in PEC cells because of its visible light response (band gap, $E_g = 2.6-2.8$ eV), a thermodynamically possible valence band edge position for water oxidation (3 V versus the normal hydrogen electrode) and good photochemical stability under acidic conditions.^[9-12, 21-23] So far, several efforts for nanostructural control of WO₃ have been paid to increase a contact area between an electrode and electrolyte solution and to make electron transport in WO₃ layers

easier, intended for enhancing performance of PEC water oxidation at WO₃ electrodes.^[9, 11, 24-27]

WO₃ films have been prepared by several techniques, *e.g.*, vacuum evaporation^[28], chemical vapor deposition^[29, 30], sol-gel precipitation^[23-26, 31], spin coating^[32], sputtering^[33] and electrodeposition^[34-38]. The low-cost chemical procedure like a sol-gel technique is selected for a wide range of applications.^[23-26, 31] Santato *et al.* reported the preparation of a transparent crystalline WO₃ film with interconnected nanoparticulate structures by a spin-coat of the colloidal tungstic acid precursor solution (obtained by passing an aqueous solution of sodium tungstate through a proton exchange column) and followed by calcination under oxygen atmosphere at 550 °C.^[24-26] However, one needs to be proficient in preparation of the precursor solution involving a somewhat complicated procedure for reproducible fabrication of the WO₃ film. Sayama *et al.* reported the fabrication of a WO₃ film from an oxygen rich amorphous peroxo-tungstic acid precursor prepared using a relatively easy technique.^[39-41] Our aim is to develop a simple and reproducible fabrication technique for a WO₃ film without a complicated procedure of precursor preparation, which is beneficial for general researcher especially out of a chemistry field. Herein we report a facile, simple and low-cost method for the preparation of the nanoporous WO₃ film utilizing commercially available WO₃ nanopowder (instead of laboratory-made tungsten precursors) with polyethylene glycol (PEG) to guide porosity of a nanostructure. The high performance of photoelectrocatalytic water oxidation of the nanoporous WO₃ film is presented, and furthermore the photostability of the

nanoporous WO₃ electrode during photoelectrocatalysis is discussed.

2.2 Experimental section

Materials

Tungsten trioxide (WO₃) nanopowder (particle size, < 100 nm) was purchased from Aldrich. Polyethylene glycol (PEG, molecular weight = 2,000) was obtained from Wako Chemical Co. Marpolose (60MP-50) was purchased from Matsumoto Yushi-Seiyaku Co. An indium tin oxide (ITO)-coated glass substrate was obtained from Asahi Glass Co. Millipore water was used for all the experiments. All other chemicals unless mentioned otherwise were of analytical grade and used as received.

Preparation of electrodes

A nanoporous WO₃ film-coated ITO (ITO/WO₃) electrode was prepared by using a doctor-blade technique. Before coating, an ITO glass substrate (1.0 cm² area) was cleaned up by the UV-Ozone treatment (SEN LIGHTS Co., Photo Surface Processor PL16-110) for 15 min. In a typical procedure, 300 µL water was added to a mixture of 200 mg WO₃ nanopowder, 100 mg PEG and 20 mg marpolose. The mixture was stirred for 2~4 h until a smooth paste was formed. The resulting paste was squeezed over the ITO glass substrate by a doctor-blade coater and dried at 80 °C for 15 min. After repeating the procedure for 2 times, it was calcined at 550 °C for 90 min to obtain the nanoporous WO₃ film on the ITO glass substrate.

Structural characterization

The crystalline phase of the nanoporous WO₃ film was characterized by

powder X-ray diffraction (XRD; Rigaku, MiniFlexII) using monochromated Cu K α ($\lambda = 1.54 \text{ \AA}$) radiation. The nanoporous structure of the film was imaged by scanning electron microscopy (SEM; JEOL, JSM-6510LV), and prior to SEM observation the samples were gold-coated by sputtered deposition (Sanyu Electron, Quick Coater SC-701). UV-visible diffuse reflectance spectra (DRS) were recorded on a JASCO V-670 spectrophotometer.

Photoelectrochemical Measurements

Photoelectrochemical measurement was carried out in a two-compartment electrochemical cell separated by a Nafion membrane using an electrochemical analyzer (Hokuto, HZ-3000). A three-electrode system has been employed by using ITO/WO₃ and Ag/AgCl electrodes in one compartment as working and reference electrodes, respectively and a Pt wire in the other compartment as a counter electrode. An aqueous 0.1 M phosphate solution were used as an electrolyte in both the compartments, which was saturated with Ar gas prior to the electrochemical measurement. For the study on effect of Co²⁺ ions on the photoelectrocatalytic performance, 0.1 mM Co(NO₃)₂·6H₂O was contained in the electrolyte solution of the working electrode compartment. The cyclic voltammogram (CV) was recorded at a scan rate of 50 mV s⁻¹ at 25 °C under Ar atmosphere. Light ($\lambda > 390 \text{ nm}$) was irradiated from a backside of the working electrode using a 500 W xenon lamp (Ushio Inc., Optical ModuleX) with a UV-cut-filter (L39) and a liquid filter (0.2 M CuSO₄) for cutting of heat ray. The output of light intensity was calibrated as 100 mW cm⁻² using a spectroradiometer (Ushio Inc., USR-40). IPCE data were calculated using equation (1):

$$\text{IPCE (\%)} = [1241 \cdot I_p / (\lambda \cdot \varphi)] \times 100 \quad (1)$$

where I_p (mA cm^{-2}), λ (nm), and ϕ (mW cm^{-2}) denote photocurrent density recorded at given conditions, wavelength and intensity of incident photon, respectively. Monochromatic irradiation was carried out using a 500 W xenon lamp in combination with a monochromator (Jasco Corp., M10). Photoelectrocatalysis was conducted at 25 °C under the potentiostatic conditions of 0.5 V vs Ag/AgCl under illumination of light ($\lambda > 390$ nm; intensity 100 mW cm^{-2}) for 1 h. The amounts of H_2 and O_2 evolved were determined from the analysis of the gas phase (headspace volume: 87.3 mL) of counter and working electrode compartments, respectively using a gas chromatography (Shimadzu, GC-8A with a TCD detector and molecular sieve 5A column and Ar carrier gas).

2.3 Results and discussion

When a WO_3 film was prepared on the ITO substrate from only a dispersion of WO_3 nanopowder (200 mg) in water (3.0 ml), a reproducible film was not obtained due to low viscosity of the dispersion medium. In case of either PEG or marpolose (120 mg) included in the dispersion medium (200 mg WO_3 in 3.0 ml water) for preparation of a coating paste, the quality of the resulted WO_3 film was better than that prepared without PEG or marpolose but it was not sufficiently homonegeous. However, the use of both PEG (100 mg) and marpolose (20 mg) in the coating paste gave a highly reproducible and homogeneous WO_3 film exhibiting a significant photocurrent responce as discussed in the latter section. Marpolose helps to attach the coating paste on the ITO substrate by increasing viscosity of the dispersion medium, which is necessary to produce an uniform layer of coating by a doctor blade method. PEG acts as a binder between WO_3 particles as well as guides porosity of a

nanostructure.^[11] The organic additive is well-defined to play a role as a template for formation of various nanostructures of the metal oxides.^[11, 25, 42, 43]

The SEM images of the ITO/WO₃ film prepared under typical conditions and then calcined at 550 °C are shown in Fig. 1. The top-view of the SEM image at a low magnification (Fig. 1a) exhibits a flawless and smooth porous network, extended over several micrometer without any significant crack formation. The SEM image at higher magnification (Fig. 1b) shows that a nanoporous network is composed of embedded ball-like WO₃ particles of ca. 100-200 nm in diameters, being well-connected to each other. From the cross-sectional SEM image the film thickness was measured to be ca. 20 µm. The X-ray diffraction (XRD) patterns of the ITO/WO₃ film calcined at 200-600 °C are shown in Fig. 2. The films exhibited sharp and intense peaks for all the calcination temperatures employed due to preattainment with optimum crystallization of WO₃ nanopowders used in the coating paste. The *d*-spacings calculated from the corresponding peaks of the XRD patterns are in good agreement with phase-pure monoclinic WO₃ (JCPDS number: 43-1305). This crystalline nanoporous structure of the connected WO₃ particles is important to yield a large interface between the electrolyte and film and efficient electron transport through the film, which are consequently expected to work efficiently for PEC water oxidation since the electron and hole pairs generated by photoexcitation of WO₃ would have less chance to recombine before participating in a water oxidation reaction at the WO₃ surface.

The PEC water oxidation at the nanoporous ITO/WO₃ electrode (calcined at 550 °C) was studied in a 0.1 M phosphate solution. On cyclic voltammograms (CVs) at pH = 6.0 in the dark, no redox response was observed in a range of -0.2 ~ 1.0 V vs. Ag/AgCl except a response based on WO₃/H_xWO₃ below 0 V (black line in Fig. 3a). Upon visible light irradiation ($\lambda > 390$ nm, 100 mW cm⁻²) the significantly high

photoanodic current was observed above 0.12 V vs. Ag/AgCl and reached 1.76 mA cm⁻² at 1.0 V. The potential values of CV data were converted from Ag/AgCl to reversible hydrogen electrode (RHE) according to equation (2):

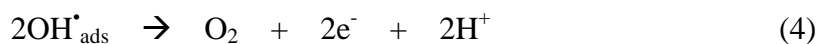
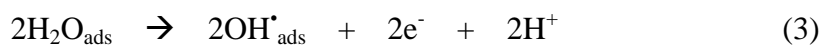
$$E_{\text{RHE}} = E_{\text{Ag/AgCl}} + (0.059 \times \text{pH}) + E^{\circ}_{\text{Ag/AgCl}} \quad (2)$$

where E_{RHE} is the calculated potential versus RHE, $E_{\text{Ag/AgCl}}$ is the measured potential vs Ag/AgCl and $E^{\circ}_{\text{Ag/AgCl}} = 0.199$ V at 25 °C. The onset potential of the nanoporous ITO/WO₃ electrode is 0.67 V versus RHE and it is lower by 0.56 V than the theoretical potential for water oxidation (1.23 V versus RHE). Fig. 3b shows the dependence of the generated photocurrent at 1.0 V vs. Ag/AgCl on the thickness of the nanoporous ITO/WO₃ electrode. The photocurrent increased up to 20 μm of the film thickness, showing that 20 μm of the WO₃ layer from the ITO interface is effective for the PEC reaction due to light penetration restriction. The photocurrent was measured by changing light intensity from 0 to 172 mW cm⁻² (Fig. 3c). It increased linearly with an increase in light intensity up to 100 mW cm⁻², indicating that the photocurrent generation is controlled by a photoexcitation process up to 100 mW cm⁻² light intensity. The downward deviation of the photocurrent from the linear relationship could be ascribed to controlled diffusion of the holes and electrons and/or a water oxidation reaction at the surface taking place after photoexcitation.

Action spectrum of IPCE for the nanoporous ITO/WO₃ electrode in a phosphate solution at pH = 6.0 and 1.04 V versus Ag/AgCl are shown in Fig. 4. The photocurrent was generated in a visible light region below 480 nm, and IPCE reached 45% at 400 nm. The edge of the action spectrum of IPCE agreed with a band gap energy of 2.64 eV (470 nm), estimated from the diffuse reflectance spectrum of the

WO₃ film (Fig. 4). This result indicates that the photocurrent is generated by band gap excitation of WO₃. The IPCE of the ITO/WO₃ electrode at 400 nm was measured to be 33 % and 42% at 0.5 V and 0.8 V versus Ag/AgCl respectively. The former IPCE value at 0.5 V is inferior to that of efficient small mesopore WO₃ film (43 % at 0.5 V)^[9], but significantly higher than those of interparticulate and bulk WO₃ films prepared from peroxo-tungstic acid precursors using a similar fabrication technique (16 and 6 % respectively at 0.5 V^[9]) The latter IPCE value at 0.8 V is comparable to that of macroporous 3D photonic crystal WO₃ films (40-45 % at 0.8 V)^[44].

The flat band potential of the nanoporous ITO/WO₃ electrode was estimated from the onset potential (E_{on}) of the photoanodic current at various pH of the electrolyte solution. Although WO₃ is known to be less stable in basic conditions,^[45] the reliably analyzable CV data of the ITO/WO₃ electrode were recorded even at pH = 10. E_{on} was defined as the intersection potential of the tangential lines of the initial photocurrent rise and x-axis of the potential in CV data. We can classify the E_{on} values into two groups, as shown in Fig. 5. In the first group, the plot of E_{on} versus pH gave straight line below pH = 8.0 with the slope of -69 mV/pH (close to -59 mV/pH), indicating that the the PEC reaction at the surface involves a proton-couple electron transfer reaction with nearly equivalents of electron and proton. Most likely, the water oxidation reaction at the surface could occur as represented in equation (3) and (4) involving adsorbed hydroxy radical species (OH[•]_{ads}).^[46]



where the subscript “ads” means adsorbed species on the WO₃ surface. In the second

group, the same plot above pH = 8.0 gave the straight line but the slope (-30 mV/pH) is low (as absolute value), indicating that the PEC reaction involves another process of 2 equivalents of electron per a proton, competing with the water oxidation reaction at the surface above pH = 8.

Photoelectrocatalysis over the nanoporous ITO/WO₃ electrode was conducted in a 0.1 M phosphate solution under the potentiostatic conditions at 0.5 V versus Ag/AgCl for 1 h upon visible light irradiation ($\lambda > 390$ nm, 100 mW cm⁻²). The photocurrent-time profile at pH = 6.0 (Fig. 6) exhibits an initial spike in the photocurrent upon illumination (related with the capacitance component at the solid-liquid interface), followed by a photocatalytic current. The photocurrent density at 1 min was 0.69 mA cm⁻², which decreased to 0.37 mA cm⁻² after 1 h. When defining the degree (r_{ps}) of photocurrent stability as the photocurrent ratio of 1 min to 1 h to evaluate stability of photoelectrocatalysis, the r_{ps} value at pH = 6 was 54%. The charge amount passed during the 1 h photoelectrocatalysis is 1.69 C and the amount (n_{O_2}) of O₂ evolved was 2.6 μ mol (59% Faradaic efficiency (FE_{O₂})), as summarized in Table 1. The performance of PEC water oxidation is lower than that ($n_{O_2} = 4.2$ μ mol, FE_{O₂} = 79%, $r_{ps} = 76\%$) for the small mesopore WO₃ film reported earlier^[9], but much higher than those of interparticulate WO₃ ($n_{O_2} = 0.9$ μ mol, FE_{O₂} = 61%, $r_{ps} = 22\%$) and bulk WO₃ ($n_{O_2} = 0.4$ μ mol, FE_{O₂} = 44%, $r_{ps} = 30\%$) prepared using a similar fabrication technique.^[9] The photocatalytic currents at pH = 3 and 9 for the nanoporous ITO/WO₃ electrode were lower than that at pH = 6 by 1.5 and 1.8 times at 1 min, respectively (Fig. 6c and d). n_{O_2} increased in a pH region from 3 to 6, although r_{ps} remains almost unchanged in this pH region, as shown in Fig. 7 (with nearly same FE_{O₂}, Table 1). The increase of n_{O_2} is ascribed to easier water oxidation according to Nernst equation as pH increases. n_{O_2} decreased drastically above pH = 7

concomitantly with decreases of r_{ps} and FE_{O_2} due to photocorrosion of WO_3 film under basic conditions,^[45] which is consistent with the mechanistic change in the proton-coupled PEC reactions in Figure 5.

The photocurrent decrease and low FE_{O_2} during photoelectrocatalysis at acidic and neutral conditions could be attributed to photo-oxidation of WO_3 by the accumulated holes to form inactive tungsten-peroxo adducts at the surface.^[22] We earlier reported that the photo-oxidation was suppressed by Co^{2+} ions in an electrolyte solution to enhance the performance of PEC water oxidation at the small mesopore WO_3 film.^[9] The similar enhancement effect by Co^{2+} ions in an electrolyte solution was reported for PEC water oxidation at a hematite photoanode.^[47] In the presence of 0.1 mM Co^{2+} ions in the phosphate buffer solution of pH = 6, the performance of PEC water oxidation at the nanoporous ITO/ WO_3 electrode was enhanced compared with those in the absence of Co^{2+} ions (Fig. 6a, Table 1). Consequently the amount of O_2 evolved (3.8 μ mol) was about 1.5 times higher compared with that (2.6 μ mol) in the absence of Co^{2+} ion. We do not have any evidence for the formation of either Co-Pi^[48] and CoO_x ^[49] catalysts during photoelectrocatalysis, as discussed in earlier report.^[9] This enhancement could be explained by acceleration of the water oxidation reaction at the WO_3 surface by Co^{2+} ions adsorbed, being predominant to the photo-oxidation of WO_3 . However, the performance of PEC water oxidation was not sufficiently improved by addition of Co^{2+} ions (r_{ps} = ~73%, FE_{O_2} = ~69%), when comparing with that (r_{ps} = ~95%, FE_{O_2} = 81%) under the same conditions for the small mesopore WO_3 photoanode reported earlier.^[9] The high photostability of the small mesopore WO_3

photoanode is attributed to low effective concentration of the accumulated holes at the surface caused by their high surface-to-volume ratio.

2.4 Conclusions

A nanoporous WO₃ film was prepared on an ITO electrode by a facile, simple and low cost method using commercial WO₃ nanopowder. PEG additive was used as a binder between the WO₃ particles and guided nanoporosity in the film composed of well-connected crystalline WO₃ particles of diameter ~100-200 nm. The WO₃ film worked efficiently as a photoanode for PEC water oxidation and the photoelectrocatalytic performance was further improved by addition of Co²⁺ ions in the electrolyte solution. The WO₃ film is available as a benchmark photoanode for water oxidation required for a PEC water splitting device because a reproducible film is easily prepared without a complicated procedure of precursor preparation, especially for general researcher out of a chemistry field.

2.5 Acknowledgment

This work was partially supported by the JST PRESTO program and Grant-in-Aid for Scientific Research (B) from the Ministry of Education, Culture, Sports, Science and Technology (No. 24350028). DC thanks JSPS for providing postdoctoral fellowship.

2.6 References

- (1) Lewis NS, Nocera DG. Powering the planet chemical challenges in solar energy utilization. PNAS 2006;103:15729-15735.

- (2) Cook TR, Dogutan DK, Reece SY, Surendranath Y, Teets TS, Nocera DG. Solar energy supply and storage for the legacy and nonlegacy world. *Chem Rev* 2010;110: 6474-6502.
- (3) Dahl S, Chorkendorff I. Solar-fuel generation: Towards practical implementation. *Nat Mater* 2012;11:100-101.
- (4) Gratzel M. Photoelectrochemical cell. *Nature* 2001; 414:338-344.
- (5) Minggu LJ, Wan Daud WR, Kassim MB. An overview of photocells and photoreactors for photoelectrochemical water splitting. *Int J Hydrogen Energy* 2010; 35:5233-5244.
- (6) Fujishima A, Honda K. Electrochemical photolysis of water at a semiconductor electrode. *Nature* 1972; 238:37-38.
- (7) Kudo A, Miseki Y. Facile fabrication of an efficient oxynitride TaON photoanode for overall water splitting into H₂ and O₂ under visible light irradiation. *Chem Soc Rev* 2009;38: 253-278.
- (8) Aprile C, Corma A, Garcia H. Enhancement of the photocatalytic activity of TiO₂ through spatial structuring and particle size control from subnanometric to submillimetric length scale. *PCCP* 2008;10:769-783.
- (9) Chandra D, Saito K, Yui T, Yagi M. Crystallization of tungsten trioxide having small mesopores: highly efficient photoanode for visible-light-driven water oxidation. *Angew Chem Int Ed* 2013;52:12606-12609.
- (10) Ng KH, Minggu LJ, Kassim MB. Gallium-doped tungsten trioxide thin film photoelectrodes for photoelectrochemical water splitting. *Int J Hydrogen Energy* 2013;38: 9585-9591.
- (11) Kim JK, Shin K, Cho SM, Lee T-W, Park JH. Synthesis of transparent mesoporous tungsten trioxide films with enhanced photoelectrochemical

- response: application to unassisted solar water splitting. *Energy Environ Sci* 2011;4:1465-1470.
- (12) Chatchai P, Murakami Y, Kishioka S-y, Nosaka AY, Nosaka Y. Efficient photocatalytic activity of water oxidation over WO₃/BiVO₄ composite under visible light irradiation. *Electrochim Acta* 2009;54:1147-1152.
 - (13) Hisatomi T, Dotan H, Stefik M, Sivula K, Rothschild A, Grätzel M, Mathews N. Enhancement in the performance of ultrathin hematite photoanode for water splitting by oxide underlayer. *Adv Mater* 2012;24:2699-2702.
 - (14) Satsangi VR, Kumari S, Singh AP, Shrivastav R, Dass S. Nanostructured hematite for photoelectrochemical generation of hydrogen. *Int J Hydrogen Energy* 2008;33:312-318.
 - (15) Rahman G, Joo O-S. Photoelectrochemical water splitting at nanostructured α -Fe₂O₃ electrodes. *Int J Hydrogen Energy* 2012;37:13989-13997.
 - (16) Li Y, Takata T, Cha D, Takanabe K, Minegishi T, Kubota J, Domen K. Vertically aligned Ta₃N₅ nanorod arrays for solar-driven photoelectrochemical water splitting. *Adv Mater* 2013;25:125-131.
 - (17) Maeda K, Higashi M, Lu D, Abe R, Domen K. Efficient nanosacrificial water splitting through two-step photoexcitation by visible light using a modified oxynitride as a hydrogen evolution photocatalyst. *J Am Chem Soc* 2010;132:5858-5868.
 - (18) Maeda K, Domen K. Water oxidation using a particular BaZrO₃-BaTaO₂N solid-solution photocatalyst that operates under a wide range visible light. *Angew Chem Int Ed* 2012;51:9865-9869.

- (19) Kim HG, Borse PH, Jang JS, Ahn CW, Jeong ED, Lee JS. Engineered nanorod perovskite film photocatalysts to harvest visible light. *Adv Mater* 2011;23:2088-2092.
- (20) Abe T, Nagai K, Kabutomori S, Kaneko M, Tajiri A, Norimatsu T. An organic photoelectrode working in the water phase: visible-light-induced dioxygen evolution by a perylene derivative/cobalt phthalocyanion bilayer. *Angew Chem Int Ed*. 2006;45:2778-2781.
- (21) Yang B, Zhang Y, Drabarek E, Barnes PRF, Luca V. Combinatorial development of nanoporous WO₃ thin film photoelectrodes for solar splitting by dealloying of binary alloys. *Chem Mater* 2007;19:5664-5672.
- (22) Seabold JA, Choi KS. Water splitting catalyst or spectator? *Chem Mater* 2011;23:1105-1112.
- (23) Yagi M, Maruyama S, Sone K, Nagai K, Norimatsu T. Preparation and photoelectrocatalytic activity of a nano-structured WO₃ platelet film. *J Solid State Chem* 2008;181:175-182.
- (24) Santato C, Ulmann M, Augustynski J. Photoelectrochemical properties of nanostructured tungsten trioxide films. *J phys chem B* 2001;105:936-940.
- (25) Santato C, Ulmann M, Augustynski J. Enhanced visible light conversion efficiency using nanocrystalline WO₃ film. *Adv Mater* 2001;13:511-514.
- (26) Santato C, Odziemkowski M, Ulmann M, Augustynski J. Photoelectrochemical water splitting using dense and aligned TiO₂ nanorod arrays. *J Am Chem Soc* 2001;123:10639-10649.
- (27) Berger S, Tsuchiya H, Ghicov A, Schmuki P. Electrical observations of filamentary conduction for the resistive memory switching in NiO films. *Appl Phys Lett* 2006;88:202102-1.

- (28) Colton RJ, Guzman AM, Rabalais JW. Electrochromism in some thin-film transition-metal oxides characterized by x-ray electron spectroscopy. *J Appl Phys* 1978;49:409-16.
- (29) Yous B, Robin S, Donnadieu A, Dufour G, Maillot C, Roulet H, Senemaud C. Chemical vapor deposition of tungsten oxides: A comparative study by X-ray photoelectron spectroscopy, X-ray diffraction and reflection high energy electron diffraction. *Mater Res Bull* 1984;19:1349-54.
- (30) Sivakumar R, Moses Ezhil Raj A, Subramanian B, Jayachandran M, Trivedi DC, Sanjeeviraja C. Preparation and characterisation of spray deposited n-type WO₃ thin films for electrochromic devices. *Mater Res Bull* 2004;39:1479-89.
- (31) Wang H, Lindgren T, He J, Hagfeldt A, Lindquist S-E. Photoelectrochemistry of nanostructured WO₃ thin film electrodes for water oxidation: Mechanism of electron transport. *J Phys Chem B*, 2000;104:5686-96.
- (32) Yamanaka K, Oakamoto H, Kidou H, Kudo T. Peroxotungstic Acid Coated Films for Electrochromic Display Devices. *Japan J Appl Phys* 1986;25:1420-6.
- (33) Le Bellac D, Azens A, Granqvist CG. Angular selective transmittance through electrochromic tungsten oxide films made by oblique angle sputtering. *Appl Phys Lett* 1995;66:1715-6.
- (34) Baeck S-H, Choi K-S, Jaramillo TF, Stucky GD, McFarland EW. Enhancement of Photocatalytic and Electrochromic Properties of Electrochemically Fabricated Mesoporous WO₃ Thin Films. *Adv Mater* 2003;15:1269-73.

- (35) Shen PK, Tseung ACC. Study of electrodeposited tungsten trioxide thin films. *J Mater Chem* 1992;2:1141-7.
- (36) Yagi M, Sone K, Yamada M, Umemiya S. Preparation and Multicolor Electrochromic Performance of a $\text{WO}_3/\text{Tris}(2,2'\text{-bipyridine})\text{ruthenium(II)}/\text{Polymer Hybrid Film}$. *Chem Eur J* 2005;11:767 – 75.
- (37) Yagi M, Umemiya S. Novel Preparation and Photoelectrochemical Properties of a Tungsten Oxide/ $\text{Tris}(2,2'\text{-bipyridine})\text{ruthenium(II)}$ Complex Composite Film. *J Phys Chem B* 2002;106:6355-7.
- (38) Sone K, Konishi K, Yagi M. Electrochromic Hysteresis Performance of a Prussian Blue Film Arising from Electron-Transfer Control by a $\text{Tris}(2,2'\text{-bipyridine})\text{ruthenium(II)}$ -Doped WO_3 Film as Studied by a Spectroscopic Voltammetry Technique. *Chem Eur J* 2006;12:8558 – 65.
- (39) Miseki Y, Kusama H, Sugihara H, Sayama K. Cs-Modified WO_3 Photocatalyst Showing Efficient Solar Energy Conversion for O_2 Production and Fe (III) Ion Reduction under Visible Light. *J Phys Chem Lett* 2010;1:1196–200.
- (40) Miseki Y, Fujiyoshi S, Gunji T, Sayama K. Photocatalytic water splitting under visible light utilizing I_3^-/I^- and IO_3^-/I^- redox mediators by Z-scheme system using surface treated PtOx/WO_3 as O_2 evolution photocatalyst. *Catal Sci Technol* 2013;3:1750-6.
- (41) Sayama K, Hayashi H, Arai T, Yanagida M, Gunji T, Sugihara H. Highly active WO_3 semiconductor photocatalyst prepared from amorphous peroxo-tungstic acid for the degradation of various organic compounds. *Appl Catal B* 2010;94:150-7.

- (42) Alexander BD, Kulesza PJ, Rutkowska I, Solarz R, Augustynski J. Metal oxide photoanodes for solar hydrogen production. *J Mater Chem* 2008;18:2298-303.
- (43) Meda L, Tozzola G, Tacca A, Marra G, Caramori S, Cristino V, Alberto Bignozzi C. Photo-electrochemical properties of nanostructured WO₃ prepared with different organic dispersing agents. *Sol Energy Mat Sol C*, 2010;94:788-96.
- (44) Chen X, Ye J, Ouyang S, Kako T, Li Z, Zou Z. Enhanced Incident Photon-to-Electron Conversion Efficiency of Tungsten Trioxide Photoanodes Based on 3D-Photonic Crystal Design. *ACS Nano* 2011;5 (6) :4310-8.
- (45) Greenwood NN, Earnshaw A. *Chemistry of the Elements* 2nd ed. Butterworth-Heinemann; 1998.
- (46) Leautic A, Babonneau F, Livage J. Photoreactivity of tungsten trioxide dispersions: spin trapping and electron spin resonance detection of radical intermediates. *J Phys Chem*. 1986;90:4193-8
- (47) Kay A, Cesar I, Grätzel M. New Benchmark for Water Photooxidation by Nanostructured α -Fe₂O₃ Films. *J Am Chem Soc*. 2006;128:15714-21.
- (48) Kanan M. W, Nocera D. G. In Situ Formation of an Oxygen-Evolving Catalyst in Neutral Water Containing Phosphate and Co²⁺. *Science* 2008; 321: 1072-75.
- (49) Higashi M, Domen K, Abe R. Fabrication of an Efficient BaTaO₂N Photoanode Harvesting a Wide Range of Visible Light for Water Splitting. *J Am Chem Soc*. 2013;135:10238-41.

Table 2-1. Summary of photoelectrocatalytic water oxidation at different pH using nanoporous ITO/WO₃ photoanodes in a 0.1M phosphate solution.

pH	Charge / C	n _{O2} / μmol	FE _{O2} ^a (%)	n _{H2} ^b / μmol	FE _{H2} ^c (%)	r _{ps} ^d (%)
3.0	1.03	1.7	65	4.7	88	56
4.0	1.12	1.7	59	5.0	87	53
5.0	1.37	2.1	59	6.3	89	52
6.0	1.69	2.6	59	7.4	85	54
6.0 ^e	2.14	3.8	69	9.5	86	74
7.0	1.38	2.3	64	6.3	88	41
8.0	1.37	1.8	50	6.1	86	27
9.0	0.61	0.52	33	2.7	85	18
10.0	0.56	0.64	44	2.5	87	7.6

^a Faradic efficiency of O₂ evolution

^b n_{H2} is the amount of H₂ evolved in the Pt counter electrode compartment.

^c Faradic efficiency of H₂ evolution

^d r_{ps} is a degree of photocurrent stability, calculated as the photocurrent ratio of 1 min to 1 h during photoelectrocatalysis.

^e Photoelectrocatalysis was conducted in the presence of 0.1 mM Co²⁺ ion in a 0.1 M phosphate solution

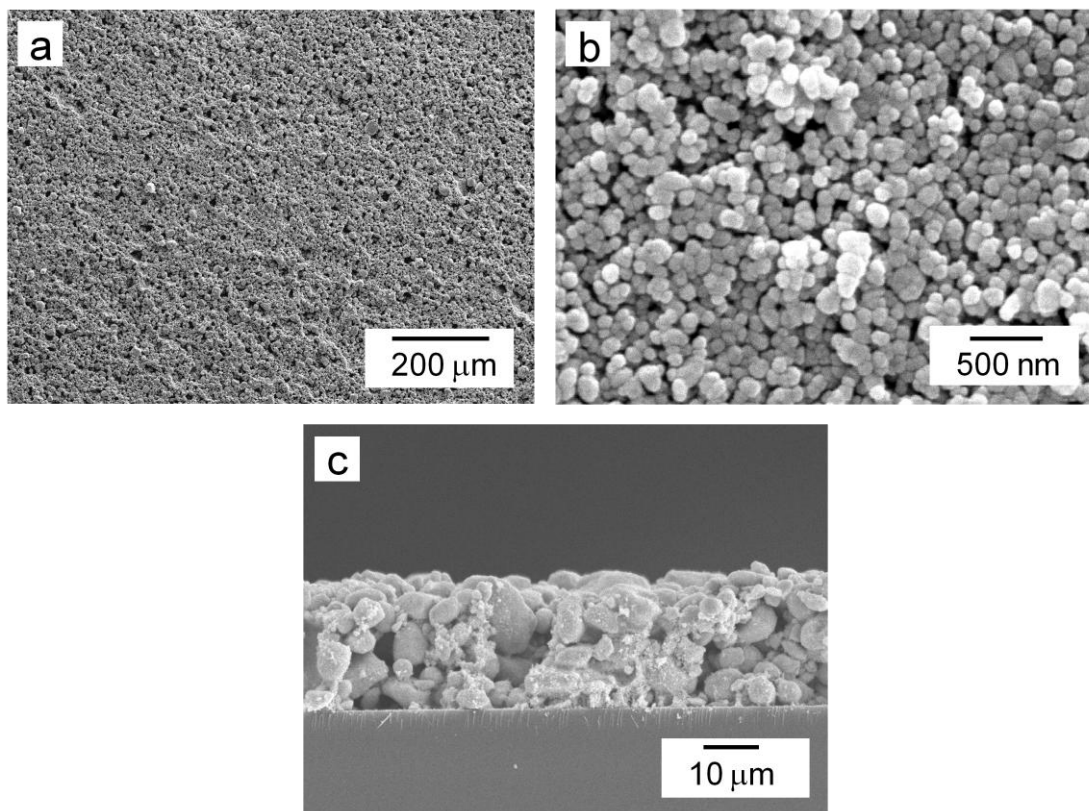


Figure 2-1. (a and b) Top view and (c) cross-sectional scanning electron microscopic (SEM) image of the nanoporous ITO/WO₃ electrode prepared under the typical conditions.

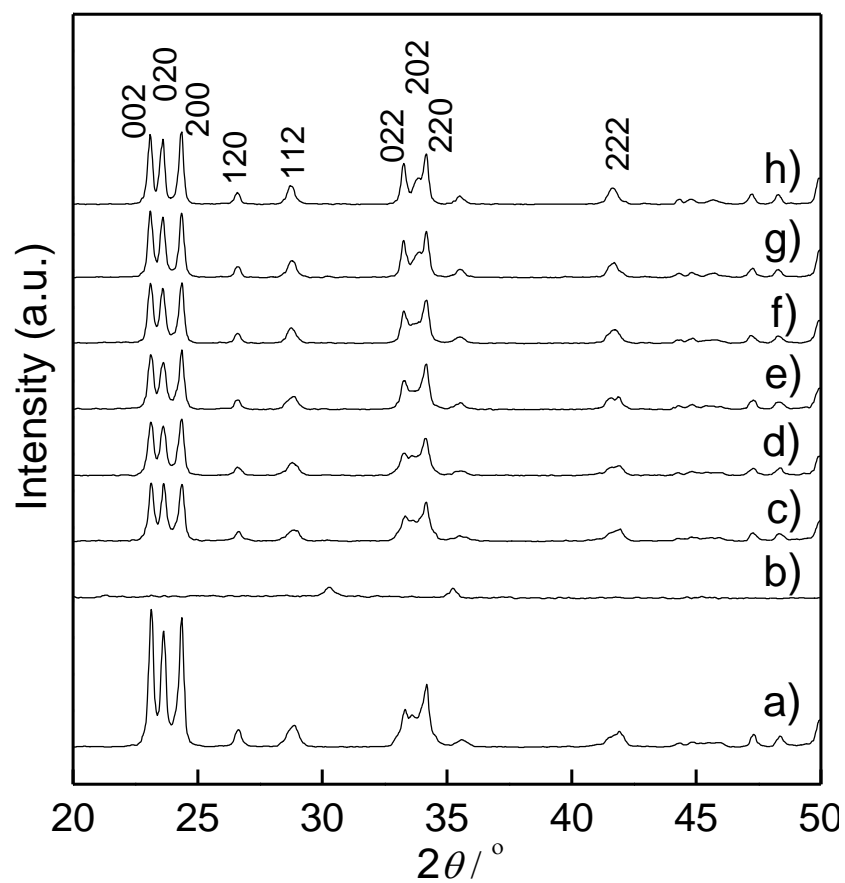


Figure 2-2. X-ray diffraction (XRD) patterns of (a) WO₃ nanopowder, (b) bare-ITO, and the WO₃ films calcined at (c) 25, (d) 200, (e) 300, (f) 400, (g) 500 and (h) 600 °C.

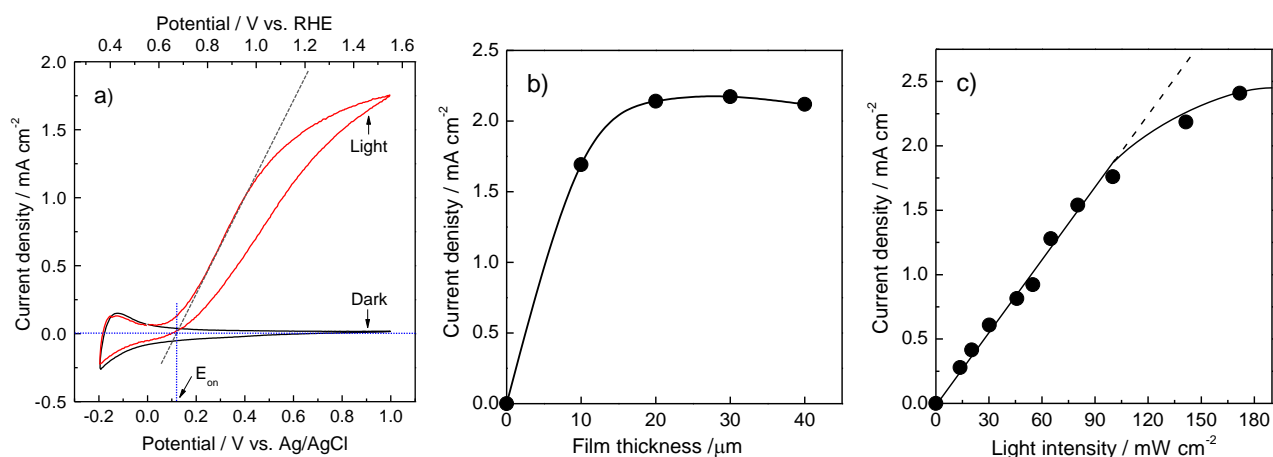


Figure 2-3. (a) Cyclic voltammograms (CVs), (b) plots of photocurrent density versus film thickness and (c) plots of photocurrent density versus light intensity for the nanoporous ITO/WO₃ electrode in a 0.1 M phosphate buffer solution of pH = 6.0. Visible light ($\lambda > 390$ nm, 100 mW cm^{-2}) was irradiated from an ITO substrate side. Photocurrent density at 1.0 V versus Ag/AgCl is used for plots in (b) and (c). CVs and plots of photocurrent density versus light intensity were measured using an ITO/WO₃ electrode of thickness 20 μm .

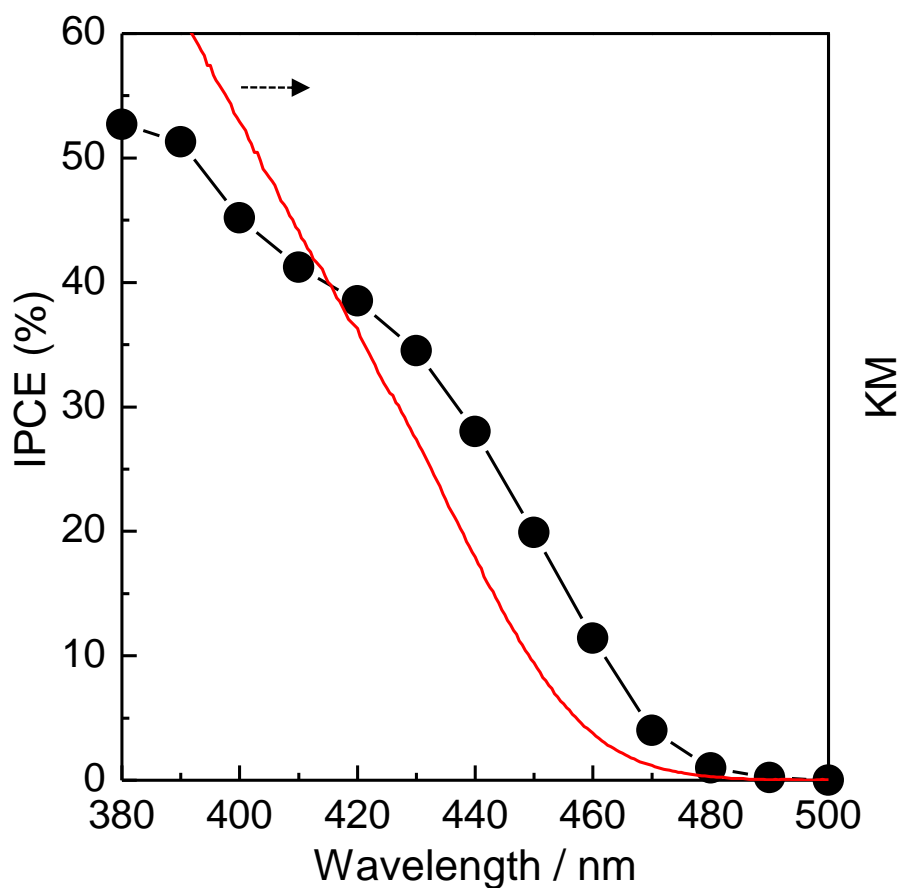


Figure 2-4. Action spectrum of IPCE (black line and symbols) for the nanoporous ITO/WO₃ electrode in a 0.1 M phosphate buffer solution of pH = 6.0 at 1.04 V vs. Ag/AgCl . The red line shows is UV-visible diffuse reflection spectra as Kubelka-Munk (KM) function of the nanoporous ITO/WO₃ electrode.

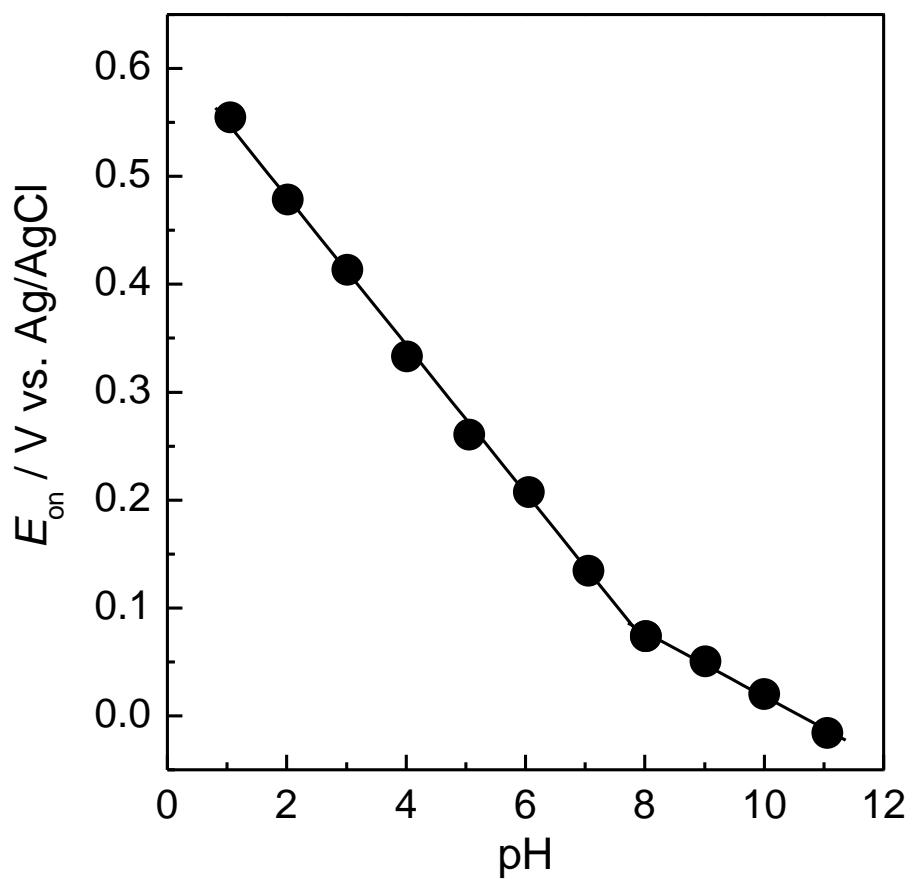


Figure 2-5. Plots of onset potential (E_{on}) versus pH for the nanoporous ITO/ WO_3 electrode in a 0.1 M phosphate solution. E_{on} was calculated as the intersection potential of the tangential lines of the initial photocurrent rise and x-axis of the potential in CV data .

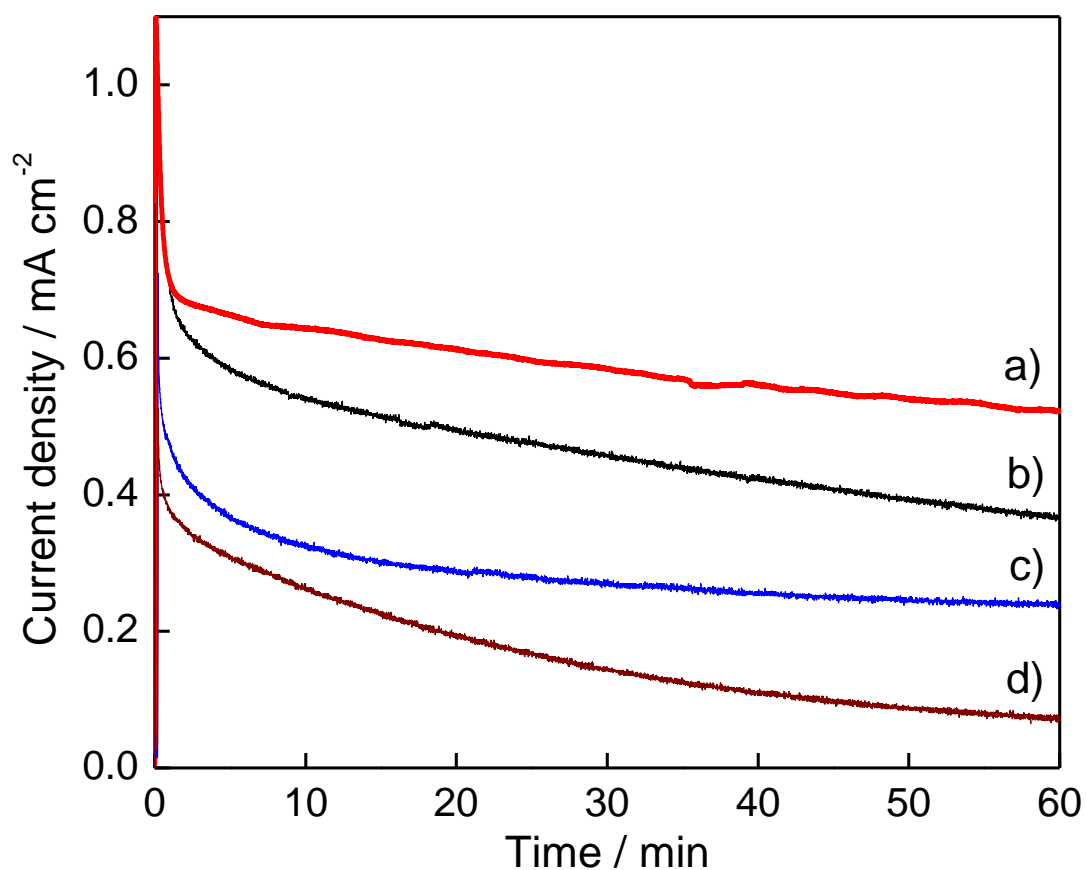


Figure 2-6. Photocurrent density-time profiles for the nanoporous ITO/WO₃ electrode in the (a) presence and (b-d) absence of 0.1 mM Co²⁺ ion in a 0.1 M phosphate solution of (a,b) pH 6.0, (c) pH 3.0 and (d) pH 9.0 at 0.5 V vs. Ag/AgCl. Visible light ($\lambda > 390$ nm, 100 mW cm⁻²) was irradiated from an ITO substrate side.

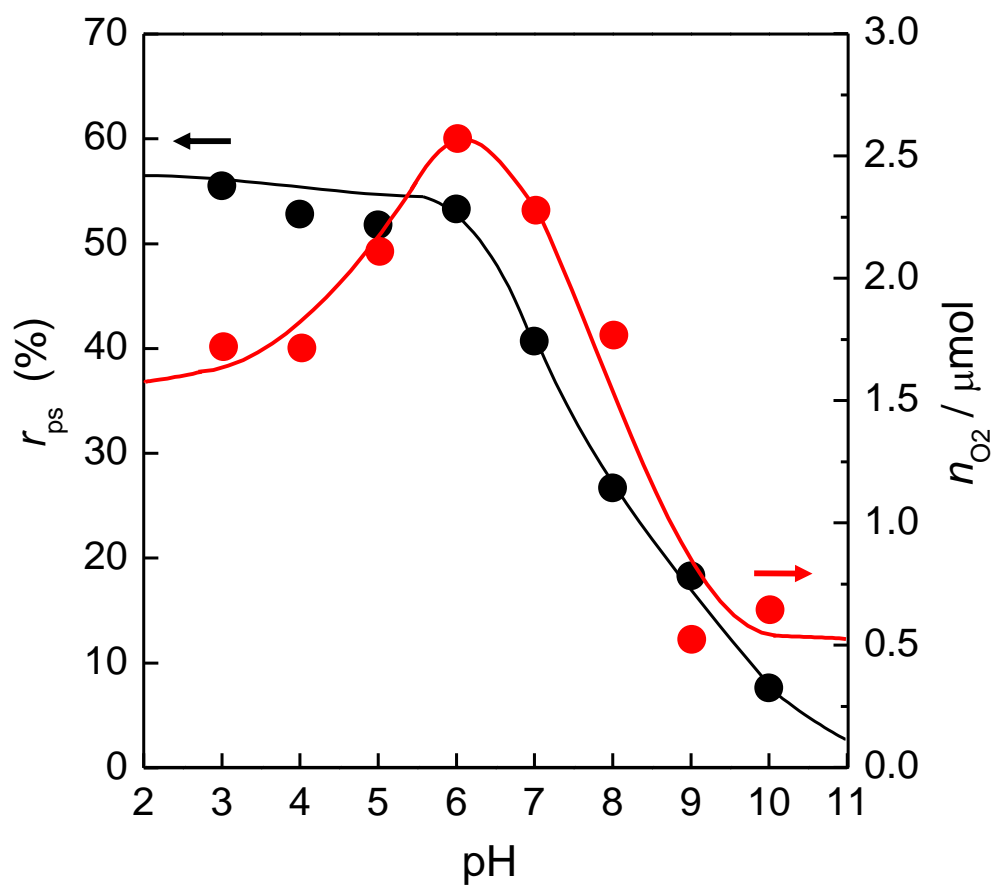


Figure 2-7. Plots of degree of photocurrent stability (r_{ps}) and the amount (n_{O_2}) of O_2 evolved versus pH for the nanoporous ITO/ WO_3 electrode in a 0.1 M phosphate solution. r_{ps} was calculated as the photocurrent ratio of 1 min to 1 h during photoelectrocatalysis.

Chapter 3

Unique and facile solvothermal synthesis of mesoporous WO₃ using a solid precursor and a surfactant template as a photoanode for visible-light-driven water oxidation

Chapter 3

Unique and facile solvothermal synthesis of mesoporous WO₃ using a solid precursor and a surfactant template as a photoanode for visible-light-driven water oxidation

3.1 Background

The recent advances in nanostructured materials have expanded their potential applications in much-desired materials for efficient solar energy conversion^[1-6]. Photoelectrochemical (PEC) water splitting into oxygen and hydrogen is an attractive but challenging way for the conversion of solar energy,^[7] following the pioneer work on a TiO₂ photoanode for water splitting by Honda and Fujishima^[8]. Unfortunately, owing to its wide electronic bandgap (3.0 to 3.2 eV), TiO₂ absorbs only an ultraviolet fraction of a solar spectrum (which accounts for just 4% of solar irradiation), being consequently responsible for low efficiency in utilization of solar light^[2,7,9]. For solar water splitting, intensive researches have been focused on nanostructured materials with narrow bandgaps including WO₃^[3,4,10-19]. WO₃, an n-type semiconductor, has attracted immense attention as a photoanode material for water oxidation in PEC cells because of its visible light response (bandgap, $E_g = 2.6$ to 2.8 eV), a valence band edge position thermodynamically possible for water oxidation (about 3 V versus the normal hydrogen electrode), and good photochemical stability under the acidic conditions^[3,10-12,20-24].

Porous material design, which has been developed employing template-directed approaches using small organic compounds^[25], supramolecular assembly^[26], and polymer beads^[27], is of great importance in many research fields because of the high porosity, large area per unit volume, and favorable design of a porous structure^[25,28,29]. So far, several efforts in nanostructural and porosity controls of WO₃ have been provided to increase the contact area between an electrode and an electrolyte solution and to make electron transport in WO₃ films more efficient, enhancing performance of PEC water oxidation at WO₃ electrodes^[3,11,30-33]. For example, Santato *et al.* have reported that crystalline WO₃ photoanodes with interconnected nanoparticulate structures improved photoelectrochemical properties^[30-32]. Berger *et al.* have demonstrated that random porous layers of WO₃ produced significantly higher photocurrent efficiency than a compact layer^[33]. Our group recently demonstrated a crystalline small mesoporous network of a WO₃ photoanode for high improvement in performance of PEC water oxidation^[3].

Numerous methods have been employed to control the dimension, morphology, and crystal structure of WO₃, *e.g.*, vacuum evaporation^[34], chemical vapor deposition^[35,36], sol-gel precipitation^[22,30-32], hydrothermal/solvothermal^[37-40], surfactant/hard template techniques^[3,41,42], and so on. Among the abundant methods, hydrothermal/solvothermal techniques can provide a cost-effective and one-step route synthesis of WO₃^[37-40]. Although the surfactant template techniques require a liquid tungsten precursor to utilize interaction with a surfactant in principle, we have focused on the interaction between a solid tungsten precursor and a surfactant under

solvothermal conditions to yield mesoporous WO_3 . Herein, we report the unique and facile synthesis of mesoporous WO_3 utilizing solid H_2WO_4 as a tungsten precursor with an organic amphiphilic molecule, dodecylamine (DDA), as a surfactant template for porosity of the nanostructure. The mesoporous WO_3 exhibited high surface area and improved the performance of PEC water oxidation compared to the corresponding materials prepared without a template.

3.2 Methods

Materials

Tungstic acid (H_2WO_4) was purchased from Kanto Chemical Co., Inc. (Chuo-ku, Tokyo, Japan). DDA was obtained from Sigma-Aldrich (St. Louis, MO, USA). Polyethylene glycol (PEG, molecular weight = 2,000) was obtained from Wako Chemical Co. (Osaka, Japan). Marpolose (60MP-50) was purchased from Matsumoto Yushi-Seiyaku Co. (Osaka, Japan). An indium tin oxide (ITO)-coated glass substrate was obtained from Asahi Glass Co. (Tokyo, Japan). Millipore water (Merck Ltd., Tokyo, Japan) was used for all the experiments. All other chemicals unless mentioned otherwise were of analytical grade and used as received.

Synthesis of mesoporous WO_3

In a typical synthesis, 1.7 g of DDA (9.0 mmol) was dissolved in 15 mL ethanol under stirring at room temperature. Tungstic acid (0.9 g; 3.6 mmol) was added to the DDA solution with stirring for 30 min to yield a suspension. It was transferred to a Teflon-lined stainless steel autoclave and then placed in an oil bath at 150 °C for 24 h.

After the autoclave was cooled down to room temperature, the solid product was recovered by centrifugation, then washed repeatedly by ethanol and air-dried. The solid product was calcined at 400 °C with a rate of 1 °C min⁻¹ and then maintained at 400 °C for 1 h in flowing N₂, followed by changing to O₂ flow (at 400 °C) for 2 h to result in a WO₃ sample (denoted as WO₃-DDA). A control sample (denoted as WO₃-bulk) was prepared in the same manner except for the addition of DDA.

Preparation of electrodes

The WO₃ film-coated ITO electrodes (ITO/WO₃) were prepared employing a doctor-blade technique. Before coating, ITO glass substrates (1.0 cm⁻² area) were cleaned up by a UV-ozone treatment (photo surface processor PL16-110, Sen Lights Co., Osaka, Japan) for 15 min. In a typical procedure, WO₃ powder (200 mg), PEG (100 mg), and Marpolose (20 mg) were mixed in 300 µL of water. The mixture suspension was stirred for approximately 2 to 4 h until a smooth paste was formed. The resulting paste was squeezed over an ITO glass substrate by a doctor-blade coater and dried at 80 °C for 15 min. After repeating the procedure for two times, the electrodes were calcined at 400 °C and maintained at 400 °C in flowing N₂ for 1h, followed by changing to O₂ flow (at 400 °C) for 2 h.

Structural characterization

Characterization of the morphological features and the crystalline phase was conducted by field-emission scanning electron microscopy (FESEM; JSM-6500F,

JEOL Ltd., Akishima, Tokyo, Japan) and powder X-ray diffraction (XRD; MiniFlexII, Rigaku Corporation, Tokyo, Japan) using monochromated Cu K α ($\lambda = 1.54 \text{ \AA}$) radiation. Nitrogen adsorption-desorption isotherms were measured using a BELSORP-miniII (BEL Japan, Inc., Osaka, Japan) at 77 K. Prior to gas adsorption, samples were degassed in vacuum for 4 h at 150 °C. The Brunauer-Emmett-Teller (BET) method was utilized to calculate the surface areas. The pore size distributions were obtained from analysis of the adsorption branches of the isotherms by the Barrett-Joyner-Halenda (BJH) method. Fourier transform infrared spectra were recorded on a Jasco FT/IR-4200 spectrophotometer (Jasco Inc., Tokyo, Japan).

Photoelectrochemical measurements

Photoelectrochemical measurement was carried out in a two-compartment photoelectrochemical cell separated by a Nafion membrane using an electrochemical analyzer (HZ-3000, Hokuto Denko Co. Ltd., Tokyo, Japan). A three-electrode system has been employed by using ITO/WO₃ and Ag/AgCl electrodes in one compartment as the working and reference electrodes, respectively, and a Pt wire in the other compartment as the counter electrode. An aqueous 0.1 M phosphate solution was used as an electrolyte in both compartments of the cell, which was saturated with Ar gas prior to the measurement. The cyclic voltammogram (CV) was recorded at a scan rate of 50 mV s⁻¹ at 25 °C. Light ($\lambda > 390 \text{ nm}$) was irradiated from the backside of the working electrode using a 500-W xenon lamp (Optical ModuleX; Ushio Inc., Tokyo, Japan) with a UV-cutfilter (L39) and liquid filter (0.2 M CuSO₄) for cutting of heat ray. The output of light intensity was calibrated as 100 mW cm⁻² using a

spectroradiometer (USR-40; Ushio Inc., Tokyo, Japan). Photoelectrocatalysis was conducted under the potentiostatic conditions of 0.5 V versus Ag/AgCl at 25 °C under illumination of light ($\lambda > 390$ nm, 100 mW cm^{-2}) for 1 h. The amounts of H_2 and O_2 evolved were determined from the analysis of the gas phase (headspace volume: 87.3 mL) of counter and working electrode compartments, respectively, using gas chromatography (GC-8A with a TCD detector and molecular sieve 5A column and Ar carrier gas; Shimadzu Corporation, Kyoto, Japan).

3.3 Results and discussion

The powder XRD patterns of the WO_3 samples calcined at 400 °C and 500 °C are shown in Figure 1. Small-angle XRD patterns (Figure 1 (a)) of WO_3 -DDA at 400 °C showed a single diffraction peak at low 2θ , being a sign of formation of mesoporous structures, but the weak intensity and broadness of the peak are possibly due to disordered mesoporous structures. The d -spacing, calculated from the XRD peak at $2\theta = 2.3^\circ$ is 3.78 nm. Weakening of the intensity of the diffraction peak for WO_3 -DDA at 500 °C (Figure 1 (b)) suggests degradation of the mesostructure at higher temperature. The wide-angle XRD patterns of both the WO_3 -DDA and WO_3 -bulk samples revealed crystallization of the framework after calcination at 400 °C and higher degree of crystallization at 500 °C, though crystallinity of WO_3 -bulk seems to be higher than that of WO_3 -DDA at both calcination temperatures. The d -spacings calculated from the XRD peaks of both WO_3 -DDA and WO_3 -bulk were in good agreement with phase-pure monoclinic WO_3 (JCPDS number: 43-1305). Average crystallite sizes for WO_3 -DDA, estimated using [002] reflections were 5.7 and 11.6 nm at 400 °C and

500 °C, respectively, which suggests that progressive growth of the WO₃ nanocrystal in the porous network is responsible for degradation of the mesostructure at 500 °C.

N₂ adsorption/desorption isotherms of the WO₃ samples calcined at 400 °C and 500 °C are shown in Figure 2. The isotherm (Figure 2 (a)) of WO₃-DDA calcined at 400 °C could be classified as type IV, characteristic of mesoporous materials^[26,43]. In this isotherm, the adsorption amount gradually increased in a range of $P/P_0 = 0.4$ to 0.85, which could be explained by the classical capillary condensation observed for mesopores. The H2 hysteresis loop in the isotherm (Figure 2 (a)) may be caused by roughness of the pore and particle surface^[44]. The BET surface area and mesopore volume for WO₃-DDA calcined at 400 °C were 57 m² g⁻¹ and 0.08 cm³ g⁻¹, respectively, as summarized in Table 1. The pore size distribution (Figure 2) by the BJH method shows narrow distribution with a peak pore width at 4.9 nm. Isotherm of WO₃-DDA calcined at 500 °C shows a predominantly type II nature, and the BET surface area was drastically reduced to 12 m² g⁻¹. The pore size distribution of WO₃-DDA calcined at 500 °C gives a wider peak at approximately 50 nm due to large interparticle pores. These results are in accordance with the degradation of the mesoporous structure of WO₃-DDA due to progressive growth of WO₃ nanocrystals at higher temperature of 500 °C, as observed in the XRD measurement. The WO₃-bulk sample synthesized without DDA exhibited typical type II isotherms, characteristic of nonporous solids. The BET surface area is 24 m² g⁻¹ at 400 °C, which is noticeably low compared to the mesoporous WO₃-DDA.

The Fourier transform infrared (FTIR) spectra of as-made (before calcination)

and calcined (400 °C and 500 °C) WO₃-DDA samples are shown in Figure 3. C-H stretching vibration bands of the hydrocarbon chains at 2,919 cm⁻¹ (asymmetric) and 2,844 cm⁻¹ (symmetric) along with C-H bending vibration bands at 1,469 cm⁻¹ of CH₂ groups were clearly observed in the as-made sample. Comparing the FTIR spectra of the as-made WO₃-DDA with calcined WO₃-DDA samples, we could see that peaks due to C-H vibration diminished completely for the calcined samples. This indicates complete removal of DDA during calcination at 400 °C and 500 °C, which is very much necessary to generate high porosity for these mesoporous materials.

The scanning electron microscopy (SEM) images of the calcined WO₃-DDA samples are shown in Figure 4. The SEM images of the topview (Figure 4a,b) exhibit that a mesoporous network is composed of tiny spherical WO₃ particles of *ca.* 5 to 20 nm in diameter, being wellconnected to each other. In a few places, the spherical particles agglomerate to form large particles. A close look into these images suggests that the average dimension of particles increases with calcination temperature from 400 °C to 500 °C due to sintering of WO₃ nanocrystals at higher calcination temperature. After preparation of a mesoporous WO₃ film on an ITO electrode, the film thickness was measured to be *ca.* 12 μm from the cross-sectional SEM image (Figure 4c). This crystalline mesoporous structure of the connected WO₃ particles is important to yield a large interface between the electrolyte and film as well as efficient electron transport through the film, which are consequently expected to work efficiently for PEC water oxidation since the electron and hole pairs generated by photoexcitation of WO₃ would have less chance to recombine before participating in a

water oxidation reaction at the WO₃ surface.

The PEC properties of the ITO/WO₃ electrodes were studied in a 0.1 M phosphate solution. Figure 5 shows the CVs of the ITO/WO₃ electrodes. On CVs of samples calcined at 400 °C for both WO₃-DDA and WO₃-bulk (Figure 5, left), no redox response was observed in the dark in a potential range of 0.4~1.0 V versus Ag/AgCl except for a response based on WO₃/H_xWO₃ below 0.2 V. Upon irradiation of visible light, the anodic current (0.13~0.18 mA cm⁻² at 1.0 V versus Ag/AgCl) was hardly generated for both samples. This is ascribed to insufficient crystallinity of both WO₃-DDA and WO₃-bulk calcined at 400 °C. Crystallinity rather than porosity for samples calcined at 400 °C is a dominant factor for the PEC performance of the WO₃-based photoanode under the conditions employed^[20,32]. On CVs of the samples calcined at 500 °C (Figure 5, right), the significantly high photoanodic current due to water oxidation was observed upon visible light irradiation above an onset potential of 0.17 V versus Ag/AgCl due to higher crystallinity. The photoanodic current reached 1.1 mA cm⁻² at 1.0 V for WO₃-DDA, which is about three times higher compared to that for the WO₃-bulk (0.36 mA cm⁻² at 1.0 V) electrode in spite of the degradation of mesoporous structure for WO₃-DDA calcined at 500 °C. The degraded mesoporous structure for WO₃-DDA might result in favorable conditions for PEC water oxidation compared with the nanoparticle structure of WO₃-bulk. Otherwise, another important factor might be involved in the higher performance of the WO₃-DDA electrode. In the present paper, we do not pursue interpretation of the higher performance of the WO₃-DDA electrode because our attention is on the solvothermal synthesis of a

mesoporous structure of WO₃.

Photoelectrocatalysis over the ITO/WO₃ electrodes was conducted in a 0.1 M phosphate solution (pH = 6.0) under potentiostatic conditions at 0.5 V versus Ag/AgCl for 1 h upon visible light irradiation ($\lambda > 390$ nm, 100 mW cm⁻²). The photocurrent-time profiles of both WO₃-DDA and WO₃-bulk calcined at 500 °C exhibit initial spikes in the photocurrent upon illumination (related with the capacitance component at the solid-liquid interface), followed by a photocatalytic current, as shown in Figure 6. The photocurrent density of WO₃-DDA at 1 min was 0.37 mA cm⁻², which is 2.5 times higher than that of the WO₃-bulk (0.15 mA cm⁻² at 1 min) electrode. The charge amount passed during 1-h photoelectrocatalysis for WO₃-DDA (0.89 C) was 3.9 times higher than that of WO₃-bulk (0.23 C). As a consequence of the high charge amount, the markedly high amount ($n_{O_2} = 1.5$ μmol, Faradaic efficiency (FE_{O2}) = 65%) of O₂ evolved for the WO₃-DDA electrode compared to that ($n_{O_2} = 0.4$ μmol, FE_{O2} = 58%) of the WO₃-bulk electrode, as summarized in Table 2. As compared with performances of PEC water oxidation under the same conditions for WO₃-based photoanodes reported earlier^[3], the performance of the present mesoporous WO₃-DDA is lower than that of the small mesoporous WO₃ film ($n_{O_2} = 4.2$ μmol, FE_{O2} = 79%)^[3], but much higher than that of interparticle mesoporous WO₃ ($n_{O_2} = 0.9$ μmol, FE_{O2} = 61%) and bulk WO₃ ($n_{O_2} = 0.4$ μmol, FE_{O2} = 44%)^[3]. The high performance of the mesoporous WO₃-DDA photoanode is attributed to its high surface-to-volume ratio which offers a large number of water oxidation sites at the electrolyte-WO₃ interface, and well-connected

WO₃ particles for efficient electron transport through the film.

3.4 Conclusions

We have prepared mesoporous WO₃ materials by a unique and facile solvothermal method using solid H₂WO₄ as a tungsten precursor. DDA was used as a template for the formation of nanostructure, which generates mesoporosity after removing DDA by calcination. The present surfactanttemplate technique is very unique in terms of use of a solid tungsten precursor in a solvothermal method, compared with a common technique using liquid tungsten precursors for interaction with surfactants in principle. The mesoporous network has a disordered arrangement of pores which is composed of well-connected tiny spherical WO₃ particles with a diameter of *ca.* 5 to 20 nm. The DDA-templated WO₃ photoanode showed three times higher photoanodic current density upon visible light irradiation and provided the efficient performance of PEC water oxidation compared to the untemplated WO₃, which is promising as an efficient material for high-performance solar energy conversion.

3.5 Competing interests

The authors declare that they have no competing interests.

3.6 Authors' contributions

LD prepared the samples and performed the photoelectrochemical measurements. DC carried out the analysis and optimization of the results and drafted the manuscript. KS and TY helped analyze the results. MY supervised the data analysis and

interpretation of the results and helped draft the manuscript. All authors read and approved the final manuscript.

3.7 Acknowledgments

This work was partially supported by the JST PRESTO program and Grant-in-Aid for Scientific Research (B) from the Ministry of Education, Culture, Sports, Science and Technology (No. 24350028). DC thanks JSPS for providing postdoctoral fellowship.

3.8 References

1. Kamat PV, Tvrđy K, Baker DR, Radich JG: **Beyond photovoltaics: semiconductor nanoarchitectures for liquid-junction solar cells.** *Chem Rev* 2010, **110**:6664.
2. Kudo A, Miseki Y: **Heterogeneous photocatalyst materials for water splitting.** *Chem Soc Rev* 2009, **38**:253.
3. Chandra D, Saito K, Yui T, Yagi M: **Crystallization of tungsten trioxide having small mesopores: highly efficient photoanode for visible-light-driven water oxidation.** *Angew Chem Int Ed* 2013, **52**:12606.
4. Kim HG, Borse PH, Jang JS, Ahn CW, Jeong ED, Lee JS: **Engineered nanorod perovskite film photocatalysts to harvest visible light.** *Adv Mater* 2011, **23**:2088.
5. Zukalová M, Zukal A, Kavan L, Nazeeruddin MK, Liska P, Grätzel M: **Organized mesoporous TiO₂ films exhibiting greatly enhanced performance in dye-sensitized solar cells.** *Nano Lett* 2005, **5**:1789.

6. Kim J, Koh JK, Kim B, Kim JH, Kim E: **Nanopatterning of mesoporous inorganic oxide films for efficient light harvesting of dye-sensitized solar cells.***Angew Chem Int Ed* 2012, **51**:6864.

7. Gratzel M: **Photoelectrochemical cells.***Nature* 2001, **414**:338.

8. Fujishima A, Honda K: **TiO₂ photoelectrochemistry and photocatalysis.***Nature* 1972, **238**:37.

9. Aprile C, Corma A, Garcia H: **Enhancement of the photocatalytic activity of TiO₂ through spatial structuring and particle size control: from subnanometric to submillimetric length scale.***Phys Chem Chem Phys* 2008, **10**:769.

10. Ng KH, Minggu LJ, Kassim MB: **Gallium-doped tungsten trioxide thin film photoelectrodes for photoelectrochemical water splitting.***Int J Hydrogen Energy* 2013, **38**:9585.

11. Kim JK, Shin K, Cho SM, Lee T-W, Park JH: **Synthesis of transparent mesoporous tungsten trioxide films with enhanced photoelectrochemical response: application to unassisted solar water splitting.***Energy Environ Sci* 2011, **4**:1465.

12. Chatchai P, Murakami Y, Kishioka S-y, Nosaka AY, Nosaka Y: **Efficient photocatalytic activity of water oxidation over WO₃/BiVO₄ composite under visible light irradiation.***Electrochim Acta* 2009, **54**:1147.

13. Hisatomi T, Dotan H, Stefik M, Sivula K, Rothschild A, Grätzel M, Mathews N: **Enhancement in the Performance of Ultrathin Hematite Photoanode for Water Splitting by an Oxide Underlayer.***Adv Mater* 2012, **24**:2699.
14. Satsangi VR, Kumari S, Singh AP, Shrivastav R, Dass S: **Nanostructured hematite for photoelectrochemical generation of hydrogen.***Int J Hydrogen Energy* 2008, **33**:312.
15. Rahman G, Joo O-S: **Photoelectrochemical water splitting at nanostructured α -Fe₂O₃ electrodes.** *Int J Hydrogen Energy* 2012, **37**:13989.
16. Li Y, Takata T, Cha D, Takanabe K, Minegishi T, Kubota J, Domen K: **Vertically aligned Ta₃N₅ nanorod arrays for solar-driven photoelectrochemical water splitting.***Adv Mater* 2013, **25**:125.
17. Maeda K, Higashi M, Lu D, Abe R, Domen K: **Efficient nonsacrificial water splitting through two-step photoexcitation by visible light using a modified oxynitride as a hydrogen evolution photocatalyst.***J Am Chem Soc* 2010, **132**:5858.
18. Maeda K, Domen K: **Water oxidation using a particulate BaZrO₃-BaTaO₂N solid-solution photocatalyst that operates under a wide range of visible light.***Angew Chem Int Ed* 2012, **51**:9865.
19. Abe T, Nagai K, Kabutomori S, Kaneko M, Tajiri A, Norimatsu T: **An organic photoelectrode working in the water phase: visible-light-induced dioxygen**

evolution by a perylene derivative/cobalt phthalocyanine bilayer. *Angew Chem Int Ed* 2006, **45**:2778.

20. Yang B, Zhang Y, Drabarek E, Barnes PRF, Luca V: **Enhanced photoelectrochemical activity of sol-gel tungsten trioxide films through textural control.** *Chem Mater* 2007, **19**:5664.

21. Seabold JA, Choi K-S: **Effect of a cobalt-based oxygen evolution catalyst on the stability and the selectivity of photo-oxidation reactions of a WO₃ photoanode.** *Chem Mater* 2011, **23**:1105.

22. Yagi M, Maruyama S, Sone K, Nagai K, Norimatsu T: **Preparation and photoelectrocatalytic activity of a nano-structured WO₃ platelet film.** *J Solid State Chem* 2008, **181**:175.

23. Miseki Y, Kusama H, Sugihara H, Sayama K: **WO₃ photocatalyst showing efficient solar energy conversion for O₂ production and Fe (III) ion reduction under visible light.** *J Phys Chem Lett* 2010, **1**:1196.

24. Miseki Y, Fujiyoshi S, Gunji T, Sayama K: **Photocatalytic water splitting under visible light utilizing I₃⁻/I⁻ and IO₃⁻/I⁻ redox mediators by Z-scheme system using surface treated PtO_x/WO₃ as O₂ evolution photocatalyst.** *Catal Sci Tech* 2013, **3**:1750.

25. Corma A: **From microporous to mesoporous molecular sieve materials and their use in catalysis.***Chem Rev* 1997, **97**:2373.
26. Kresge CT, Leonowicz ME, Roth WJ, Vartuli JC, Beck JS: **Ordered mesoporous molecular sieves synthesized by a liquid-crystal template mechanism.***Nature* 1992, **359**:710.
27. Chandra D, Bekki M, Nakamura M, Sonezaki S, Ohji T, Kato K, Kimura T: **Dye-sensitized biosystem sensing using macroporous semiconducting metal oxide films.***J Mater Chem* 2011, **21**:5738.
28. Davis ME: **Ordered porous materials for emerging applications.***Nature* 2002, **417**:813.
29. Sanchez C, Boissière C, Grosso D, Laberty C, Nicole L: **Design, synthesis, and properties of inorganic and hybrid thin films having periodically organized nanoporosity.***Chem Mater* 2008, **20**:682.
30. Santato C, Ulmann M, Augustynski J: **Photoelectrochemical properties of nanostructured tungsten trioxide films.***J Phys Chem B* 2001, **105**:936.
31. Santato C, Ulmann M, Augustynski J: **Enhanced visible light conversion efficiency using nanocrystalline WO₃ Films.***Adv Mater* 2001, **13**:511.

32. Santato C, Odziemkowski M, Ulmann M, Augustynski J: **Crystallographically oriented mesoporous WO₃ films: synthesis, characterization, and application.***J Am Chem Soc* 2001, **123**:10639.
33. Berger S, Tsuchiya H, Ghicov A, Schmuki P: **High photocurrent conversion efficiency in self-organized porous WO₃.***Appl Phys Lett* 2006, **88**:203119.
34. Colton RJ, Guzman AM, Rabalais JW: **Electrochromism in some thin-film transition-metal oxides characterized by x-ray electron spectroscopy.***J Appl Phys* 1978, **49**:409.
35. Yous B, Robin S, Donnadiou A, Dufour G, Maillot C, Roulet H, Senemaud C: **Chemical vapor deposition of tungsten oxides: A comparative study by X-ray photoelectron spectroscopy, X-ray diffraction and reflection high energy electron diffraction.***Mater Res Bull* 1984, **19**:1349.
36. Sivakumar R, Moses Ezhil Raj A, Subramanian B, Jayachandran M, Trivedi DC, Sanjeeviraja C: **Preparation and characterization of spray deposited n-type WO₃ thin films for electrochromic devices.***Mater Res Bull* 2004, **39**:1479.
37. Saha D, Jensen KMØ, Tyrsted C, Bøjesen ED, Mamakhel AH, Dippel A-C, Christensen M, Iversen BB: **In situ total X-Ray scattering study of WO₃nanoparticle formation under hydrothermal conditions.***Angew Chem Int Ed* 2014, **53**:3667.

38. Wang N, Wang D, Li M, Shi J, Li C: **Photoelectrochemical water oxidation on photoanodes fabricated with hexagonal nanoflower and nanoblock WO₃.***Nanoscale* 2014, **6**:2061.
39. Zeng W, Li Y, Zhang H: **Hierarchical WO₃ porous microspheres and their sensing properties.***J Mater Sci: Mater Electron* 2014, **25**:1512.
40. Katsumata H, Inoue K, Suzuki T, Kaneco S: **Facile synthesis of WO₃ nanorod thin film on W substrate with enhance photocatalytic performance.***Catal Lett* 2014, **144**:837.
41. Brezesinski T, Fattakhova Rohlfing D, Sallard S, Antonietti M, Smarsly BM: **Highly crystalline WO₃ thin films with ordered 3D mesoporosity and improved electrochromic performance.***Small* 2006, **2**:1203.
42. Sadakane M, Sasaki K, Kunioku H, Ohtani B, Ueda W, Abe R: **Preparation of nano-structured crystalline tungsten(vi) oxide and enhanced photocatalytic activity for decomposition of organic compounds under visible light irradiation.***Chem Commun* 2008, 6552.
43. Chandra D, Yokoi T, Tatsumi T, Bhaumik A: **Highly luminescent organic–inorganic hybrid mesoporous silicas containing tunable chemosensor inside the pore wall.***Chem Mater* 2007, **19**:5347.
44. Grosman A, Ortega C: **Capillary condensation in porous materials. Hysteresis**

and interaction mechanism without pore blocking/percolation process.*Langmuir.*

2008, **24**:3977.

Table 3-1. Physicochemical properties of WO₃ samples.

Sample name	Calcination temperature	<i>d</i> -spacing [nm]	Surface area [m ² g ⁻¹]	Pore volume [cm ³ g ⁻¹]	Pore size [nm]
WO ₃ -DDA	400 °C	1.70	57	0.08	4.9
WO ₃ -DDA	500 °C	-	12	0.09	48.2
WO ₃ -bulk	400 °C	-	24	0.19	52.7

Table 3-2. Summary of photoelectrocatalytic water oxidation at different ITO/WO₃ photoanodes calcined at 500 °C in a 0.1M phosphate solution.

Sample name	Charge / C	n _{O2} / μmol	F.E. _{O2} ^a (%)	n _{H2} ^b / μmol	F.E. _{H2} ^c (%)
WO ₃ -DDA	0.89	1.49	65.2	4.46	97.4
WO ₃ -bulk	0.23	0.35	58.1	0.89	74.3

^a Faradic efficiency of O₂ evolution

^b n_{H2} is the amount of H₂ evolved in the Pt counter electrode compartment.

^c Faradic efficiency of H₂ evolution

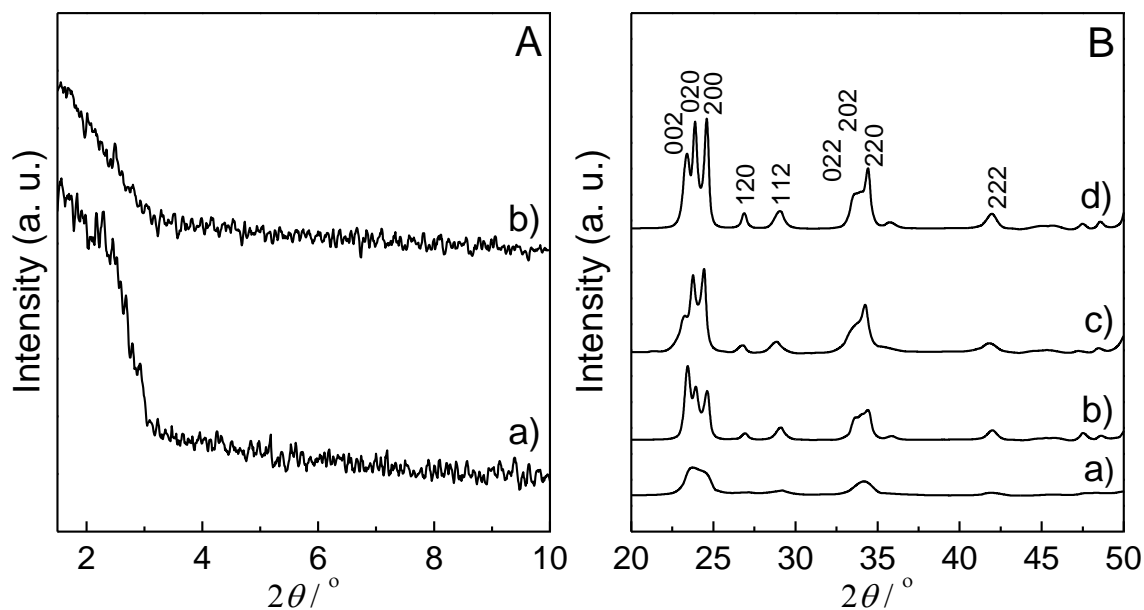


Figure 3-1. (A) Small-angle and (B) wide-angle XRD patterns of WO₃-DDA and WO₃-bulk samples after being calcined at 400 and 500 °C. a) WO₃-DDA calcined at 400°C, b) WO₃-DDA calcined at 500°C, c) WO₃-bulk calcined at 400°C, d) WO₃-bulk calcined at 500°C.

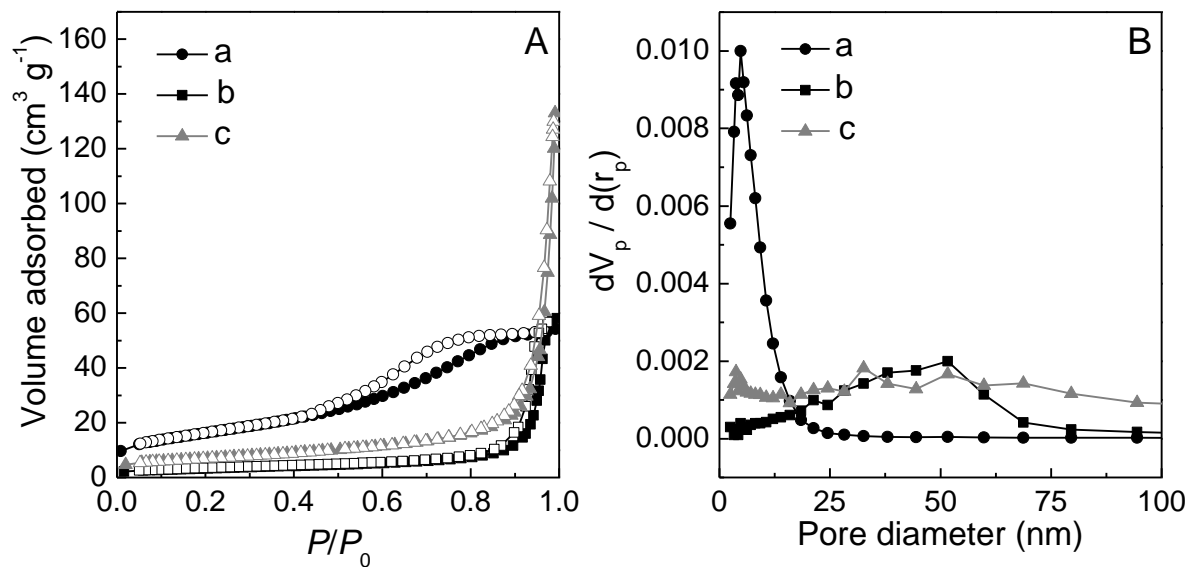


Figure 3-2. (A) N₂ sorption isotherms and (B) pore size distribution of WO₃-DDA and WO₃-bulk samples after being calcined at 400 and 500 °C. In N₂ sorption isotherm adsorption and desorption points are marked by filled and empty symbols respectively. a) WO₃-DDA calcined at 400°C, b) WO₃-DDA calcined at 500°C, c) WO₃-bulk calcined at 400°C.

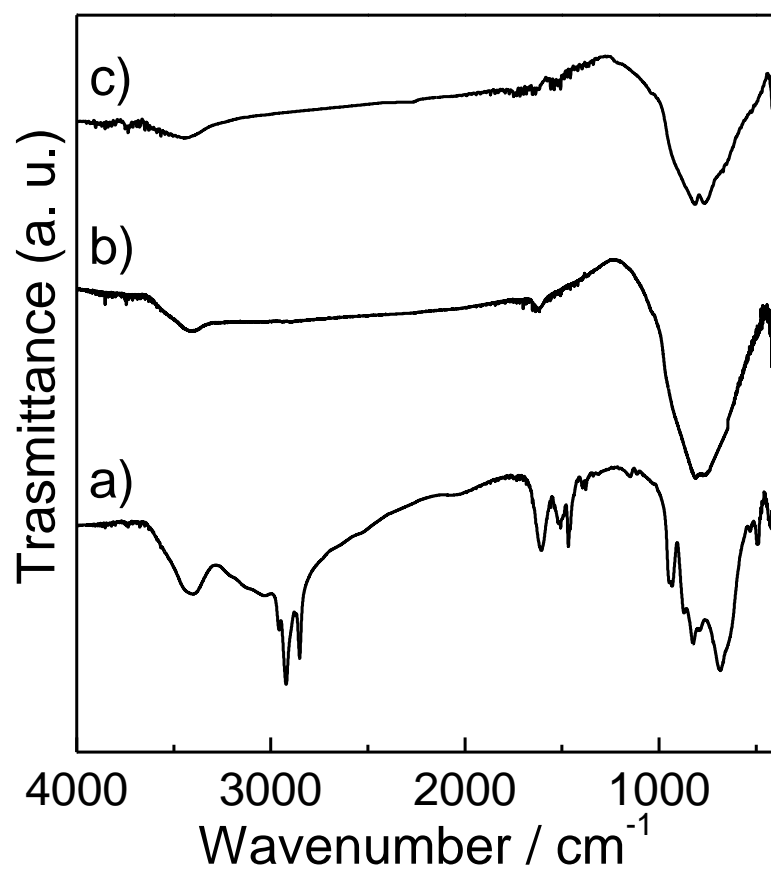


Figure 3-3. FT-IR spectra of WO_3 -DDA samples for (a) as-made and after being calcined at (b) 400 and (c) 500 °C.

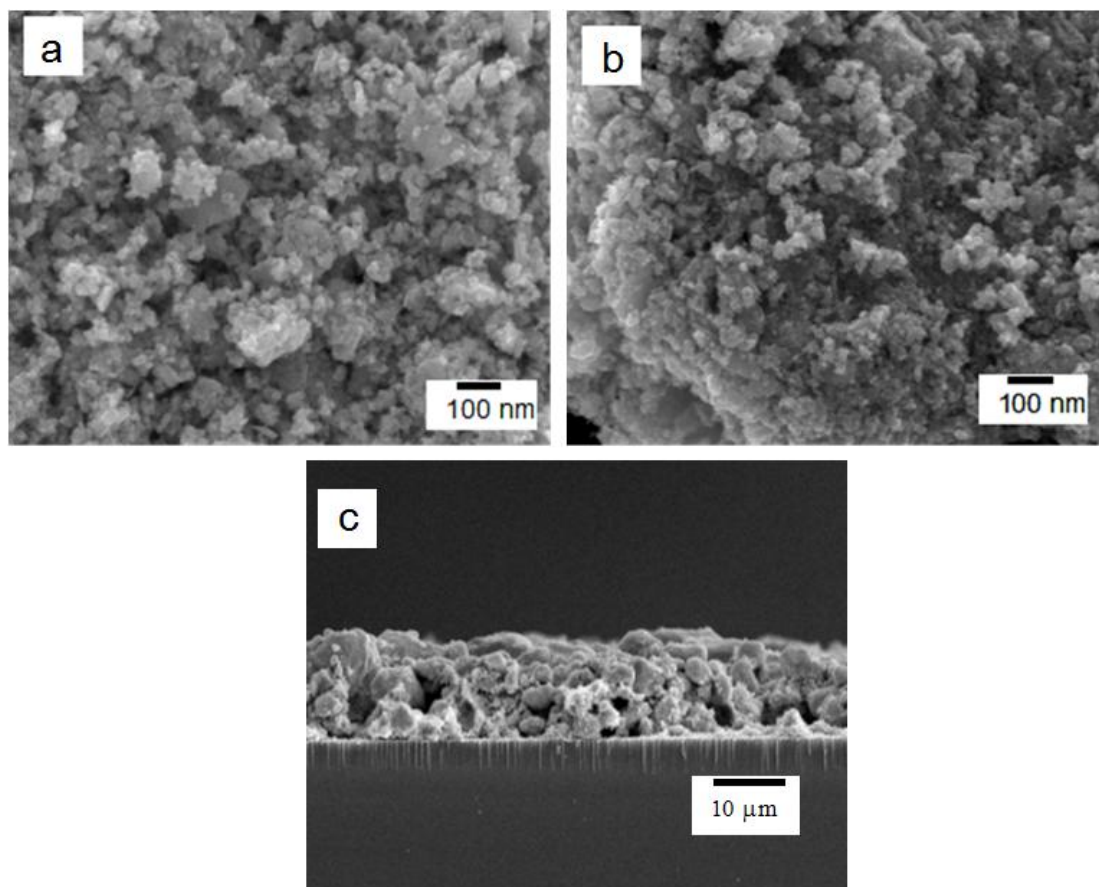


Figure 3-4. Scanning electron microscopic (SEM) images. Top view of WO₃-DDA samples at calcined (a) 400 and (b) 500 °C, (c) cross-sectional view of the ITO/WO₃-DDA electrode after being calcined at 500 °C.

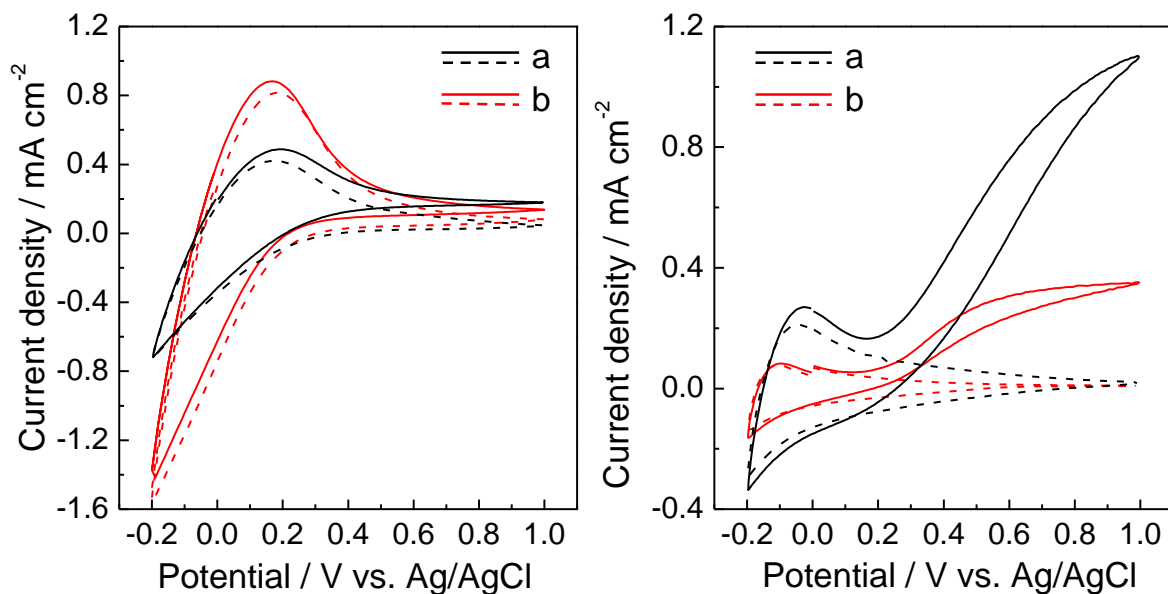


Figure 3-5. Cyclic voltammograms (CVs) for the samples calcined at 400 °C (left) and 500 °C (right) of the (a) ITO/WO₃-DDA and (b) ITO/WO₃-bulk electrodes in a 0.1 M phosphate buffer solution of pH = 6.0. The dashed and solid lines represents CV measured in the dark and on irradiation of visible light ($\lambda > 390$ nm, 100 mW cm⁻²), respectively.

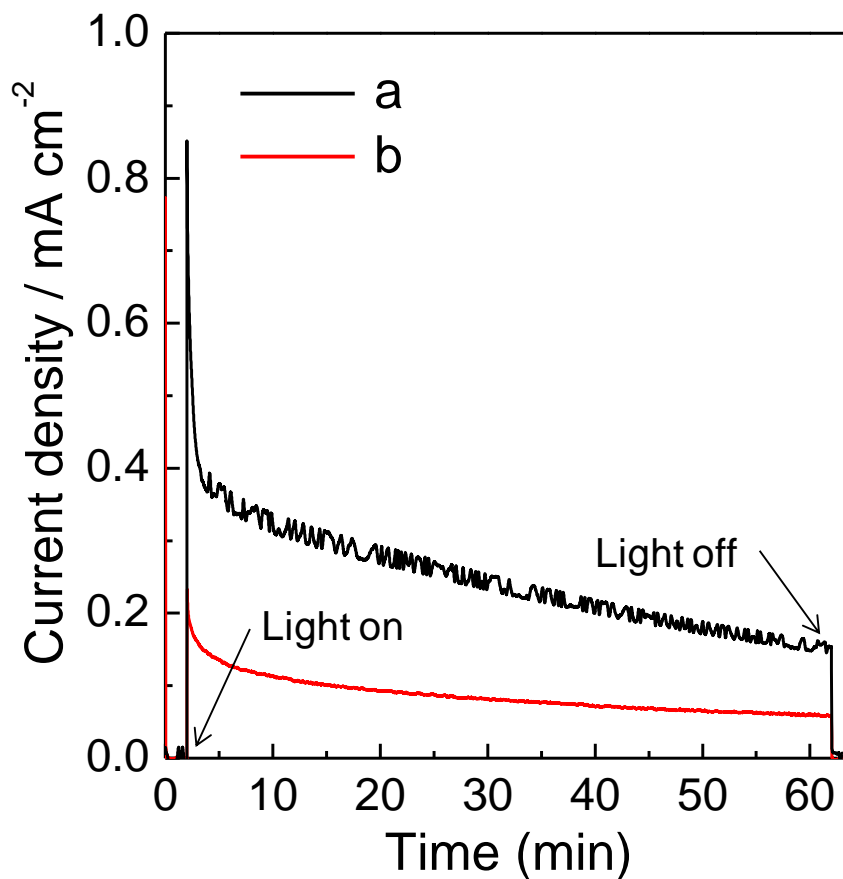


Figure 3-6. Photocurrent density versus time profiles during PEC water oxidation using the samples calcined at 500 °C of the (a) ITO/WO₃-DDA and (b) ITO/WO₃-bulk electrodes in a 0.1 M phosphate buffer solution of pH = 6.0 at 0.5 V vs. Ag/AgCl with visible light irradiation ($\lambda > 390$ nm, 100 mW cm⁻²).

Chapter 4

Unique synthesis of mesoporous WO₃ by in-situ N₂ intercalation from surfactant template : Photoanode for Visible-light-driven water oxidation

Chapter 4

Unique synthesis of mesoporous WO₃ by in-situ N₂ intercalation from surfactant template : Photoanode for Visible-light-driven water oxidation

4.1 Introduction

Recently, much attention has been paid on artificial photosynthesis in order to resolve the problem of environment pollution or energy storage¹⁻³. Photoelectrochemical (PEC) splitting of water is one of the most promising clean energy providing system in which H₂ and O₂ has been produced by utilizing abundant solar light. Since oxidation of water is considering as energy demanding bottle-neck is in PEC water splitting, a robust photoanode with high efficient for water oxidation is necessary. Since Fujishima and Honda described the TiO₂ photoanode in 1972⁴, a number of semiconductor and metal oxides have been investigated as photoanode for water oxidation^{2, 5, 6}. Unfortunately, owing to its wide electronic bandgap (3.0-3.2 eV), TiO₂ absorbs only an ultraviolet fraction of a solar spectrum (which accounts for just 3-5% of solar irradiation), being consequently responsible for low efficiency in utilization of solar light^{7, 8}. For solar water splitting, intensive researches have been focused on nanostructured materials with narrow bandgaps including tungsten trioxide (WO₃)⁹⁻²⁰. WO₃, an n-type semiconductor, has attracted immense attention as a photoanode material for water oxidation in Photoelectrochemical (PEC) cells because of its visible light response (bandgap, $E_g = 2.6$ to 2.8 eV), a valence band edge

position thermodynamically possible for water oxidation (about 3 V versus the normal hydrogen electrode), strong absorption within solar spectrum and good photochemical stability under the acidic conditions^{9, 11-13, 21-25}.

However, solar energy conversion efficiency of pure WO₃ is still limited due to its considerably high band gap, which restricts from sufficient strong visible region absorption of solar spectrum. So far, a lot of works have reported to improve visible light absorption through incorporation of dopants, such as, transition metal (Ti, Fe, Co, Ni, Cu, Zn)^{26, 27} and representative elements (N, C, S)²⁸⁻³⁰. Recently, Lewis et al. reported a WO₃ material with nitrogen molecules (N₂) intercalated into the crystalline lattice by a thermal decomposition of commercially available ammonium metatungstate ((NH₄)₆H₂W₁₂O₄₀ · xH₂O) and ammonium paratungstate ((NH₄)₁₀H₂W₁₂O₄₂ · 4H₂O) in O₂ atmosphere³¹. The N₂-intercalated WO₃ provides longer wavelength absorption compared with pure WO₃ due to narrowing of band gap by contribution of N 2p in N₂ to the valence band dominated by O 2p of WO₃.

So far, several efforts in nanostructural and porosity controls of WO₃ have been provided to increase the contact area between an electrode and an electrolyte solution and to make electron transport in WO₃ films more efficient, enhancing performance of PEC water oxidation at WO₃ electrodes^{8, 32-35}.^{9, 32, 36-38} For example, Santato *et al.* have reported that crystalline WO₃ photoanodes with interconnected nanoparticulate structures improved photoelectrochemical properties^{32, 39}. Berger et al. have demonstrated that random porous layers of WO₃ produced significantly higher photocurrent efficiency than a compact layer³³. Our group recently demonstrated a

crystalline small mesoporous network of a WO_3 photoanode for high improvement in performance of PEC water oxidation⁹. On the other hand, more and more attention have been paid to synthesize mesoporous materials⁴⁰⁻⁴³. Also, mesoporous materials are widely used as photoanode materials to improve the solar energy conversion efficient because mesoporous materials possess continuous pore channels, and high specific surface area have been proved to enhance the separation the photoexcited electrons and holes efficiently⁴⁴⁻⁴⁷. Our group recently demonstrated a crystalline small mesoporous network of a WO_3 using peroxo-tungstic acid (PA) as a tungsten precursor with an organic amphiphilic molecule, 2-(hexadecylaminomethyl) pyridine (PAL2-16) by surfactant-templated-carbonization method⁹. And also, our group were succeed to synthesize mesoporous WO_3 utilizing solid H_2WO_4 as a tungsten precursor with an organic amphiphilic molecule, dodecylamine (DDA), as a surfactant template using hydrothermal treatment (HTT)⁴⁸. The mesoporous WO_3 exhibited high surface area and improved the performance of PEC water oxidation compared to the corresponding materials prepared without a template.

We report herein that a unique N_2 -intercalated WO_3 with a mesoporous structure was first succeed to synthesize by employing an facile one-step hydrothermal treatment procedure using DDA, which was used as an nitrogen source as well as a surfactant template for formation of mesoporous structure. The N_2 -intercalated mesoporous WO_3 exhibit that this photoanode material was responsive to visible light of $\lambda \leq 490$ nm, which is corroborated the optical band gap (2.5 eV). This band gap of N_2 -intercalated mesoporous WO_3 is narrower compared to the corresponding

materials prepared without a template. And also the performance of PEC water oxidation was improved.

4.2 Experimental section

Materials

Tungstic acid (H_2WO_4) was purchased from Kanto Chemical Co., Inc. (Chuo-ku, Tokyo, Japan). DDA was obtained from Sigma-Aldrich (St. Louis, MO, USA). Polyethylene glycol (PEG, molecular weight = 2,000) was obtained from Wako Chemical Co. (Osaka, Japan). Marpolose (60MP-50) was purchased from Matsumoto Yushi-Seiyaku Co. (Osaka, Japan). An indium tin oxide (ITO)-coated glass substrate was obtained from Asahi Glass Co. (Tokyo, Japan). Millipore water (Merck Ltd., Tokyo, Japan) was used for all the experiments. All other chemicals unless mentioned otherwise were of analytical grade and used as received.

Preparations

Optimization towards the amount of DDA for preparing mesoporous WO_3

0.17 g, 0.34 g, 0.68 g, 1.7 g and 3.4 g DDA (0.9 mmol, 1.8 mmol, 3.6 mmol, 9.0 mmol and 18 mmol, respectively) were dissolved in 15 mL ethanol using five beakers under stirring at room temperature. Yellow suspensions were obtained after 0.9 g H_2WO_4 (3.6 mmol) were added according to the molar ratio of H_2WO_4 and DDA at 1 : 0.25, 1 : 0.5, 1 : 1, 1 : 2.5 and 1 : 5. The suspensions were transferred to the Teflon-lined stainless steel autoclaves and then placed in an oil bath at 150 °C for 24 h. After the autoclaves were cooled down to room temperature, the DDA-derived precursors powder were recovered by centrifugation, then washed repeatedly by

ethanol and air-dried. The DDA-derived precursors powder were calcined at 400 °C with a rate of 1 °C min⁻¹ and then maintained at 400 °C for 1 h in flowing N₂, followed by changing to O₂ flow (at 400 °C) for 2 h, obtaining five different WO₃ samples. A control sample (denoted as WO₃-bulk) was prepared in the same manner except for the addition of DDA.

Optimization of reaction temperature for HTT

1.7 g DDA (9.0 mmol) was dissolved in 15 mL ethanol under stirring at room temperature. Tungstic acid (0.9 g; 3.6 mmol) was added to the DDA solution with stirring for 30 min to yield a yellow suspension according to the molar ratio of H₂WO₄ and DDA at 1 : 2.5. Another three suspensions were prepared using the same recipe. After that, the suspensions were transferred to four Teflon-lined stainless steel autoclaves and then placed in the oil bath at 80 °C, 120 °C, 150 °C and 180 °C for 24 h, respectively. The four kinds of DDA-derived precursors powder were collected using such procedure described before and the DDA-derived precursors were calcined 400 °C result in four different WO₃ samples (denoted as WO₃-DDA-80, WO₃-DDA-120, WO₃-DDA-150, and WO₃-DDA-180).

Preparation of N₂-intercalated mesoporous WO₃

The N₂-intercalated mesoporous WO₃ sample was prepared from DDA-derived precursor followed calcination from 400 °C~550 °C in flowing N₂ for 1h, followed by changing to O₂ flow for 2 h.

Fabrication of electrodes

The WO₃ film-coated ITO electrodes (ITO/WO₃) were prepared employing a

doctor-blade technique. Before coating, ITO glass substrates (1.0 cm^{-2} area) were cleaned up by a UV-ozone treatment (photo surface processor PL16-110, Sen Lights Co., Osaka, Japan) for 15 min. In a typical procedure, WO_3 powder (200 mg), PEG (100 mg), and Marpolose (20 mg) were mixed in 300 μL of water. The mixture suspension was stirred for approximately 2 to 4 h until a smooth paste was formed. The resulting paste was squeezed over an ITO glass substrate by a doctor-blade coater and dried at $80\text{ }^\circ\text{C}$ for 15 min. After repeating the procedure for two times, the electrodes were calcined from $400\text{ }^\circ\text{C}$ ~ $550\text{ }^\circ\text{C}$ in flowing N_2 for 1h, followed by changing to O_2 flow for 2 h.

Structural characterization

Characterization of the morphological features and the crystalline phase was conducted by field-emission scanning electron microscopy (FESEM; JSM-6500F, JEOL Ltd., Akishima, Tokyo, Japan) and powder X-ray diffraction (XRD; MiniFlexII, Rigaku Corporation, Tokyo, Japan) using monochromated $\text{Cu K}\alpha$ ($\lambda = 1.54\text{ \AA}$) radiation. The Energy dispersive X-ray spectroscopic (EDS) data were taken using SEM images were taken using a scanning electron microscope (JEOL, TSM-6510LV) operated at an accelerating voltage of 10 kV. Nitrogen adsorption-desorption isotherms were measured using a BELSORP-miniII (BEL Japan, Inc., Osaka, Japan) at 77 K. Prior to gas adsorption, samples were degassed in vacuum for 4 h at $150\text{ }^\circ\text{C}$. The Brunauer-Emmett-Teller (BET) method was utilized to calculate the surface areas. The pore size distributions were obtained from analysis of the adsorption branches of the isotherms by the Barrett-Joyner-Halenda (BJH) method. Raman spectra were

recorded using a Raman microspectroscopic apparatus (Horiba-Jobin-Yvon, LabRAM HR). UV-visible diffuse reflectance spectra (DRS) were recorded on a spectrophotometer (JASCO, V-670) in a DR mode. Thermogravimetric (TG) and Differential Thermal Analysis (DTA) data were taken using a TG analyzer (Rigaku, TG 8120) from 25 to 800 °C with a heating rate of 5 °C min⁻¹ under air.

Photoelectrochemical measurements

Photoelectrochemical measurement was carried out in a two-compartment photoelectrochemical cell separated by a Nafion membrane using an electrochemical analyzer (HZ-3000, Hokuto Denko Co. Ltd., Tokyo, Japan). A three-electrode system has been employed by using ITO/WO₃ and Ag/AgCl electrodes in one compartment as the working and reference electrodes, respectively, and a Pt wire in the other compartment as the counter electrode. An aqueous 0.1 M phosphate solution was used as an electrolyte in both compartments of the cell, which was saturated with Ar gas prior to the measurement. For the investigation of effect of Co²⁺ ions on photoelectrocatalytic performance, 0.1 mM Co(NO₃)₂ · 6H₂O was maintained in the electrolyte solution of the working compartment. The cyclic voltammogram (CV) was recorded at a scan rate of 50 mV s⁻¹ at 25 °C. Light ($\lambda > 390$ nm) was irradiated from the backside of the working electrode using a 500 W xenon lamp (Optical ModuleX; Ushio Inc., Tokyo, Japan) with a UV-cutfilter (L39) and liquid filter (0.2 M CuSO₄) for cutting of heat ray. The output of light intensity was calibrated as 100 mW cm⁻² using a spectroradiometer (USR-40; Ushio Inc., Tokyo, Japan). Photoelectrocatalysis

was conducted under the potentiostatic conditions of 0.5 V versus Ag/AgCl at 25 °C under illumination of light ($\lambda > 390$ nm, 100 mW cm^{-2}) for 1 h. The amounts of H_2 and O_2 evolved were determined from the analysis of the gas phase (headspace volume: 87.3 mL) of counter and working electrode compartments, respectively, using gas chromatography (GC-8A with a TCD detector and molecular sieve 5A column and Ar carrier gas; Shimadzu Corporation, Kyoto, Japan). A monochromic light with 10 nm of bandwidth was given from a 500 W xenon lamp using a monochromator for incident photon-to-current conversion efficiency (IPCE) measurements.

4.3 Results and discussion

N_2 adsorption/desorption isotherms of the WO_3 samples prepared from DDA-derived precursor which was prepared from H_2WO_4 and DDA according to the molar ratio at 1 : 0.25, 1 : 0.5, 1 : 1, 1 : 2.5 and 1 : 5 under 150 °C oil bath reaction for 24h calcined at 400 °C is shown in Figure 1. When the molar ratio of H_2WO_4 and DDA increased to 1 : 2.5, the isotherm of WO_3 sample could be classified as type IV and the surface area was $57 \text{ m}^2 \text{ g}^{-1}$. The surface area results and pore size distributions were summarized in Table 1, in which indicate that the optimum molar ratio of H_2WO_4 and DDA is 1 : 2.5 for mesoporous synthesis.

N_2 adsorption/desorption isotherms of the WO_3 -DDA-80, WO_3 -DDA-120, WO_3 -DDA-150, and WO_3 -DDA-180 samples calcined at 400 °C are shown in Figure 2. It shows that the reaction temperature of 150 °C is the best one for HTT to synthesize mesoporous WO_3 , the surface area of WO_3 -DDA-150 was $57 \text{ m}^2 \text{ g}^{-1}$, as summarized in Table 2.

It has already known that the reaction temperature of 150 °C and molar ratio of 1 : 2.5 between H_2WO_4 and DDA are the optimum conditions for synthesizing mesoporous WO_3 . So we carried out all of experiments below using this optimum condition.

N_2 adsorption/desorption isotherms of the WO_3 -DDA samples calcined at 400 °C~500 °C are shown in Figure 3A. In this isotherm, for the adsorption amount gradually increased in a range of $P/P_0 = 0.4$ to 0.85, which could be explained by the classical capillary condensation observed for mesopores. The H_2 hysteresis loop in the isotherm for WO_3 -DDA calcined at 400 °C may be caused by roughness of the pore and particle surface.⁴⁹ The BET surface area and mesopore volume for WO_3 -DDA calcined at 400 °C were $57 \text{ m}^2 \text{ g}^{-1}$ and $0.08 \text{ cm}^3 \text{ g}^{-1}$, respectively, as summarized in Table 3. The pore size distribution (Figure 3B) by the BJH method shows narrow distribution with a peak pore width at 4.8 nm. The surface area of WO_3 -DDA samples, as summarized in Table 3, decreased with increasing the calcination temperature due to decomposition of mesoporous structure and formation of large interparticle pores, agreeing with the results of pore size distributions, where the pore size distributions exhibit more and more wider peaks with the temperature increased. The WO_3 -bulk sample synthesized without DDA exhibited typical type II isotherms, characteristic of nonporous solids. The BET surface area is $24 \text{ m}^2 \text{ g}^{-1}$ at 400 °C, which is noticeably low compared to the mesoporous WO_3 -DDA, summarizing in Table 4.

The transmission electron microscopic (TEM) image of WO_3 -DDA sample calcined at 400°C (Figure 4A) shows the small interparticle mesoporous between the

crystalline WO_3 particles. WO_3 -DDA sample crystallized at 500 °C shows the complete collapse of the small interparticle mesoporous and the existence of only WO_3 particles (Figure 4B). A representative high-resolution TEM (HRTEM) images (Figure 4C) of mesoporous WO_3 -DDA sample crystallized at 400 °C exhibits that the pores were composed of randomly oriented crystalline particles of an estimated size in the range of 4-7 nm .

EDS data as shown in Figure 5, where the assignment the peak at 0.4 eV is somewhat unclear, and it could possibly be due to either a $K\alpha$ for N or to some minor band for O. This assignment is significant to prove the presence of N into WO_3 lattice whether or not and possibly a measurement of the local content of N. In order to assign the peak at 0.4 eV, the EDS results of DDA- WO_3 samples was analyzed carefully by dividing the peaks overlapping each other to calculate the N content. For comparison of WO_3 -bulk sample which no N signal was detected, the DDA-derived precursor gave a signal of N and the molar ratio of W : N was 1 : 0.59. But the molar ratio of W : N decreased gradually with the calcination temperature increased, the molar ratio of W : N was 1 : 0.007 as the calcined at 500°C, summarized in Table 5.

XRD data of WO_3 -bulk and WO_3 -DDA samples calcined from 400~550 °C are shown in Figure 6. Both the WO_3 -bulk (Figure 6A) and WO_3 -DDA (Figure 6B) samples revealed crystallization of the framework after calcination at 400 °C and the degree of crystallization increased with the calcination temperature increased. XRD peaks of both WO_3 -DDA and WO_3 -bulk were agree with phase-pure monoclinic WO_3 (JCPDS number: 01-072-0667) well. The crystallite diameter based on [120]

reflections (D_{120}) for both WO_3 -bulk and WO_3 -DDA samples were estimated according to the following Scherrer equation:

$$D_{hkl} = \frac{K\lambda}{\beta \cos \theta}$$

Where K is Scherrer constant, assumed as 0.9, λ is wavelength of X-ray (0.154 nm), β is half value width ($^\circ$) and θ is diffraction angle ($^\circ$). The results were summarized in Table 6, where All of the crystallite diameter for WO_3 -DDA samples were bigger compare with WO_3 -bulk samples, suggest that WO_3 -DDA samples own higher crystallinity compare to WO_3 -bulk samples.

In order to reveal the effect of N_2 intercalation on the crystal lattice, lattice parameter of WO_3 -bulk and WO_3 -DDA samples prepared at various calcination temperatures were analyzed (Figure 7). The 002, 020, and 200 peak positions reflect the a , b , and c lattice parameter, respectively. In Figure 7A, WO_3 -bulk samples exhibited no change for both the lattice parameters of a , b and c (7.31, 7.54 and 7.69) and lattice volume of 135.33 \AA^3 in spite of calcination changing, however, WO_3 -DDA samples exhibited noticeable change for the the lattice parameters with the calcination temperature increased except calcination at 400 $^\circ\text{C}$ (Figure 7B). And also, both the $a:b$ ratio and lattice volume of WO_3 -DAA samples exceeded that of WO_3 -bulk samples from 450 $^\circ\text{C}$, signifying that N_2 intercalation occurred from 450 $^\circ\text{C}$. However, the $a:b$ ratio decreased from 0.9705 to 0.9698 (Figure 7C) and lattice volume (Figure 7D) decreased from 161.63 \AA^3 to 143.87 \AA^3 with increasing the calcination temperature due to the decrease of N content, which is corresponding the EDS results.

Raman spectra of the WO_3 -DDA sample prepared at various calcination

temperatures are shown in Figure 8. Raman spectra of the WO₃-DDA samples exhibited the characteristic signals of the monoclinic phase of peaks at 139.9 cm⁻¹ (lattice vibration), 276.5 cm⁻¹ (δ (O-W-O) deformation vibration), 697.1 cm⁻¹ and 799.2 cm⁻¹ (O-W-O) stretching vibration) in a range of Raman shift from 100 ~ 1000 cm⁻¹ (Figure 8A). This results are good agreement with the XRD patterns of the WO₃-DDA samples measured by various calcination temperatures. In a region of 2200 ~2400 cm⁻¹ (Figure 8B) no signal was detected for the WO₃-DDA sample calcined at less than 400 °C, but the peaks at 2328 ~ 2330 cm⁻¹ assigned to the N≡N vibration intercalated into the WO₃ lattice^{31, 50-52} were started to observe from 450 °C. The results of Raman are good agreement with the XRD analysis results of lattice.

For comparison with WO₃-DDA samples, Raman spectra of the WO₃-bulk samples exhibited the characteristic signals of the monoclinic phase alone in a range of 100 ~ 1000 cm⁻¹ (Figure 9), being consistent with the XRD data. In a region of 2200 ~2400 cm⁻¹ (Figure 9B) no signal of the presence of N≡N were detected.

DRS data of the WO₃ -DDA samples prepared from 400 °C-550 °C and WO₃-bulk sample prepared at 550°C are shown in Figure 10. In this UV-vis DR spectra, noticeable red-shift of fundamental absorption edge were observed for WO₃-DDA samples (487 nm) comparing with the WO₃-bulk sample (443 nm), but except the WO₃-DDA sample calcined at 400 °C due to carbon from DDA template was not completely decomposed. As a perhaps explanation for red-shift of fundamental absorption edge, the band structure of WO₃ will be altered, which a new

N 2p energy level would be formed above the valence band of WO₃ after N₂ molecule intercalation into the crystal lattice of WO₃. The fundamental absorption edge decreased with increasing the calcination temperature due to the contents of N₂ molecule decreased with the calcination temperature increased, corresponding to the results of EDS and XRD analysis results of lattice.

TG analysis offer evidence of overall ~38% weight loss of the DDA-derived precursor in the temperature range from 50 to 500 °C (Figure 11). The TG profile of DDA-derived precursor exhibited four weight loss steps and four endothermic peaks: the first step weight loss of about 21% occurred up to 289 °C due to the removal of adsorbed water and the decomposition of DDA template. The second weight loss of about 2% occurred from 289 °C to 306 °C due to decomposition of DDA which was decomposed completely at the first step. The third step weight loss of about 4% between 306 °C and 395 °C could be ascribed to with the conversion of the precursor to WO₃. The last step weight loss of about 11% occurred from 395 °C to 450 °C could be associated with the N₂ intercalation to form N₂·WO₃ and subsequent crystallization of N₂·WO₃.

SEM images of the ITO/WO₃ film prepared DDA-derived precursor under typical condition and then calcined at 500°C are shown in Figure 12. The SEM images of the top-view at low magnification (Figure 12a) exhibit smooth porous network without any significant crack formation. The SEM images at low magnification (Figure 12b) exhibits that a mesoporous network is composed of tiny spherical WO₃ particles of *ca.* 5 to 20 nm in diameter, being well connected to each other. The film

thickness was measured to be *ca.* 13 μm from the cross-sectional SEM image (Figure 12c).

The PEC properties of the ITO/ WO_3 electrodes were studied in a 0.1 M phosphate solution (pH=6.0). Figure 13 shows the CVs of the ITO/ WO_3 electrodes. On CVs of WO_3 -DDA sample calcined at 500 $^{\circ}\text{C}$ (Figure 13), no redox response was observed in the dark in a potential range of 0.4~1.0 V versus Ag/AgCl except for a response based on $\text{WO}_3/\text{H}_x\text{WO}_3$ below 0.2 V. The photoanodic currents due to water oxidation were observed upon visible light irradiation above onset potentials of 0.2 V versus Ag/AgCl and reached 1.5 mA cm^{-2} at 1.0 V versus Ag/AgCl, which is 4.3 times higher than that (0.35 mA cm^{-2} at 1.0 V versus Ag/AgCl) of WO_3 -bulk in spite of the degradation of mesoporous structure for WO_3 -DDA sample calcined at 500 $^{\circ}\text{C}$.

The relationship between calcination temperatures and photoanodic currents at 1.0 V vs. Ag/AgCl was plotted using standard deviations, as shown in Figure 14. The photocurrent increased with increasing the calcination temperature for both WO_3 -DDA and WO_3 -bulk samples. The photocurrent of WO_3 -DDA ($0.04 \pm 0.02 \text{ mA cm}^{-2}$) calcined at 400 $^{\circ}\text{C}$ is similar to WO_3 -bulk ($0.02 \pm 0.01 \text{ mA cm}^{-2}$), though the mesoporous structure was formed for WO_3 -DDA sample. It demonstrate that crystallinity is the dominant factor for PEC water oxidation rather than porosity for samples calcied at 400 $^{\circ}\text{C}$. With the calcination increased above 450 $^{\circ}\text{C}$, the photocurrents of WO_3 -DDA samples are significant higher than that of WO_3 -bulk samples. The photocurrent ($1.26 \pm 0.05 \text{ mA cm}^{-2}$) of WO_3 -DDA is about 4.3 times higher than that ($0.30 \pm 0.03 \text{ mA cm}^{-2}$) of WO_3 -bulk sample. Three possible reasons

are given here, (1) mesoporous-structured WO₃-DDA having high surface area which can separate the electron and hole pairs well to reduce the possibility of recombining before participating in a water oxidation reaction at the WO₃ surface, (2) visible light can be used sufficiently to improve the PEC water oxidation performance after N₂ intercalation, (3) WO₃-DDA sample owns higher crystallinity which is the dominant factor for PEC water oxidation than the WO₃-bulk calcined at 450°C. The photocurrents of WO₃-DDA and WO₃-bulk calcined at 550°C are $1.38 \pm 0.05 \text{ mA cm}^{-2}$ and $0.57 \pm 0.06 \text{ mA cm}^{-2}$, respectively, therefore, the photocurrents ratio between WO₃-DDA and WO₃-bulk decreased to 2.4 as calcined at 550°C due to (1) mesoporous structure is decomposed above 500°C so that the surface area decreases, (2) the contents of N₂ decrease with the calcination temperature increase, (3) also the crystallinity of WO₃-bulk becomes higher with the calcination temperature increase, and thus the photocurrent increases.

Figure 15 shows action spectra of the IPCE at 0.5 V versus Ag/AgCl using different ITO/WO₃ electrodes calcined at 500 °C. Photocurrent was not observed above 470 nm for WO₃-bulk samples, however, the photocurrent was observed below 490 nm for WO₃-DDA samples. The on-set wavelength of 490 nm of action spectrum corresponds to the absorption edge of the diffused reflectance spectrum of the WO₃-DDA sample, corroborating that the photoanodic current is based on a band gap photoexcitation of N 2p-W 5d. At the crystallization temperature of 500 °C, a remarkable higher IPCE for WO₃-DDA (32%) at 400 nm are observed, which is about 4.6 times higher compared to that of WO₃-bulk (7%).

The IPCE values at 420 nm for both WO₃-DDA and WO₃-bulk samples and the ratio of IPCE are plotted in Figure 16, where the the IPCE values increased with the calcination increased, the ratio of IPCE decreased with calcination temperature increased above 500°C. The IPCE value at 420 nm for WO₃-DDA is about 25%, which is 10 times than that (5%) of WO₃-bulk sample calcined at 450°C. After that, the ratio show the decrease tendency due to the decomposition of mesoporous structure and N₂ contents decrease at high calcination temperature.

Photoelectrocatalysis over the ITO/WO₃ electrodes was conducted in a 0.1 M phosphate solution (pH = 6.0) under potentiostatic conditions at 0.5 V versus Ag/AgCl for 1 h upon visible light irradiation ($\lambda > 390$ nm, 100 mW cm⁻²). The photocurrent-time profiles of both WO₃-DDA and WO₃-bulk calcined at 500 °C are shown in Figure 17. Higher initial photocurrents were observed upon illumination for both of WO₃ electrodes, but the photocurrents were not stable and began to decay over time due to accumulation of peroxo species on WO₃ surface⁵³. The photocurrent density of WO₃-DDA (Figure. 17b) at 2 min was 0.58 mA cm⁻², which is 2.9 times higher than that of the WO₃-bulk (0.20 mA cm⁻² at 2 min, Figure. 17d) electrode. The charge amount passed during 1h photoelectrocatalysis for WO₃-DDA (0.93 C) was 3.9 times higher than that of WO₃-bulk (0.24 C). As a consequence of the high charge amount, the markedly high amount ($n_{O_2} = 1.8$ μmol, Faradaic efficiency (FE_{O2}) = 75%) of O₂ evolved for the WO₃-DDA electrode compared to that ($n_{O_2} = 0.33$ μmol, FE_{O2} = 55%) of the WO₃-bulk electrode, as summarized in Table 7. The improvement of PEC water oxidation at a hematite photoanode was reported by adding Co²⁺ ions in an

electrolyte solution.⁵⁴ In the presence of 0.1 mM Co^{2+} ions in the phosphate buffer solution of pH=6.0, the PEC water oxidation performances were enhanced for both WO_3 -DDA electrode (Figure. 17a) and WO_3 -bulk electrode (Figure. 17c) compare those in the absence of Co^{2+} ions (Table 7). The enhancement of the mesoporous WO_3 -DDA photoanode is attributed to its high surface-to-volume ratio which offers a large number of water oxidation sites at the electrolyte- WO_3 interface, and well-connected WO_3 particles for efficient electron transport through the film. Otherwise, N_2 intercalated WO_3 -DDA can use the visible light ($\lambda > 490$ nm) efficiently to increase the PEC performance of water oxidation. The enhancement of WO_3 -bulk photoanode would be explained by acceleration of water oxidation reaction at the WO_3 surface by Co^{2+} absorbed.

4.4 Conclusions

A unique N_2 -intercalated WO_3 with a mesoporous structure was synthesized by employing an facile one-step hydrothermal treatment procedure using DDA, which was used as a nitrogen source as well as a surfactant template for formation of mesoporous structure. The mesoporous N_2 -intercalated WO_3 show higher surface area and crystallinity compared to the untemplated WO_3 . Therefore, mesoporous N_2 -intercalated WO_3 showed 4.3 times higher photoanodic current and provided the enhancement towards performance of PEC water oxidation. The IPCE was enhanced by N_2 intercalation and gave a on-set wavelength of 490 nm.

4.5 References

1. X. Chen, J. Ye, S. Ouyang, T. Kako, Z. Li and Z. Zou, *ACS Nano*, 2011, 5,

4310-4318.

2. A. Kudo and Y. Miseki, *Chem. Soc. Rev.*, 2009, 38, 253-278.
3. P. Kamat, K. Tvrđy, D. Baker and J. Radich, *Chem Rev*, 2010, 110, 6664.
4. A. Fujishima and K. Honda, *Nature*, 1972, 238, 37.
5. Z. Zou, J. Ye, K. Sayama and H. Arakawa, *Nature*, 2001, 414, 625-627.
6. K. Maeda, K. Teramura, D. Lu, T. Takata, N. Saito, Y. Inoue and K. Domen, *Nature*, 2006, 440, 295-295.
7. M. Gratzel, *Nature*, 2001, 414, 338-344.
8. C. Aprile, A. Corma and H. Garcia, *Phys Chem Chem Phys*, 2008, 10, 769.
9. D. Chandra, K. Saito, T. Yui and M. Yagi, *Angew. Chem. Int. Ed.*, 2013, 52, 12606-12609.
10. H. Kim, P. Borse, J. Jang, C. Ahn, E. Jeong and J. Lee, *Adv Mater*, 2011, 23, 2088.
11. K. Ng, L. Minggu and M. Kassim, *Int. J. Hydrogen Energy*, 2013, 38, 9585.
12. J. Kim, K. Shin, S. Cho, T.-W. Lee and J. Park, *Energy Environ Sci*, 2011, 4, 1465.
13. P. Chatchai, Y. Murakami, S.-y. Kishioka, A. Nosaka and Y. Nosaka, *Electrochim Acta*, 2009, 54, 1147.
14. T. Hisatomi, H. Dotan, M. Stefić, K. Sivula, A. Rothschild, M. Gratzel and N. Mathews, *Adv Mater*, 2012, 24, 2699.
15. V. Satsangi, S. Kumari, A. Singh, R. Shrivastav and S. Dass, *Int. J. Hydrogen Energy*, 2008, 33, 312.

16. G. Rahman and O.-S. Joo, *Int. J. Hydrogen Energy*, 2012, 37, 13989.
17. Y. Li, T. Takata, D. Cha, K. Takanabe, T. Minegishi, J. Kubota and K. Domen, *Adv. Mater.*, 2013, 25, 125-131.
18. K. Maeda, M. Higashi, D. Lu, R. Abe and K. Domen, *J. Am. Chem. Soc.*, 2010, 132, 5858-5868.
19. K. Maeda and K. Domen, *Angew. Chem. Int. Ed.*, 2012, 51, 9865-9869.
20. T. Abe, K. Nagai, S. Kabutomori, M. Kaneko, A. Tajiri and T. Norimatsu, *Angew. Chem. Int. Ed.*, 2006, 45, 2778-2781.
21. B. Yang, Y. Zhang, E. Drabarek, P. Barnes and V. Luca, *Chem. Mater.*, 2007, 19, 5664.
22. J. Seabold and K.-S. Choi, *Chem Mater*, 2011, 23, 1105.
23. M. Yagi, S. Maruyama, K. Sone, K. Nagai and T. Norimatsu, *J Solid State Chem*, 2008, 181, 175.
24. Y. Miseki, H. Kusama, H. Sugihara and K. Sayama, *J Phys Chem Lett*, 2010, 1, 1196.
25. Y. Miseki, S. Fujiyoshi, T. Gunji and K. Sayama, *Catal. Sci. Tech.*, 2013, 3, 1750-1756.
26. M. Radecka, P. Sobas, M. Wierzbicka and M. Rekas, *Phys. B*, 2005, 364, 85-92.
27. A. Hameed, M. A. Gondal and Z. H. Yamani, *Catal. Commun.*, 2004, 5, 715-719.
28. Y. Sun, C. J. Murphy, K. R. Reyes-Gil, E. A. Reyes-Garcia, J. M. Thornton, N.

- A. Morris and D. Raftery, *Int. J. Hydrogen Energy*, 2009, 34, 8476-8484.
29. B. Cole, B. Marsen, E. Miller, Y. Yan, B. To, K. Jones and M. Al-Jassim, *J. Phys. Chem. C*, 2008, 112, 5213-5220.
 30. W. Li, J. Li, X. Wang and Q. Chen, *Appl. Surf. Sci.*, 2012, 263, 157-162.
 31. Q. Mi, Y. Ping, Y. Li, B. Cao, B. S. Brunschwig, P. G. Khalifah, G. A. Galli, H. B. Gray and N. S. Lewis, *J. Am. Chem. Soc.*, 2012, 134, 18318-18324.
 32. C. Santato, M. Odziemkowski, M. Ulmann and J. Augustynski, *J. Am. Chem. Soc.*, 2001, 123, 10639-10649.
 33. S. Berger, H. Tsuchiya, A. Ghicov and P. Schmuki, *Appl Phys Lett*, 2006, 88, 203119.
 34. R. Colton, A. Guzman and J. Rabalais, *J Appl Phys*, 1978, 49, 409.
 35. B. Yous, S. Robin, A. Donnadieu, G. Dufour, C. Maillot, H. Roulet and C. Senemaud, *Mater Res Bull*, 1984, 19, 1349.
 36. C. Santato, M. Ulmann and J. Augustynski, *J. Phys. Chem. B*, 2001, 105, 936-940.
 37. S. Berger, H. Tsuchiya, A. Ghicov and P. Schmuki, *Applied Physics Letters*, 2006, 88, -.
 38. J. K. Kim, K. Shin, S. M. Cho, T.-W. Lee and J. H. Park, *Energy Environ. Sci.*, 2011, 4, 1465-1470.
 39. R. Sivakumar, A. Moses Ezhil Raj, B. Subramanian, M. Jayachandran, D. Trivedi and C. Sanjeeviraja, *Mater Res Bull*, 2004, 39, 1479.
 40. H. Chen, J. Gu, J. Shi, Z. Liu, J. Gao, M. Ruan and D. Yan, *Adv. Mater.*, 2005,

- 17, 2010-2014.
41. X. Cai, G. Zhu, W. Zhang, H. Zhao, C. Wang, S. Qiu and Y. Wei, *Eur. J. Inorg. Chem.*, 2006, 2006, 3641-3645.
 42. D. Zhao, P. Yang, B. F. Chmelka and G. D. Stucky, *Chem. Mater.*, 1999, 11, 1174-1178.
 43. A. Dong, Y. Wang, Y. Tang, N. Ren, Y. Zhang, Y. Yue and Z. Gao, *Adv. Mater.*, 2002, 14, 926-929.
 44. H. Li, Z. Bian, J. Zhu, D. Zhang, G. Li, Y. Huo, H. Li and Y. Lu, *J. Am. Chem. Soc.*, 2007, 129, 8406-8407.
 45. J. K. Kim, J. H. Moon, T.-W. Lee and J. H. Park, *Chem. Commun.*, 2012, 48, 11939-11941.
 46. X. Cui, J. Shi, H. Chen, L. Zhang, L. Guo, J. Gao and J. Li, *J. Phys. Chem. B*, 2008, 112, 12024-12031.
 47. J. C. Yu, X. Wang and X. Fu, *Chem. Mater.*, 2004, 16, 1523-1530.
 48. D. Li, D. Chandra, K. Saito, T. Yui and M. Yagi, *Nanoscale Res. Lett.*, 2014, 9, 542.
 49. A. Grosman and C. Ortega, *Langmuir*, 2008, 24, 3977-3986.
 50. F. Tessier, L. Le Gendre, F. Cheviré R. Marchand and A. Navrotsky, *Chem. Mater.*, 2005, 17, 3570-3574.
 51. S. G. Ebbinghaus, H.-P. Abicht, R. Dronskowski, T. Müller, A. Reller and A. Weidenkaff, *Prog. Solid State Chem.*, 2009, 37, 173-205.
 52. A. Rachel, S. G. Ebbinghaus, M. Güngerich, P. J. Klar, J. Hanss, A.

- Weidenkaff and A. Reller, *Thermochim. Acta*, 2005, 438, 134-143.
53. J. A. Seabold and K.-S. Choi, *Chem. Mater.*, 2011, 23, 1105-1112.
54. A. Kay, I. Cesar and M. Grätzel, *J. Am. Chem. Soc.*, 2006, 128, 15714-15721.

Table 4-1 Physicochemical properties of WO₃ samples prepared from the precursors powder which were synthesized with / without DDA at 150°C followed by calcination at 400°C.

Sample	n _{H2WO4} : n _{DDA}	Surface area (m ² g ⁻¹)	Pore size (nm)	Pore volume (cm ³ g ⁻¹)
WO ₃ -Bulk	1 : 0	24.5	52.1	0.20
WO ₃ -DDA	1 : 0.25	28.2	4.4	0.07
WO ₃ -DDA	1 : 0.5	29.3	5.0	0.08
WO ₃ -DDA	1 : 1	53.6	4.9	0.10
WO ₃ -DDA	1 : 2.5	57.3	4.8	0.08
WO ₃ -DDA	1 : 5	31.2	4.8	0.09

Table 4-2 Physicochemical properties of WO₃-DDA samples prepared from the precursors powder which were synthesized at various preparation temperatures followed by calcination at 400°C.

Sample	Reaction temperature (°C)	Surface area (m ² g ⁻¹)	Pore size (nm)	Pore volume (cm ³ g ⁻¹)
DDA-WO ₃	80	23.3	5.5	0.12
DDA-WO ₃	120	46.6	5.1	0.09
DDA-WO ₃	150	57.3	4.8	0.08
DDA-WO ₃	180	34.1	4.4	0.04

Table 4-3 Physicochemical properties of WO₃-DDA samples calcined at different calcination temperatures.

Sample	Calcin. Temp. ^a / °C	Surface area (m ² g ⁻¹)	Pore size (nm)	Pore volume (cm ³ g ⁻¹)
WO ₃ -DDA	400	57.3	4.8	0.08
WO ₃ -DDA	450	24.2	24.5	0.09
WO ₃ -DDA	500	11.6	46.7	0.09
WO ₃ -DDA	550	6.57	94.3	0.08

^a Calcin. Temp. : Calcination temperature

Table 4-4 Physicochemical properties of WO₃-bulk samples under different calcination temperatures.

Sample	Calcin Temp. ^a / °C	Surface area (m ² g ⁻¹)	Pore size (nm)	Pore volume (cm ³ g ⁻¹)
WO ₃ -bulk	400	24.5	52.7	0.19
WO ₃ -bulk	450	18.7	51.6	0.23
WO ₃ -bulk	500	9.8	60.4	0.23
WO ₃ -bulk	550	5.4	197.1	0.14

^a Calcin. Temp. : Calcination temperature

Table 4-5 Summary of EDS data for different samples calcined at different calcination temperatures.

Sample name	Calcination temperature / °C	Molar ration of W: N
WO ₃ -bulk	500	1 : 0
As made	-	1 : 0.59
WO ₃ -DDA	400	1 : 0.060
WO ₃ -DDA	450	1 : 0.025
WO ₃ -DDA	500	1 : 0.012
WO ₃ -DDA	550	1 : 0.007

Table 4-6 The crystallite diameter of Bulk- WO_3 samples, and DDA- WO_3 samples

base on the (120) peak (D_{120}) calcined at 400 °C-550 °C.

Sample Temperature	Crystallite diameter (D_{120}) nm	
	WO_3 -bulk	WO_3 -DDA
400 °C	15	16
450 °C	18	21
500 °C	20	22
550 °C	24	27

Table 4-7 Summary of photoelectrocatalytic water oxidation in 0.1M phosphate buffer

(pH=6.0) using different WO₃ photoanodes crystallized at 500°C.

Samples	[Co ²⁺] / mM	Charge / C	<i>n</i> _{O₂} / μmol	F.E. _{O₂} ^a (%)	<i>n</i> _{H₂} ^b / μmol	F.E. _{H₂} ^c (%)
WO ₃ -bulk	0.1	0.47	0.71	57	2.27	92
WO ₃ -DDA	0.1	1.40	2.66	73	6.88	95
WO ₃ -bulk	0	0.24	0.36	58	1.05	87
WO ₃ -DDA	0	0.92	1.60	66	4.49	93

^aFaradic efficiency of O₂ evolution.

^b*n*_{H₂} is the amount of H₂ evolved in the Pt counter electrode compartment.

^cFaradic efficiency of H₂ evolution.

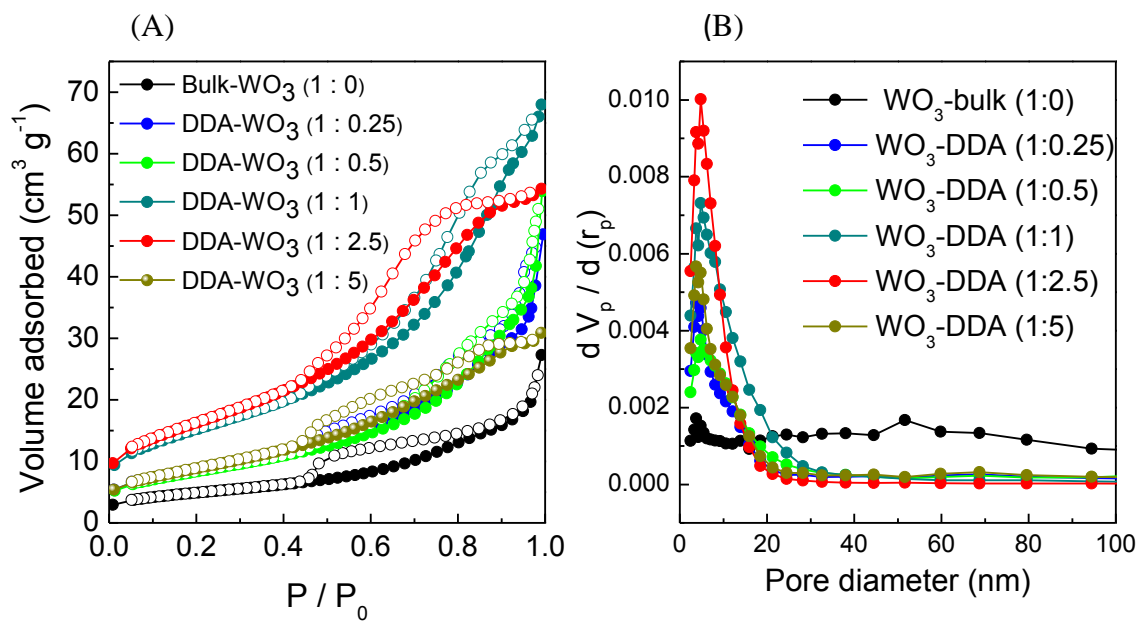


Figure 4-1 (A) N_2 sorption isotherms and (B) pore size distribution of WO_3 samples prepared from the different precursors powder which were synthesized with / without DDA at 150°C followed by calcination at 400°C .

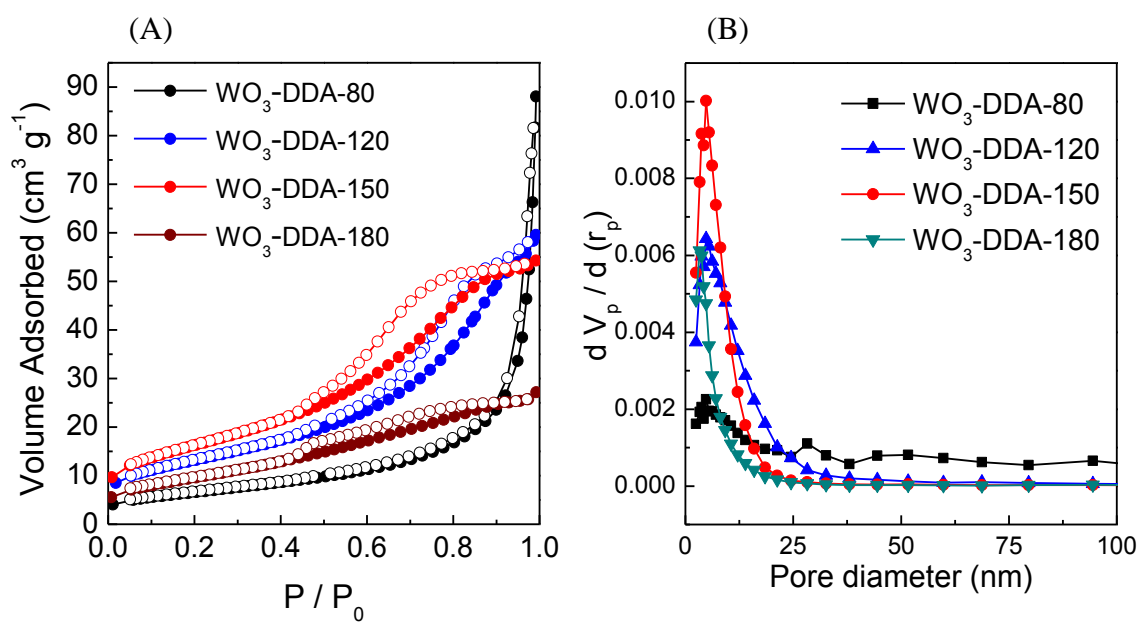


Figure 4-2 (A) N_2 sorption isotherms and (B) pore size distribution of WO_3 -DDA samples prepared from the different precursors powder which were synthesized at various preparation temperatures followed by calcination at 400°C .

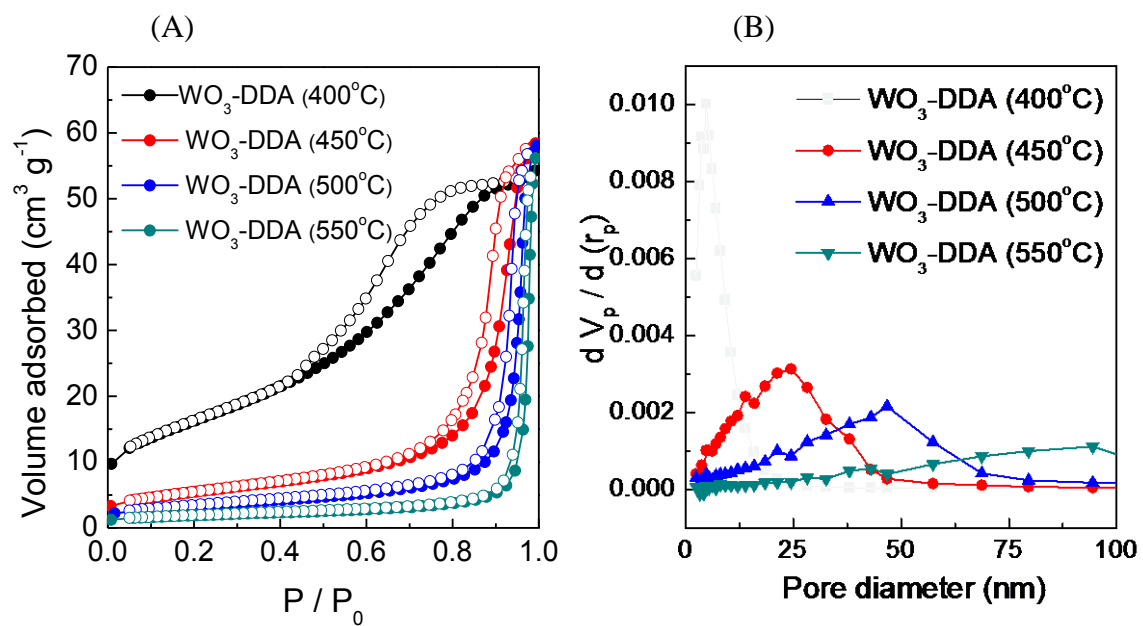


Figure 4-3 (A) N_2 sorption isotherms and (B) pore size distribution of WO_3 -DDA samples after being calcined at 400-550 °C.

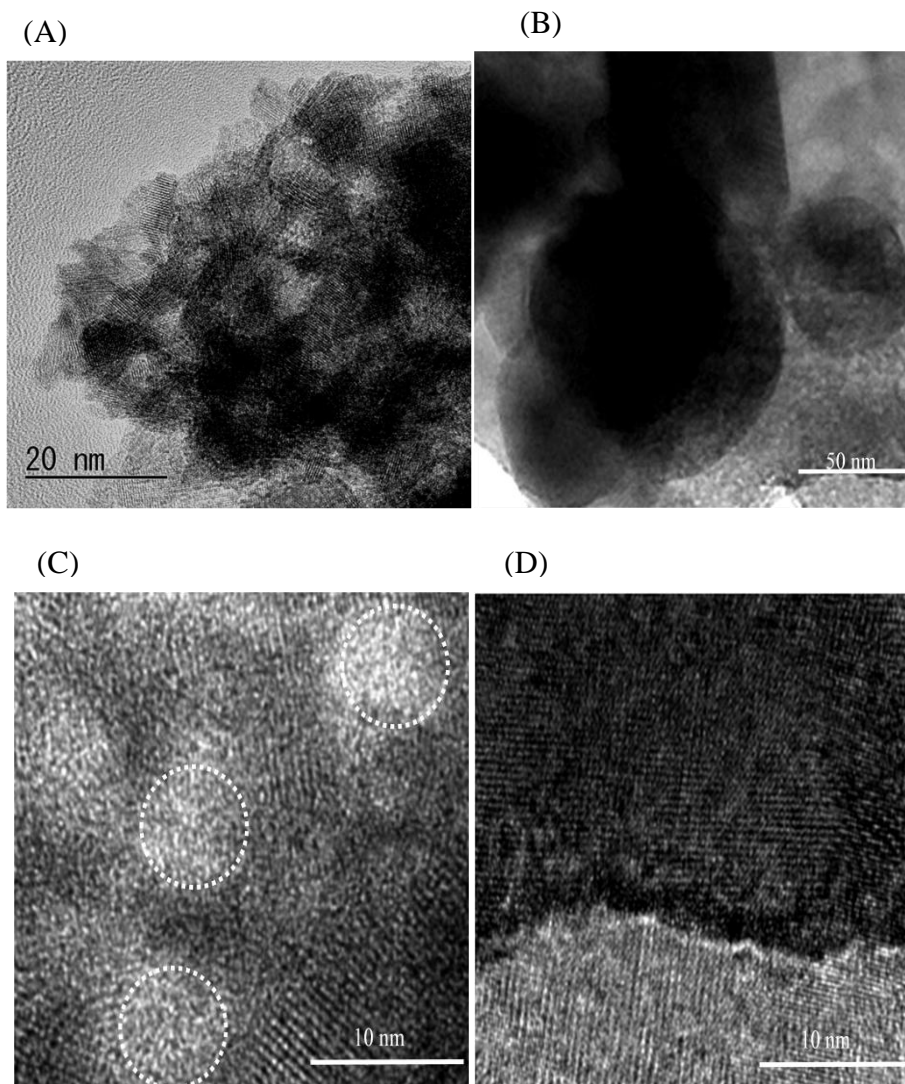


Figure 4-4 (A and B)TEM and (C and D) HRTEM images of WO_3 -DDA samples after being calcined at (left) 400 and (right) 550 °C. In the HRTEM images of WO_3 -DDA samples calcined at (C) 400°C a few pores are highlighted by white circles.

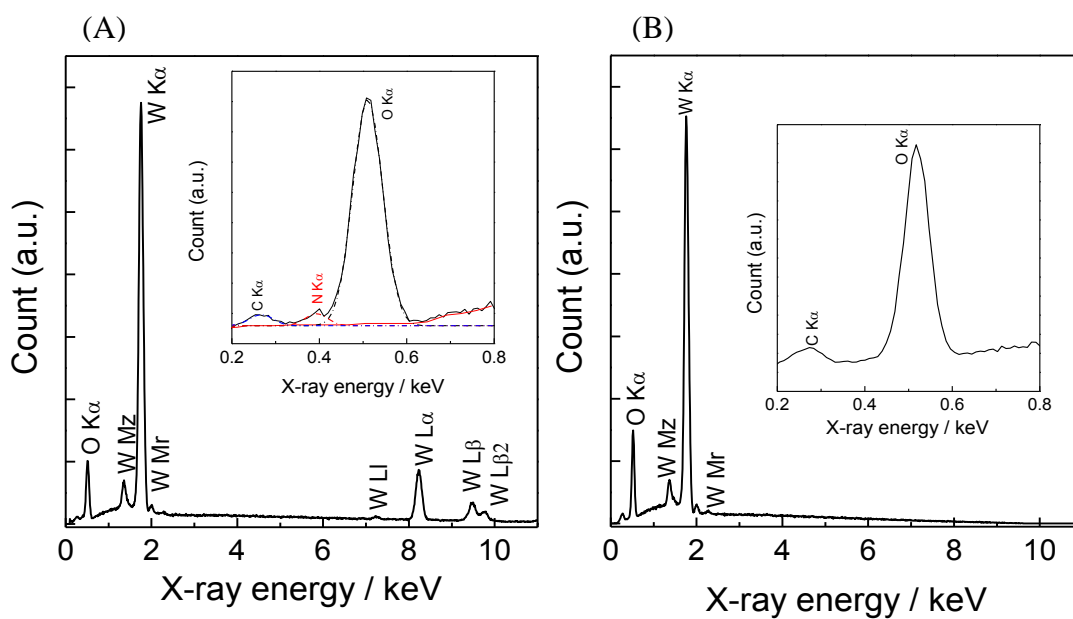


Figure 4-5 (A) EDS data of WO_3 -DDA sample after being calcined at 400°C and (inset) after analyzing carefully from 0.2-0.8 keV. (B) EDS data of WO_3 -bulk samples after being calcined at 400°C .

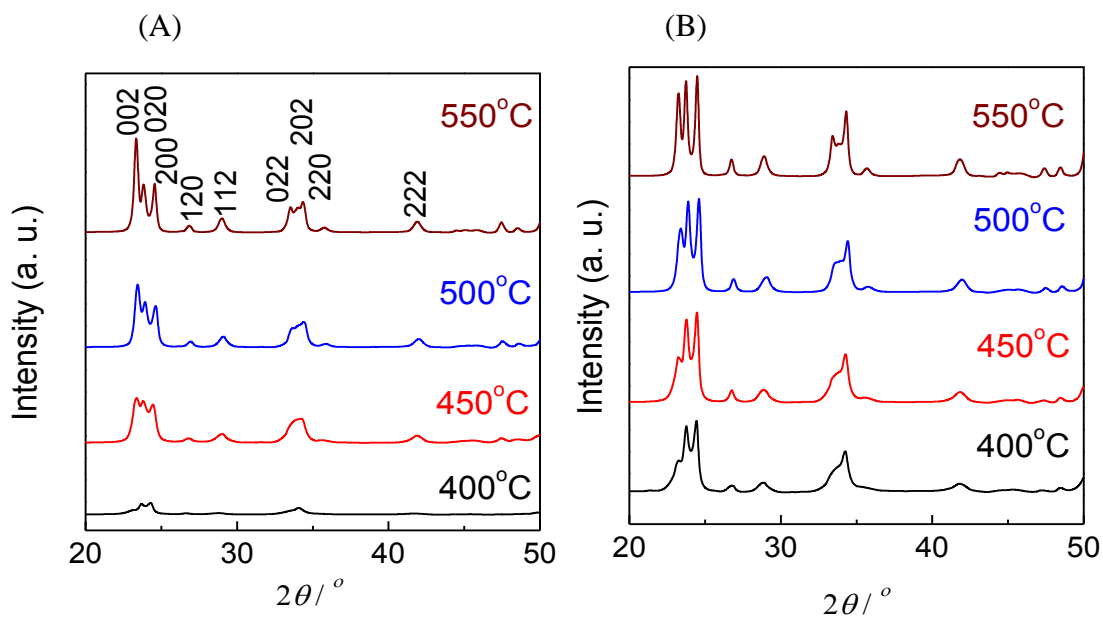


Figure 4-6 XRD patterns of (A) WO_3 -bulk and (B) WO_3 -DDA samples after being calcined at 400-500 °C. The 002, 020, and 200 peak positions reflect the a, b, and c lattice parameters, respectively.

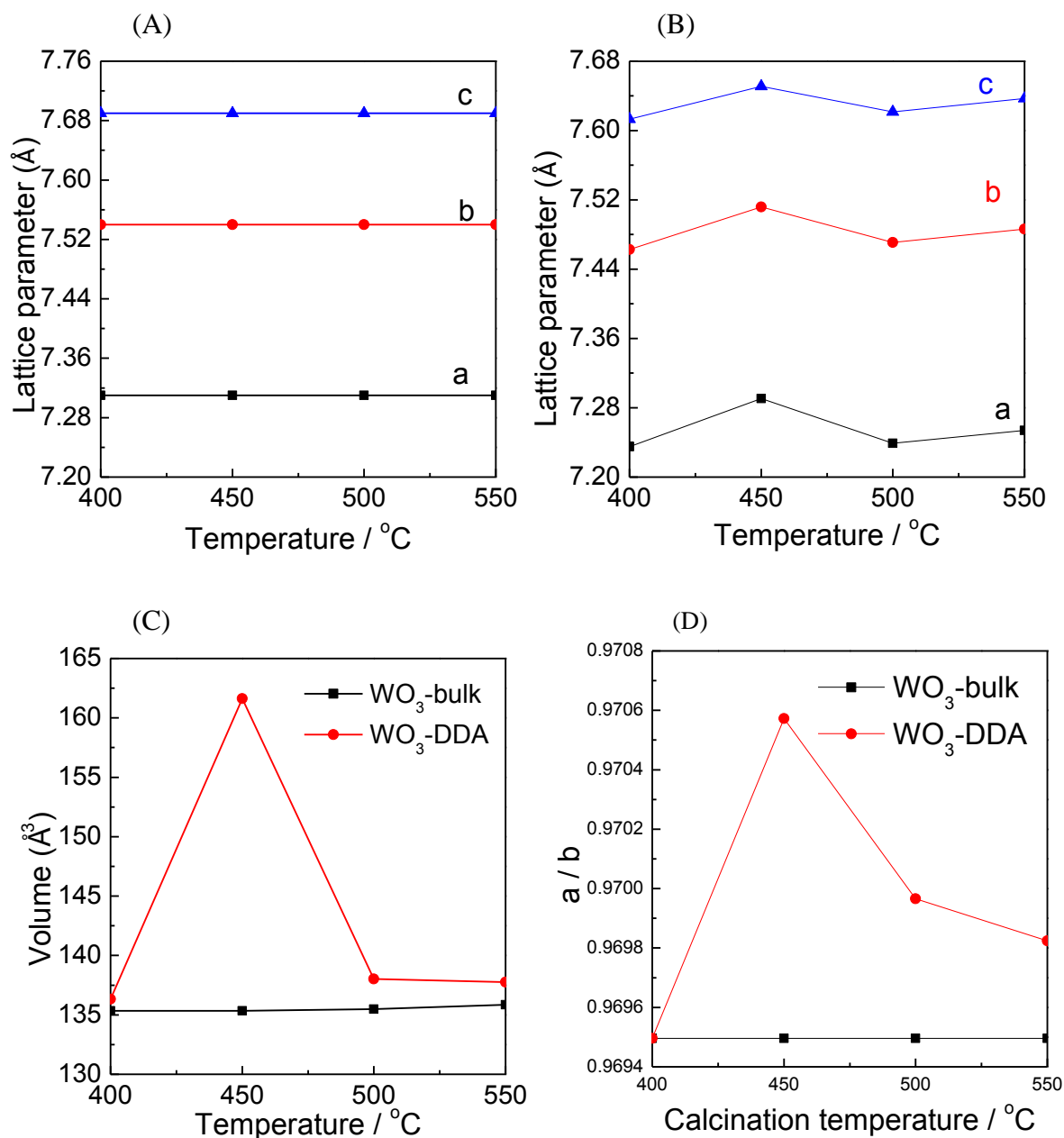


Figure 4-7 Lattice parameters of (A) WO_3 -bulk sample and (B) WO_3 -DDA sample annealed at 400-500°C, (C) the comparison towards lattice volume of WO_3 -bulk and WO_3 -DDA samples annealed at 400-500°C, and (D) the a:b ratio of WO_3 -bulk and WO_3 -DDA samples annealed at 400-500°C.

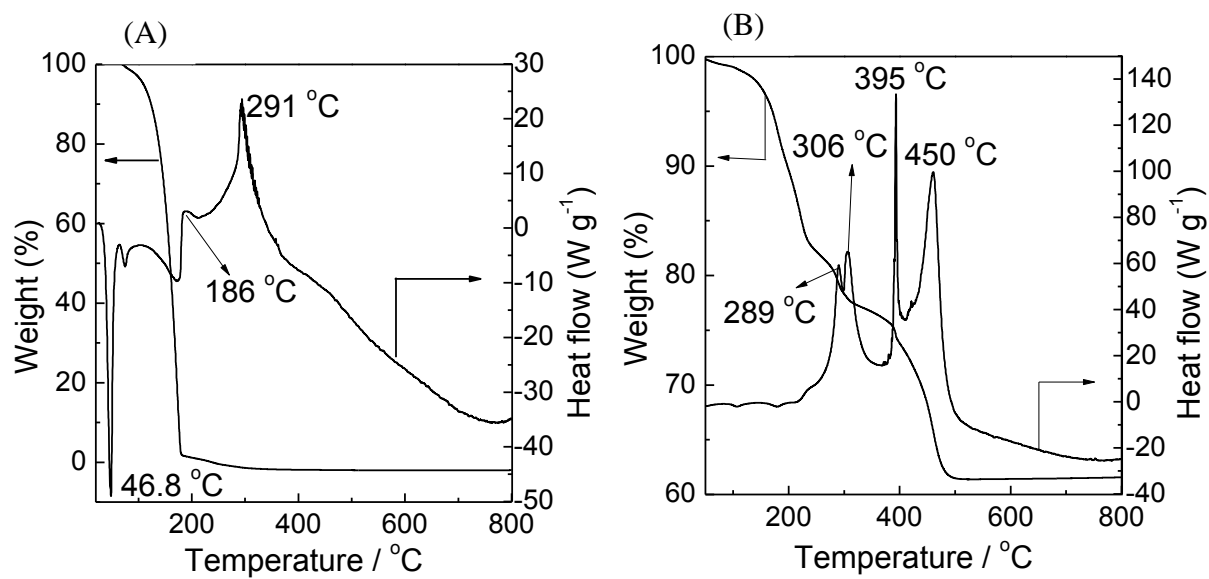


Figure 4-8 TG analysis of (A) DDA and (B) precursor powder which was synthesized from H_2WO_4 and DDA.

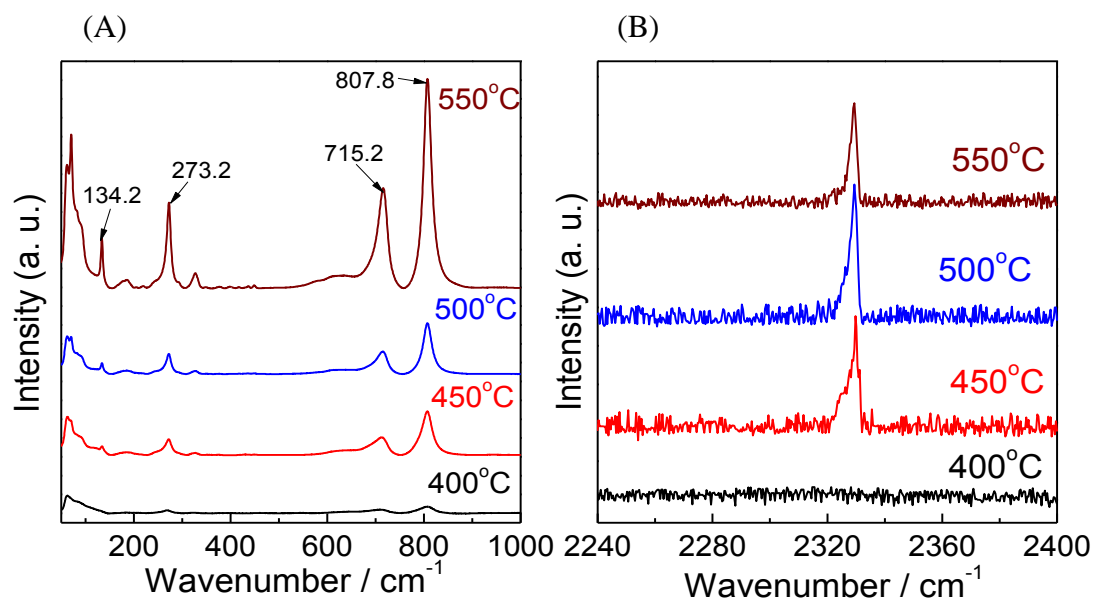


Figure 4-9 Raman spectra of (A) low wavenumber and (B) high wavenumber for WO_3 -DDA samples after being calcined at 400-500 °C.

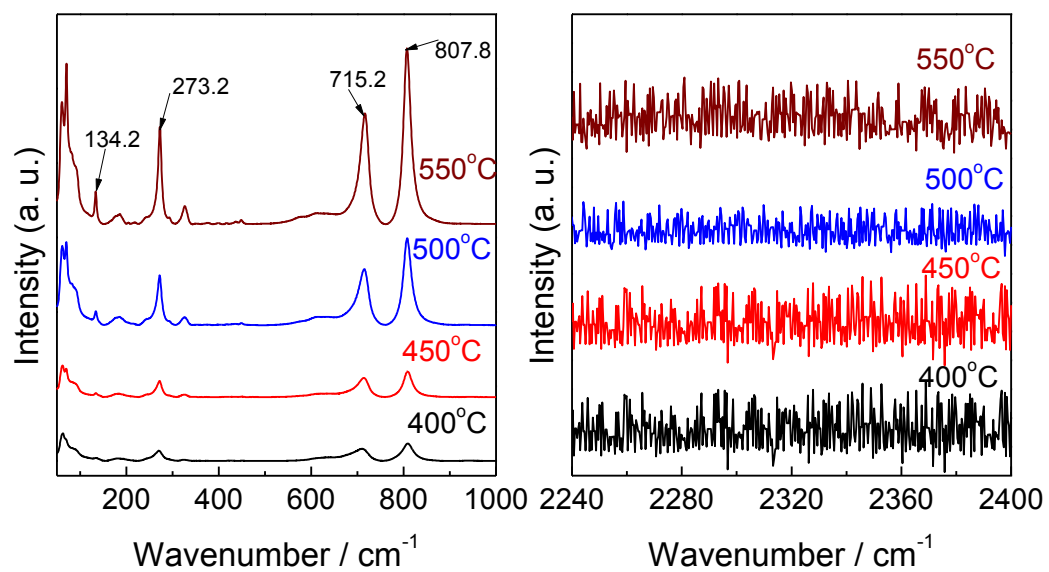


Figure 4-10 Raman spectra of (A) low wavenumber and (B) high wavenumber for WO_3 -bulk samples after being calcined at 400-500 °C.

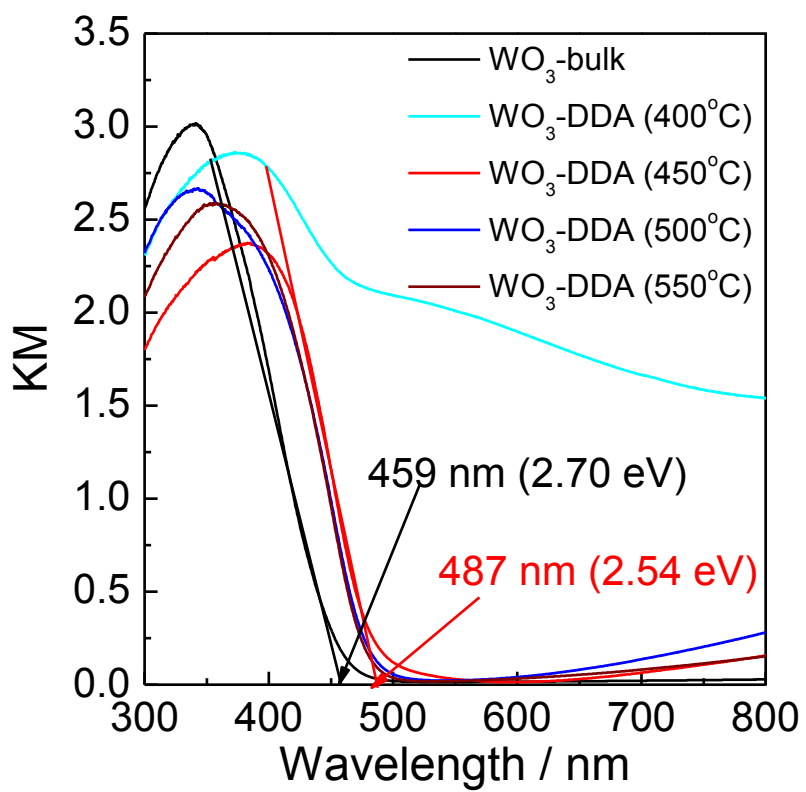


Figure 4-11 Diffuse reflectance spectra of (black) WO_3 -bulk sample calcined at 500°C and WO_3 -DDA samples calcined at 400 - 500°C .

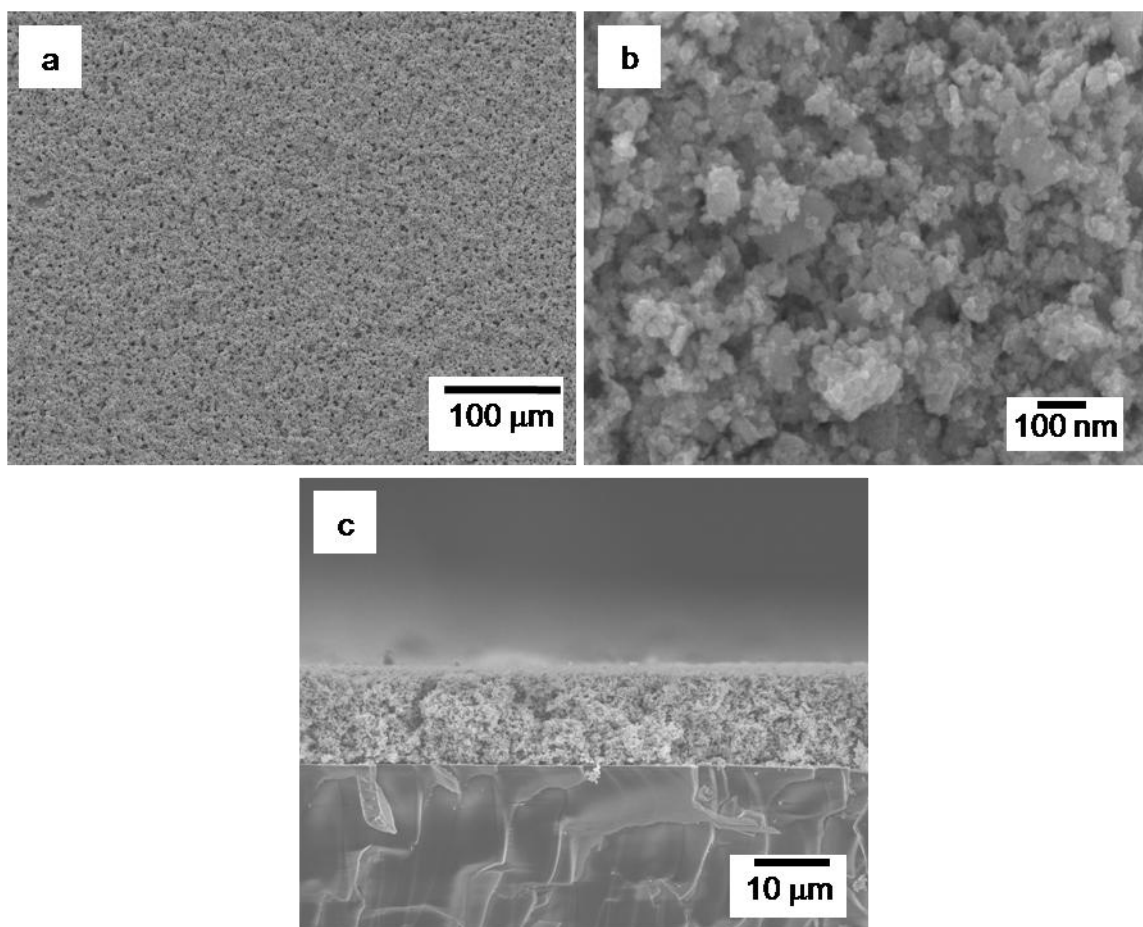


Figure 4-12 (a and b) Top view and (c) cross-sectional scanning electron microscopic (SEM) image of the ITO/ WO_3 -DDA electrode after being calcined at 500 $^\circ\text{C}$.

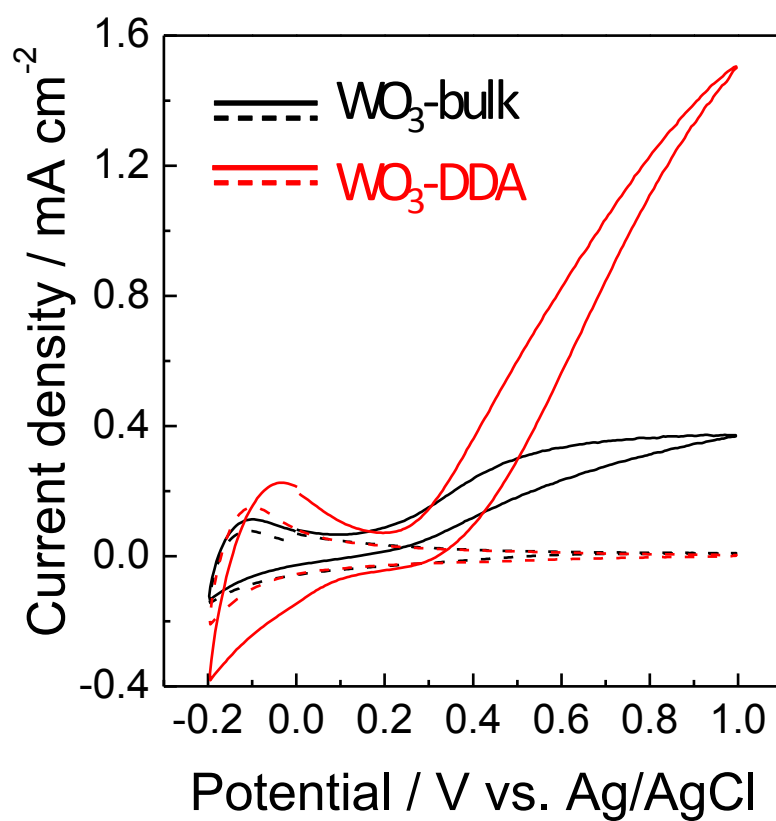


Figure 4-13 Cyclic voltammograms (CVs) for the samples calcined at 500 °C of the (red) ITO/ WO_3 -DDA and (black) ITO/ WO_3 -bulk electrodes in a 0.1 M phosphate buffer solution of pH = 6.0. The dashed and solid lines represents CV measured in the dark and on irradiation of visible light ($\lambda > 390 \text{ nm}$, 100 mW cm^{-2}), respectively.

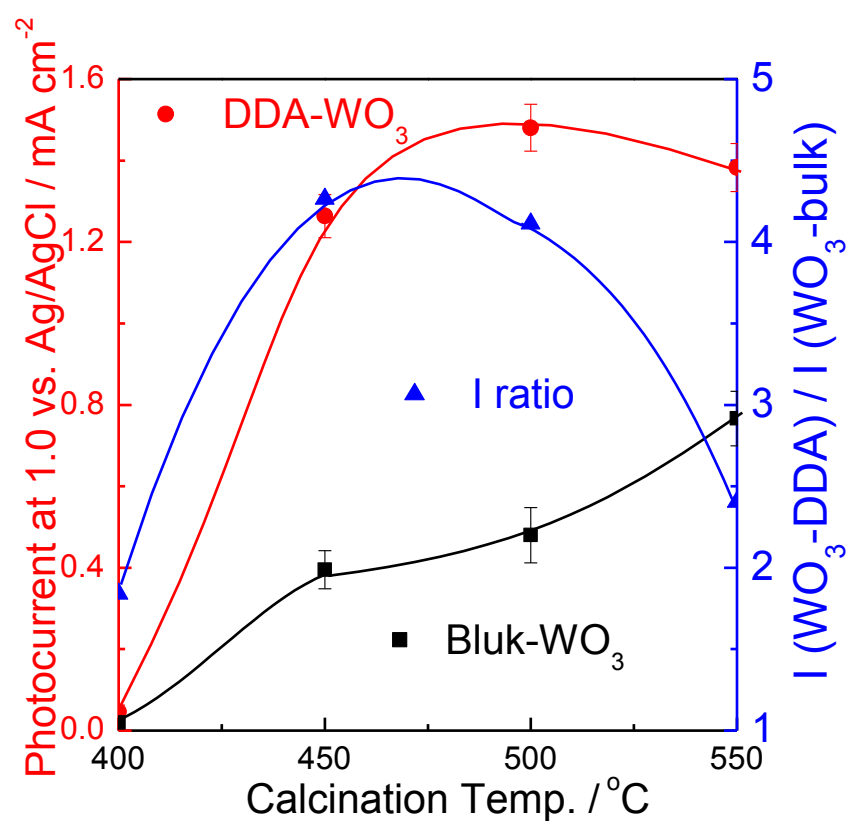


Figure 4-14 The relationship between calcination temperature and photocurrent at 1.0 V vs. Ag/AgCl for the the (red) ITO/WO₃-DDA and (black) ITO/WO₃-bulk electrodes. (blue) the ratio of photocurrent at 1.0 V vs. Ag/AgCl between the ITO/WO₃-DDA and ITO/WO₃-bulk electrodes.

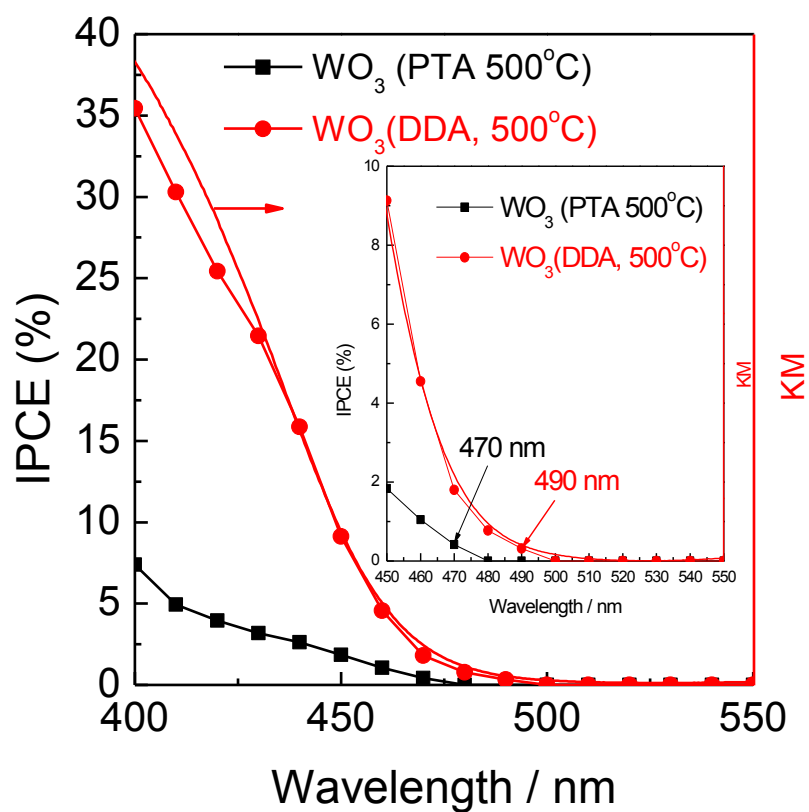


Figure 4-15 Action spectra of IPCE for the (red line and symbols) ITO/WO₃-DDA and (black line and symbols) ITO/WO₃-bulk electrodes in a 0.1 M phosphate buffer solution of pH = 6.0 at 0.5 V vs. Ag/AgCl. The red solid line which is marked by arrow shows is UV-visible diffuse reflectance spectra as Kubelka-Munk (KM) function of the ITO/WO₃-DDA electrodes.

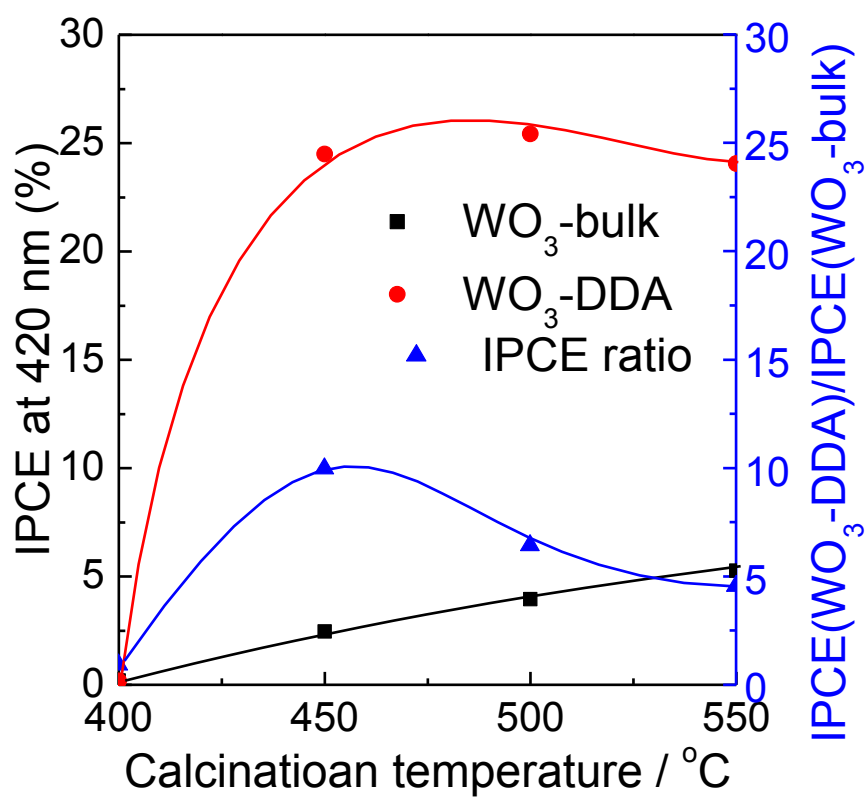


Figure 4-16 The comparison of IPCE values for the (red) ITO/WO₃-DDA and (black) ITO/WO₃-bulk electrodes after being annealed at 400-500°C. The blue line and symbols shows is the ratio of IPCE at at 420 nm between the ITO/WO₃-DDA and ITO/WO₃-bulk electrodes.

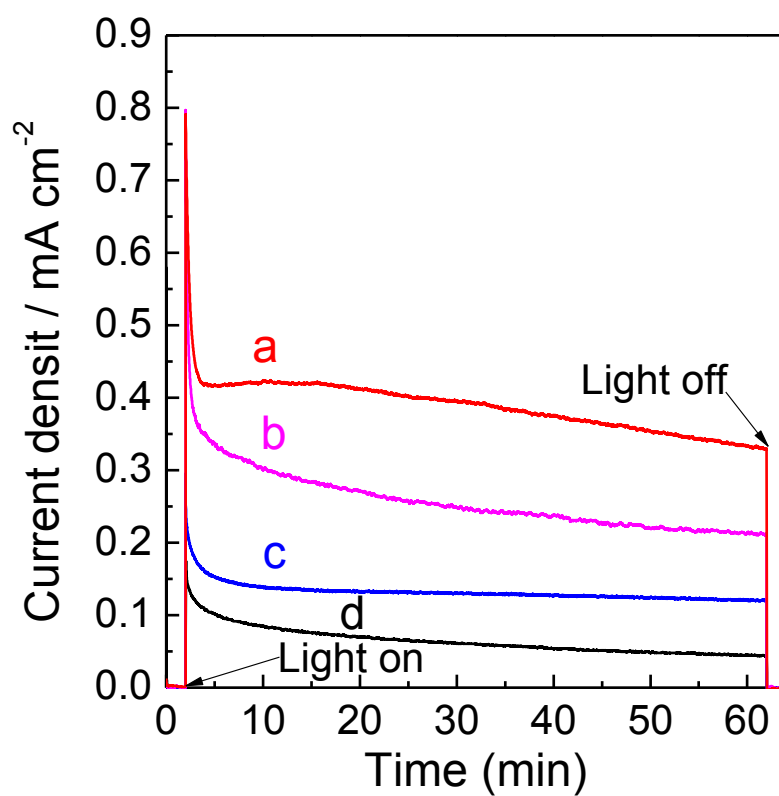


Figure 4-17 Photocurrent density-time profiles for the (pink and red) ITO/WO₃-DDA and (black and blue) ITO/WO₃-bulk electrodes in the (red and blue) presence and (pink and black) absence of 0.1 mM Co²⁺ ions in a 0.1 M phosphate buffer solution of pH 6.0 at 0.5 V vs. Ag/AgCl.

Chapter 5

**Nanorod architecture of N₂-intercalated WO₃
operated in wide-range of visible-light for highly
efficient photocatalytic and photoelectrochemical
water oxidation**

Chapter 5

Nanorod architecture of N₂-intercalated WO₃ operated in wide-range of visible-light for highly efficient photocatalytic and photoelectrochemical water oxidation

5.1 Introduction

Recently, solar water splitting using nano-structured materials as the photocatalyst have been received much attention, because of that clean, renewable and sustainable hydrogen fuel and oxygen will be produced from water by conversing abundant solar light directly.¹⁻³ Since oxidation of water is considering as energy demanding bottle-neck is in solar water splitting, a robust material with high efficient for water oxidation is necessary. For solar water splitting, intensive researches have been focused on nanostructured materials with narrow bandgaps including tungsten trioxide (WO₃)⁴⁻¹⁴. WO₃, an n-type semiconductor, has attracted immense attention as photocatalyst¹⁵⁻¹⁸ materials and photoanode materials for water oxidation in Photoelectrochemical (PEC) cells^{4,19-25} because of its visible light response (bandgap, $E_g = 2.6$ to 2.8 eV), a valence band edge position thermodynamically possible for water oxidation (about 3 V versus the normal hydrogen electrode), strong absorption within solar spectrum and good photochemical stability under the acidic conditions^{4,13,16,19,24,26-29}. Until now, many efforts have been devoted to the develop nanostructured WO₃, such as nanoparticles³⁰⁻³², nanoflakes^{23,33,34}, nanotubes³⁵, nanobelts³⁶, nanoplatelets¹⁹ and nanorods^{21,22,35}, to improve the PEC water oxidation performance. Among these, nanorods based WO₃ photoanodes will have a higher photocatalytic activities for water oxidation in comparison to the corresponding bulk one due to that nanorods can migrate electron fast along a rod axis between the interfaces of electrolyte and photoanode to reduce the chance of recombination during

the migration of electron and enhance the PEC water oxidation performance. But as a photoanode material, the band gap of pure WO_3 is still too large to realize a sufficient absorption of solar energy. So far, a lot of works have reported to improve visible light absorption through incorporation of dopants, such as, transition metal (Ti, Fe, Co, Ni, Cu, Zn),^{37,38} other metals (Ga, Dy, Te, Ta, V, Ce)³⁹⁻⁴⁴ and representative elements (N, C, S)⁴⁵⁻⁴⁷.

Recently, Lewis et al. reported a WO_3 powder with nitrogen molecules (N_2) intercalated into the crystalline lattice by a technique using commercially available ammonium metatungstate ($(\text{NH}_4)_6\text{H}_2\text{W}_{12}\text{O}_{40} \cdot x\text{H}_2\text{O}$) and ammonium paratungstate ($(\text{NH}_4)_{10}\text{H}_2\text{W}_{12}\text{O}_{42} \cdot 4\text{H}_2\text{O}$) as well as ^{15}N -labeled ammonium paratungstate synthesized from tungstic acid and aqueous $^{15}\text{NH}_4\text{OH}$ followed by calcination under O_2 atmosphere to oxidized NH_4^+ ions in the solid state to N_2 gas, being catalyzed by tungsten, and the N_2 enclosed in solid state is trapped in the hollow center of the crystallized WO_3 lattice during phase transition to orthorhombic WO_3 at $\sim 410^\circ\text{C}$.⁴⁸ And thus, the N_2 -intercalated WO_3 provides a red-shift of absorption edge compared with pure WO_3 due to narrowing the band gap by contribution of N 2p in N_2 to the valence band dominated by O 2p of WO_3 . But the reported N_2 -intercalated WO_3 exhibits mainly monoclinic phase with considerable hexagonal phase, which is an undesirable feature because the photoelectrocatalytic activity of hexagonal WO_3 for water oxidation is well-known to be lower than that of the monoclinic phase.⁴⁹ Moreover, nanostructure control is effective to improve the photoelectrocatalytic activity of N_2 -intercalated WO_3 . However, the nano- and micro structure of the N_2 -intercalated WO_3 has not been reported yet.

Herein, we report the synthesis of N_2 -intercalated WO_3 (denoted as $\text{N}_2 \cdot \text{WO}_3$) using hydrazine as a nitrogen source instead of NH_4^+ . The hydrazine-derived $\text{N}_2 \cdot \text{WO}_3$

exhibits the single phase of a monoclinic crystalline as well as a nano-rodlike structure in contrast to the micro-scale block structure of ammonia-derived N_2WO_3 . The hydrazine-derived N_2WO_3 photoanode works efficiently for visible-light driven water oxidation.

5.2 Experimental Section

Materials. The purest grades of tungstic acid (Kanto Chemical Co. Inc.), ammonia aqueous solution, Hydrogen Peroxide (Junsei Chemical Co., Ltd.), and polyethylene glycol (PEG) (Mw=20,000), Tungstgen powder, Hydrozine monohydrate (Wako Pure Chemical Ind., Ltd.), and Marpoloser 60 Mp-50 (Matsumoto Yushi-Seiyaku Co., Ltd.) were purchased and used as received. An indium tin oxide (ITO)-coated glass with 10 Ω /sq of a sheet resistance was purchased from Asahi Glass Co.

Preparations.

Preparation of N_2WO_3 powders and neat WO_3 powder

To yellow suspension of tungstic acid (0.3 g, 1.2 mmol) in water (1.5 mL) was added $N_2H_4 \cdot H_2O$ (146 μ L, 3.0 mmol) drop by drop with vigorous stirring to give white suspension. After continuous stirring for 30 min, solvent was slowly evaporated to yield a hydrazine-derived precursor. An ammonia-derived precursor is synthesized using $NH_3 \cdot H_2O$ (204.0 μ L, 3.0 mmol) in a similar manner to the hydrazine-derived precursor. The peroxo-tungstic acid (PTA) as a precursor for neat WO_3 power was synthesized according to the method by Sayama⁵⁰ 1.46 g (8 mmol) of tungsten powder was carefully dissolved by slow addition of 15 mL aqueous H_2O_2 (30%) in an ice-cold bath and with stirring. The transparent colorless solution was evaporated quickly on a hot stir-plate to decompose excess H_2O_2 and give PTA powder. The PTA powder was re-dissolved in 10 mL hot water and then evaporated to dryness at 70 $^{\circ}C$

to yield a PTA precursor. The hydrazine- and ammonia-derived precursors and the PTA precursor were calcined in an electric furnace at 400 ~ 550 °C with rate of 1 °C min⁻¹ in flowing oxygen atmosphere and then maintained for 1h at this atmosphere to obtain the hydrazine- and ammonia-derived N₂ WO₃ powders and neat WO₃ powder.

Fabrication of N₂ WO₃- or WO₃-coated electrodes

The hydrazine- or ammonia-derived precursor powder (0.2 g), PEG (0.1 g) and Marpolose (20.0 mg) were mixed in water (0.5 mL) with stirring for preparation of a precursor paste. It was coated on an ITO substrate by a squeezing technique and then air-dried for 15 min. The precursor-coated ITO substrate was calcined at 420 °C and 550 °C under oxygen atmosphere to give the hydrazine- or ammonia-N₂ WO₃-coated electrode. The WO₃-coated electrode was prepared by the same method using a PTA precursor.

Measurements

XRD data were recorded using an X-ray diffraction spectrometer (Rigaku, MiniFlex 600) using monochromated Cu K α (λ = 1.54 Å) radiation. SEM images were taken using a scanning electron microscope (JEOL, TSM-6510LV) operated at an accelerating voltage of 10 kV. Raman spectra were recorded using a Raman microspectroscopic apparatus (Horiba-Jobin-Y von, LabRAM HR). UV-visible diffuse reflectance spectra (DRS) were recorded on a spectrophotometer (JASCO, V-670) in a DR mode. Thermogravimetric (TG) and Differential Thermal Analysis (DTA) data were taken using a TG analyzer (Rigaku, TG 8120) from 25 to 800 °C with a heating rate of 5 °C min⁻¹ under air. Photoelectrochemical measurements were conducted using an electrochemical analyzer (HZ-3000, Hokuto Denko Co. Ltd., Tokyo, Japan) and two-compartment photoelectrochemical cell at 25 °C. Three electrode system has been employed using the N₂ WO₃-coated electrode and an Ag/AgCl electrode in one

compartment as the working and reference electrode, respectively and platinum wire in the other compartment as a counter electrode. In order to investigate the effect of Co^{2+} ions on photoelectrocatalytic performance, 0.1 mM $\text{Co}(\text{NO}_3)_2 \cdot 6\text{H}_2\text{O}$ concentration was maintained in electrolyte solution of the working electrode compartment. A 500 W xenon lamp (Optical ModuleX; Ushio Inc., Japan) as a light source with a UV-cut-filter (L39) and liquid filter (0.2 M CuSO_4) for Photoelectrochemical measurements. A monochromic light with 10 nm of bandwidth was given from a 500 W xenon lamp using a monochromator for incident photon-to-current conversion efficiency (IPCE) measurements. All the electrochemical and photoelectrochemical experiments were carried out under argon atmosphere in an aqueous 0.1 M phosphate buffer solution (PBS, pH \approx 6.0).

5.3 Results and Discussion

A SEM technique was used to characterize the morphology of the WO_3 sample and $\text{N}_2 \cdot \text{WO}_3$ samples calcined at 550°C. The SEM image (Figure 1a) shows that the neat WO_3 which prepared from PTA precursor is composed of the particles with 10 – 50 nm in diameter, being well-connected to each other. In a few places, the spherical particles agglomerate to form large particles. The hydrazine-derived $\text{N}_2 \cdot \text{WO}_3$ shows a nanorod structure (Figure 1b), with the rods having 20 - 80nm width, while length of the nanorod range from 500 nm to 1000 nm, which is different from the ammonia-derived $\text{N}_2 \cdot \text{WO}_3$ of the massive blocks in a micro-scale (Figure 1c).

XRD data of the neat WO_3 sample and the hydrazine- and ammonia-derived $\text{N}_2 \cdot \text{WO}_3$ samples prepared at different calcination temperatures are shown in Figure 2 . The neat WO_3 sample calcined at 420°C, shows the monoclinic structure (JSPDF number: 01-083-0950). For the hydrazine-derived $\text{N}_2 \cdot \text{WO}_3$ sample, clear monoclinic phase was observed even at 420 °C, however, for the ammonia-derived $\text{N}_2 \cdot \text{WO}_3$

sample, the peaks at $2\theta = 13.9^\circ$, 28.1° and 36.7° ; which correspond to (100), (200) and (201) of hexagonal WO_3 (JSPDF number: 01-085-2459) were observed with the monoclinic phase at 420°C , being consistent with the XRD data reported earlier⁴⁸. All of WO_3 samples exhibit monoclinic structure after calcination at 550°C . The XRD results suggest that crystallization of the monoclinic phase facilitates for the hydrazine-derived $\text{N}_2 \cdot \text{WO}_3$ sample compared with ammonia-derived $\text{N}_2 \cdot \text{WO}_3$ sample.

The DTA curve of the hydrazine-derived precursor shows a noticeable sharp and intense endothermic peak at 266°C due to the crystallization of WO_3 , which is lower than 315°C of the ammonia-derived precursor (Figure 3). TG analysis confirms that the hydrazine-derived $\text{N}_2 \cdot \text{WO}_3$ sample crystallized earlier than hydrazine-derived $\text{N}_2 \cdot \text{WO}_3$ sample, corresponding to the result of XRD.

Raman spectra depict that clean monoclinic structure are observed from neat WO_3 sample and the hydrazine-derived $\text{N}_2 \cdot \text{WO}_3$ sample. In contrast the ammonia-derived $\text{N}_2 \cdot \text{WO}_3$ sample exhibited the monoclinic phase of peaks at 139.9 cm^{-1} , 276.5 cm^{-1} , 697.1 cm^{-1} and 799.2 cm^{-1} , however, the characteristic signals of the hexagonal phase of peaks which marked by asterisk in Figure 4 were observed simultaneously, agree with the XRD data well (Figure 2). Figure 4 also shows the Raman spectra in a range of $2240 - 2400\text{ cm}^{-1}$ for neat WO_3 sample, the hydrazine- and ammonia-derived $\text{N}_2 \cdot \text{WO}_3$ samples prepared at 420°C and 550°C . Neat WO_3 sample did not show any signal in this region, however, the peaks were observed at $2328 \sim 2330\text{ cm}^{-1}$ for the hydrazine- and ammonia-derived $\text{N}_2 \cdot \text{WO}_3$ samples at both of calcination temperatures, assigned to the $\text{N}\equiv\text{N}$ vibration intercalated into the WO_3 lattice.^{48,51-53} In addition, another broad peak was also observed at 2340 cm^{-1} , suggest that at least two configurations of N_2 were present in both of the hydrazine- and ammonia-derived $\text{N}_2 \cdot \text{WO}_3$ samples, being consistent with the Raman data

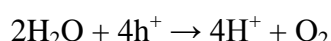
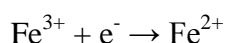
reported previously⁴⁸. To our best knowledge, atomic N doped WO₃ can cause the material to become less crystalline^{46 54} or a new phase (W₂N) will be detected from XRD measurement⁵⁵. In our presentation, hydrazine- and ammonia-derived N₂·WO₃ samples possessing good crystalline degree, although hexagonal phases exist in ammonia-derived N₂·WO₃ sample calcined at 420°C. And no new phase can be detected in hydrazine- and ammonia-derived N₂·WO₃ samples from XRD patterns (Figure 2). Furthermore, Raman signal of N≡N vibration at ~ 2330 cm⁻¹ can not be observed from N-doped materials, whereas, N₂ intercalated materials show this characteristic vibrational signal into the WO₃ lattice.^{48,51-53}. These can be used as the most important evidence for the material have already trapped N₂ species into WO₃ lattice whether or not.

DRS data of neat WO₃ sample, the hydrazine - and ammonia-derived N₂·WO₃ samples prepared at 420°C and 550°C are shown in Figure. 5. For neat WO₃ sample, the wavelength of onset of light absorption was around at 470 nm, which is equivalent to 2.7 eV of band gap energy. For comparison with neat WO₃, the UV-vis reflectance of hydrazine- and ammonia-derived N₂·WO₃ samples prepared at 420°C, predominant absorption are similar to that of neat WO₃ sample. But the absorption shoulders were observed around at 480 nm caused noticeable red-shift of fundamental absorption edge due to N₂ molecular was intercalated into the lattice of WO₃ and led to obvious changes in colours, from the pale green of pure monoclinic neat WO₃ sample to the orange and dark yellow of hydrazine-derived N₂·WO₃ and ammonia-derived N₂·WO₃ samples, respectively. Although the absorption shoulders became smaller compared with 420°C due to the color of the hydrazine- and ammonia-derived N₂·WO₃ samples changed from yellow and pale orange to yellow green and pale green after being annealing at 550°C, the absorption red-shift were still observed as

shown in Figure.5. According to the results of DRS, it suggests that the crystal and electronic structure of WO₃ will be altered after N₂ intercalation. After N₂ intercalating, it will form a new intermediate energy level (N 2p) above the valence band of WO₃ to play a key role in the photoresponse of WO₃. And thus, N₂ ·WO₃ materials are looking forward to showing high photocatalytic activity and PEC water oxidation performance under visible light irradiation.

Energy dispersive X-ray spectroscopic (EDS) data clearly showed the presence of nitrogen for the hydrazine- and ammonia-derived N₂ ·WO₃ samples in comparison with WO₃ sample (Figure 6). The molar ratio of W : N for the hydrazine-derived N₂ ·WO₃ sample calcined at 420 °C was 1 : 0.095, which is higher than that (1 : 0.05) for the ammonia-derived N₂ ·WO₃ sample calcined at the same temperature (Table 1) . And also, the EDS data indicates higher contents of nitrogen for the hydrazine-derived N₂ ·WO₃ sample compared to the ammonia-derived N₂ ·WO₃ sample even half amount of hydrazine was used, is summarized in Table S1. Though these ratios decreased with increasing the calcination temperature for both the N₂ ·WO₃ samples, the ratio (1 : 0.01) for the hydrazine-derived N₂ ·WO₃ sample is still higher than that (1 : 0.006) of ammonia-derived N₂ ·WO₃ sample under 550 °C calcination conditions.

Recently, O₂ evolution has been reported from aqueous Fe₂(SO₄)₃ solution according to the half reaction following.¹⁶



The total reaction is:

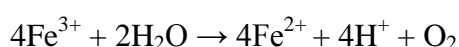


Figure 7 exhibits the photocatalytic water oxidation in the Fe₂(SO₄)₃ aqueous

solution with pH=2.3, upon irradiation visible light ($\lambda > 390$ nm) using neat WO_3 , hydrazine-derived $\text{N}_2 \cdot \text{WO}_3$ and ammonia-derived $\text{N}_2 \cdot \text{WO}_3$ catalysts prepared at 420 °C and 550°C. It is noted that the hydrazine-derived $\text{N}_2 \cdot \text{WO}_3$ shows highest activities at both 420 °C and 550°C compare to neat WO_3 and ammonia-derived $\text{N}_2 \cdot \text{WO}_3$. With the temperature increased, the photocatalytic activity also increased due to the crystalline increased. However, the ammonia-derived $\text{N}_2 \cdot \text{WO}_3$ shows low photocatalytic activity for water oxidation due to its morphology (blocks, Fig. 1c) can't transport electron-hole well compare to neat WO_3 (nanoparticles, Fig. 1a), and hydrazine-derived $\text{N}_2 \cdot \text{WO}_3$ (nanorods, Fig. 1b). The time course of O_2 evolution over different WO_3 photocatalysts are shown in Figure 8.

The PEC properties of the ITO/ WO_3 electrodes prepared at 420°C were studied in a 0.1 M phosphate solution with pH adjusted to 6.0. Cyclic voltammograms (CVs) of the neat WO_3 , ammonium- and hydrazine-derived $\text{N}_2 \cdot \text{WO}_3$ electrodes are shown in Figure. 9, where the redox response of $\text{H}_x\text{WO}_3 / \text{WO}_3$ were observed below 0.2 V vs. Ag/AgCl, however, no anodic currents were observed under the dark condition in a potential range of 0.2 ~ 1.0 V vs. Ag/AgCl for all of electrodes due to n-type Schottky barrier at the interfacial heterojunction between the electrodes surface and the electrolyte solution. Upon irradiation of visible light, a photoanodic current of 0.02 mA cm^{-2} was hardly observed for neat ITO/ WO_3 electrode. However, a significant higher photoanodic current due to water oxidation over 0.2 V vs. Ag/AgCl was observed and it reached to 1.24 mA cm^{-2} at 1.0 V vs. Ag/AgCl for ITO/hydrazine-derived $\text{N}_2 \cdot \text{WO}_3$ electrode, which is about 4 times higher than that of ITO/ammonium-derived $\text{N}_2 \cdot \text{WO}_3$ electrode (0.3 mA cm^{-2} at 1.0 V vs. Ag/AgCl).

In Figure 11, the action spectra of IPCE were recorded under the bias potential of 0.5 V versus Ag/AgCl using different ITO/ WO_3 photoanodes. On the IPCE spectra of

samples calcined at 420°C (Figure 11, left), the IPCE of neat WO₃ at 400 nm was 0.4% with the onset wavelength of 470 nm, corresponds the indirect band gap energy of 2.63 eV. In the case of hydrazine- and ammonia-derived N₂·WO₃ samples, the IPCE values at 400 nm increased to 5.18% and 4.90%, the onset wavelength of both N₂·WO₃ samples extended to 520 nm and 510 nm, which consistent with the band gap of hydrazine- and ammonia-derived N₂·WO₃ samples of 2.38 eV and 2.41 eV, respectively, indicating that the photoanodic current is based on a band gap photoexcitation of N 2p-W 5d. Furthermore, IPCE for different electrodes calcined at 550°C are shown in Figure 11, where the photoreponse position decreased to 490 nm for both of hydrazine- and ammonia-derived N₂·WO₃ samples due to the content of N₂ became lower compare to that of samples prepared at 420°C. However, the maximum IPCE at 400 nm of the hydrazine-derived N₂·WO₃ (58%) is about five- and six times higher than that of ammonia-derived N₂·WO₃ (14%) and neat WO₃ (8%), respectively. The high IPCE value of the hydrazine-derived N₂·WO₃ is attributed to its high crystallinity and high content of N₂ molecule intercalation can utilize the visible light efficiently to increase IPCE compare to the others two samples. As comparison of IPCE value for WO₃-based photoanodes reported previously by Santato²⁹, this present IPCE value at 400 nm of hydrazine-derived N₂·WO₃ is lower than that of the nanoparticle WO₃ (75% measured at 1V vs. RHE in 1 M HClO₄),²⁹ but higher and comparable to the recently values obtained for WO₃ nanostructures^{21-23,33,34,56-58}, such as WO₃ nanoplatelet (30% measured at 1.2 V vs. SCE in 1 M HClO₄)⁵⁷, WO₃ nanorod (18% measured at 1.23 V vs. RHE in 0.5 M Na₂SO₄)²¹, WO₃ nanorod (35% measured at 0.8

V vs. Ag/AgCl in 0.5 M Na₂SO₄)²², WO₃ nanoflakes (35% measured at 1.0 V vs. Ag/AgCl in 0.5 M Na₂SO₄)²³, WO₃ nanowire (8% measured at 0.5 V vs. Ag/AgCl in 0.1 M Na₂SO₄) and WO₃ nanoflakes (55% measured at 1.0 V vs. Ag/AgCl in 0.1 M Na₂SO₄)³³, WO₃ nanoflake (38% measured at 1.2 V vs. Ag/AgCl in 0.1 M Na₂SO₄)³⁴, WO₃ nanoparticle (15% measured at 1.2 V vs. NHE in 0.5 M H₂SO₄)⁵⁶ and WO₃ nanorode (30% measured at 0.5 V vs. NHE in 0.5 M Na₂SO₄)⁵⁸.

The photoelectrocatalysis experiments over different electrodes calcined at 550°C (Figure 12) were preliminary performed under 100 mW / cm⁻² illumination at 0.5 V in a 0.1 M phosphate buffer with pH adjusted to 6.0 for 1h, upon visible light irradiation ($\lambda > 390$ nm). The photocurrent-time profile of the hydrazine-derived N₂·WO₃ (Fig. 12c) exhibited a quite higher initial photocurrent (0.78 mA cm⁻² at 2 minute) comparing to neat WO₃ (0.30 mA/cm⁻², Fig. 12a) and ammonia-derived N₂·WO₃ (0.55 mA cm⁻², Fig. 12c), which is corresponding to cyclic voltammetry (CV) data (Figure 10). But the photocurrents were not stable and began to decay over time, the photocurrent of hydrazine-derived N₂·WO₃ decreased to 0.28 mA cm⁻² after 1h of photoelectrocatalysis (about 64% decrease), the decay of photocurrents for neat WO₃ and ammonia-derived N₂·WO₃ were 77% and 62%, respectively after 1h of irradiation caused by the formation of tungsten peroxo species on the WO₃ surface^{29,59}. The charge amount passed during 1h of photoelectrocatalysis for hydrazine-derived N₂·WO₃ (1.05 C) is 3.1 and 1.2 times higher than those of neat WO₃ (0.34 C) and ammonia-derived N₂·WO₃ (0.9 C), respectively (Table 2). The amount of O₂ evolution during photoelectrocatalysis for hydrazine-derived N₂·WO₃ (2.16 μ mol) is much

higher than neat WO_3 (0.52 μmol) and ammonia-derived $\text{N}_2 \cdot \text{WO}_3$ (1.69 μmol). Also, Faradaic efficiency of O_2 evolution for hydrazine-derived $\text{N}_2 \cdot \text{WO}_3$ (80%) is higher than neat WO_3 film (56%) and ammonia-derived $\text{N}_2 \cdot \text{WO}_3$ (72%). The high PEC water oxidation performance for hydrazine-derived $\text{N}_2 \cdot \text{WO}_3$ is attributed to its high content of N element in hydrazine-derived $\text{N}_2 \cdot \text{WO}_3$ lattice and nanorod structured morphology and high crystallinity.

The performance of PEC water oxidation shows further improvement by adding 0.1 mM Co^{2+} ions in the electrolyte solution (Fig. 12d). In the presence of 0.1 mM Co^{2+} ions in phosphate buffer solution, hydrazine-derived $\text{N}_2 \cdot \text{WO}_3$ shows 0.9 mA cm^{-2} of initial photocurrent at 2 minute and give 0.68 mA cm^{-2} of photocurrent after 1h of photoelectrocatalysis, which is about 2.4 times better than the absence of Co^{2+} ions. The charge amount passed of 2.62 C (5.47 μmol of O_2 evolution, F.E. _{O_2} 81%, Table 2) is 2.5 times better than the charge amount of 1.05 C without Co^{2+} ions. The enhancement of PEC water oxidation after adding Co^{2+} ions indicate that the formation of peroxo species would be suppressed due to acceleration of the water oxidation reaction on the WO_3 surface by Co^{2+} ions in the electrolyte solution.

5.4 Reference

- (1) Chen, X.; Shen, S.; Guo, L.; Mao, S. S. *Chem. Rev.* **2010**, *110*, 6503.
- (2) Kamat, P. V.; Tvrđy, K.; Baker, D. R.; Radich, J. G. *Chem. Rev.* **2010**, *110*, 6664.
- (3) Kudo, A.; Miseki, Y. *Chem. Soc. Rev.* **2009**, *38*, 253.

- (4) Chandra, D.; Saito, K.; Yui, T.; Yagi, M. *Angew. Chem. Int. Ed.* **2013**, *52*, 12606.
- (5) Satsangi, V.; Kumari, S.; Singh, A.; Shrivastav, R.; Dass, S. *Int. J. Hydrogen Energy* **2008**, *33*, 312.
- (6) Rahman, G.; Joo, O.-S. *Int. J. Hydrogen Energy* **2012**, *37*, 13989.
- (7) Li, Y.; Takata, T.; Cha, D.; Takanabe, K.; Minegishi, T.; Kubota, J.; Domen, K. *Adv. Mater.* **2013**, *25*, 125.
- (8) Maeda, K.; Higashi, M.; Lu, D.; Abe, R.; Domen, K. *J. Am. Chem. Soc.* **2010**, *132*, 5858.
- (9) Maeda, K.; Domen, K. *Angew. Chem. Int. Ed.* **2012**, *51*, 9865.
- (10) Abe, T.; Nagai, K.; Kabutomori, S.; Kaneko, M.; Tajiri, A.; Norimatsu, T. *Angew. Chem. Int. Ed.* **2006**, *45*, 2778.
- (11) Abe, R.; Takata, T.; Sugihara, H.; Domen, K. *Chem. Commun.* **2005**, 3829.
- (12) Hisatomi, T.; Dotan, H.; Stefik, M.; Sivula, K.; Rothschild, A.; Grätzel, M.; Mathews, N. *Adv. Mater.* **2012**, *24*, 2699.
- (13) Chatchai, P.; Murakami, Y.; Kishioka, S.-y.; Nosaka, A. Y.; Nosaka, Y. *Electrochim. Acta* **2009**, *54*, 1147.
- (14) Kim, H. G.; Borse, P. H.; Jang, J. S.; Ahn, C. W.; Jeong, E. D.; Lee, J. S. *Adv. Mater.* **2011**, *23*, 2088.
- (15) Kominami, H.; Yabutani, K.-i.; Yamamoto, T.; Kera, Y.; Ohtani, B. *J. Mater. Chem.* **2001**, *11*, 3222.
- (16) Miseki, Y.; Kusama, H.; Sugihara, H.; Sayama, K. *J. Phys. Chem. Lett.* **2010**,

1, 1196.

(17)Ma, S. S. K.; Maeda, K.; Abe, R.; Domen, K. *Energy Environ. Sci.* **2012**, *5*, 8390.

(18)Martin, D. J.; Reardon, P. J. T.; Moniz, S. J. A.; Tang, J. *J. Am. Chem. Soc.* **2014**, *136*, 12568.

(19)Yagi, M.; Maruyama, S.; Sone, K.; Nagai, K.; Norimatsu, T. *J. Solid State Chem.* **2008**, *181*, 175.

(20)Li, D.; Chandra, D.; Saito, K.; Yui, T.; Yagi, M. *Nanoscale Res. Lett.* **2014**, *9*, 542.

(21)Pihosh, Y.; Turkevych, I.; Mawatari, K.; Asai, T.; Hisatomi, T.; Uemura, J.; Tosa, M.; Shimamura, K.; Kubota, J.; Domen, K.; Kitamori, T. *Small* **2014**, *10*, 3692.

(22)Kalanur, S. S.; Hwang, Y. J.; Chae, S. Y.; Joo, O. S. *J. Mater. Chem.* **2013**, *1*, 3479.

(23)Wang, G.; Ling, Y.; Wang, H.; Yang, X.; Wang, C.; Zhang, J. Z.; Li, Y. *Energy Environ. Sci.* **2012**, *5*, 6180.

(24)Seabold, J. A.; Choi, K.-S. *Chem. Mater.* **2011**, *23*, 1105.

(25)Hill, J. C.; Choi, K.-S. *J. Phys. Chem. C* **2012**, *116*, 7612.

(26)Kim, J.; Shin, K.; Cho, S.; Lee, T.-W.; Park, J. *Energy Environ Sci* **2011**, *4*, 1465.

(27)Yang, B.; Zhang, Y.; Drabarek, E.; Barnes, P.; Luca, V. *Chem. Mater.* **2007**, *19*, 5664.

(28)Miseki, Y.; Fujiyoshi, S.; Gunji, T.; Sayama, K. *Catal. Sci. Tech.* **2013**, *3*,

1750.

(29) Santato, C.; Ulmann, M.; Augustynski, J. *J. Phys. Chem. B* **2001**, *105*, 936.

(30) Li, W.; Li, J.; Wang, X.; Ma, J.; Chen, Q. *Int. J. Hydrogen Energy* **2010**, *35*,

13137.

(31) Sivakumar, R.; Moses Ezhil Raj, A.; Subramanian, B.; Jayachandran, M.;

Trivedi, D. C.; Sanjeeviraja, C. *Mater. Res. Bull.* **2004**, *39*, 1479.

(32) Santato, C.; Odziemkowski, M.; Ulmann, M.; Augustynski, J. *J. Am. Chem.*

Soc. **2001**, *123*, 10639.

(33) Su, J.; Feng, X.; Sloppy, J. D.; Guo, L.; Grimes, C. A. *Nano Lett.* **2010**, *11*,

203.

(34) Amano, F.; Li, D.; Ohtani, B. *Chem. Commun.* **2010**, *46*, 2769.

(35) Liu, X.; Wang, F.; Wang, Q. *Phys. Chem. Chem. Phys.* **2012**, *14*, 7894.

(36) Bi, Y.; Li, D.; Nie, H. *Mater. Chem. Phys.* **2010**, *123*, 225.

(37) Hameed, A.; Gondal, M. A.; Yamani, Z. H. *Catal. Commun.* **2004**, *5*, 715.

(38) Radecka, M.; Sobas, P.; Wierzbicka, M.; Rekas, M. *Phys. B* **2005**, *364*, 85.

(39) Ng, K.; Minggu, L.; Kassim, M. *Int. J. Hydrogen Energy* **2013**, *38*, 9585.

(40) Liu, H.; Peng, T.; Ke, D.; Peng, Z.; Yan, C. *Mater. Chem. Phys.* **2007**, *104*,

377.

(41) Yang, B.; Luca, V. *Chem. Commun.* **2008**, 4454.

(42) Enesca, A.; Duta, A.; Schoonman, J. *Phys. Status Solidi A* **2008**, *205*, 2038.

(43) Karuppasamy, K. M.; Subrahmanyam, A. *J. Phys. D: Appl. Phys.* **2008**, *41*,

035302.

- (44) Xueting, C.; Shibin, S.; Yun, Z.; Lihua, D.; Yansheng, Y. *Nanotechnology* **2011**, 22, 265603.
- (45) Sun, Y.; Murphy, C. J.; Reyes-Gil, K. R.; Reyes-Garcia, E. A.; Thornton, J. M.; Morris, N. A.; Raftery, D. *Int. J. Hydrogen Energy* **2009**, 34, 8476.
- (46) Cole, B.; Marsen, B.; Miller, E.; Yan, Y.; To, B.; Jones, K.; Al-Jassim, M. J. *Phys. Chem. C* **2008**, 112, 5213.
- (47) Li, W.; Li, J.; Wang, X.; Chen, Q. *Appl. Surf. Sci.* **2012**, 263, 157.
- (48) Mi, Q.; Ping, Y.; Li, Y.; Cao, B.; Brunschwig, B. S.; Khalifah, P. G.; Galli, G. A.; Gray, H. B.; Lewis, N. S. *J. Am. Chem. Soc.* **2012**, 134, 18318.
- (49) Szilágyi, I. M.; Fűrész, B.; Rosseler, O.; Szegedi, Á.; Németh, P.; Király, P.; Tárnágyi, G.; Vajna, B.; Varga-Josepovits, K.; László, K.; Tóth, A. L.; Baranyai, P.; Leskelä, M. *J. Catal.* **2012**, 294, 119.
- (50) Sayama, K.; Hayashi, H.; Arai, T.; Yanagida, M.; Gunji, T.; Sugihara, H. *Appl. Catal. B* **2010**, 94, 150.
- (51) Tessier, F.; Le Gendre, L.; Cheviré, F.; Marchand, R.; Navrotsky, A. *Chem. Mater.* **2005**, 17, 3570.
- (52) Ebbinghaus, S. G.; Abicht, H.-P.; Dronskowski, R.; Müller, T.; Reller, A.; Weidenkaff, A. *Prog. Solid State Chem.* **2009**, 37, 173.
- (53) Rachel, A.; Ebbinghaus, S. G.; Güngerich, M.; Klar, P. J.; Hanss, J.; Weidenkaff, A.; Reller, A. *Thermochim. Acta* **2005**, 438, 134.
- (54) Vemuri, R. S.; Noor-A-Alam, M.; Gullapalli, S. K.; Engelhard, M. H.; Ramana, C. V. *Thin Solid Films* **2011**, 520, 1446.

- (55)Liu, Y.; Li, Y.; Li, W.; Han, S.; Liu, C. *Appl. Surf. Sci.* **2012**, 258, 5038.
- (56)Hong, S. J.; Jun, H.; Borse, P. H.; Lee, J. S. *Int. J. Hydrogen Energy* **2009**, 34, 3234.
- (57)Yagi, M.; Maruyama, S.; Sone, K.; Nagai, K.; Norimatsu, T. *J Solid State Chem* **2008**, 181, 175.
- (58)Su, J.; Guo, L.; Bao, N.; Grimes, C. A. *Nano Lett.* **2011**, 11, 1928.
- (59)Seabold, J.; Choi, K.-S. *Chem Mater* **2011**, 23, 1105.

Table 5-1 EDS data of WO₃ samples prepared from different precursors followed by calcination at 420 °C and 550 °C.

Sample name	$n_{\text{H}_2\text{WO}_4} : n_{\text{N}_2\text{H}_4} (n_{\text{NH}_3})$	Calcination	Molar ration of W: N
		temperature / °C	
Neat WO ₃	1 : 0	550	-
N ₂ H ₄ -derived N ₂ ·WO ₃	1 : 1.25	420	1 : 0.092
N ₂ H ₄ -derived N ₂ ·WO ₃	1 : 2.5	420	1 : 0.095
NH ₃ -derived N ₂ ·WO ₃	1 : 2.5	420	1 : 0.05
N ₂ H ₄ -derived N ₂ ·WO ₃	1 : 1.25	550	1 : 0.008
N ₂ H ₄ -derived N ₂ ·WO ₃	1 : 2.5	550	1 : 0.01
NH ₃ -derived N ₂ ·WO ₃	1 : 2.5	550	1 : 0.006

Table 5-2 Summary of photoelectrocatalytic water oxidation using different ITO/WO₃ photoanodes calcined at different temperatures.

sample	[Co ²⁺] / mM	Charge / C	n_{O_2} / μmol	F.E. _{O₂} ^a (%)	n_{H_2} ^b / μmol	F.E. _{H₂} ^c (%)
WO ₃ (PTA)	0	0.34	0.52	56	1.46	83
N ₂ ·WO ₃ (NH ₃)	0	0.90	1.69	72	4.59	98
N ₂ ·WO ₃ (N ₂ H ₄)	0	1.05	2.16	79	5.02	91
N ₂ ·WO ₃ (N ₂ H ₄)	0.1	2.62	5.47	81	12.70	93

^aFaradic efficiency of O₂ evolution.

^b n_{H_2} is the amount of H₂ evolved in the Pt counter electrode compartment.

^cFaradic efficiency of H₂ evolution.

^d N.D. (Not Detected)

^e Calc.Temp. (Calcination temperature)

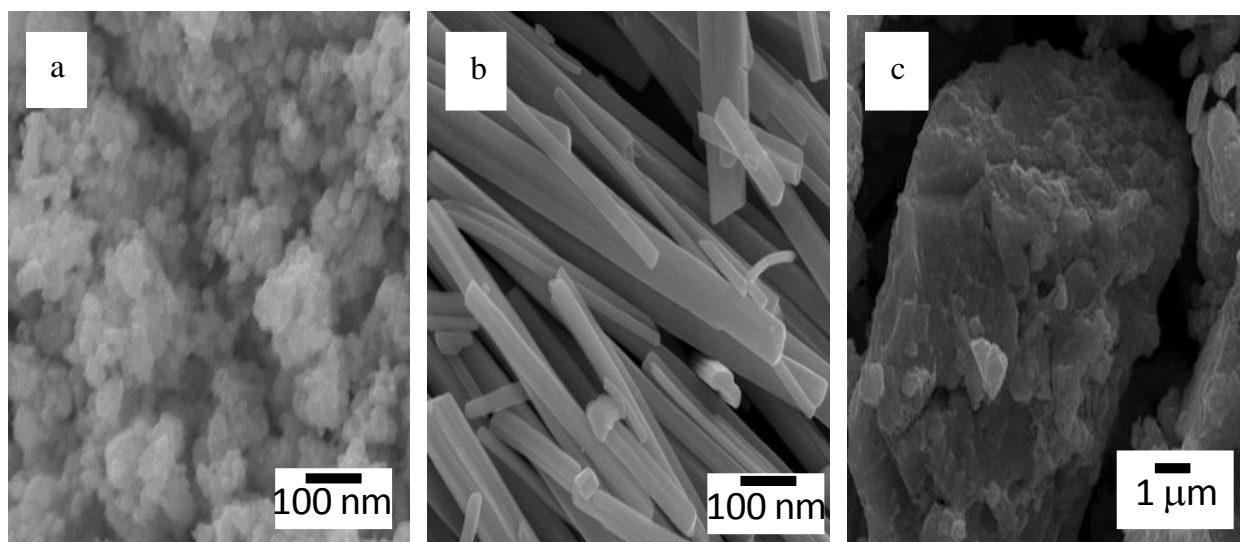


Figure 5-1 Scanning electron microscopic (SEM) images of (a) neat WO_3 , (b) N_2H_4 -derived $\text{N}_2 \cdot \text{WO}_3$, and (c) NH_3 -derived $\text{N}_2 \cdot \text{WO}_3$ samples annealed at 550°C .

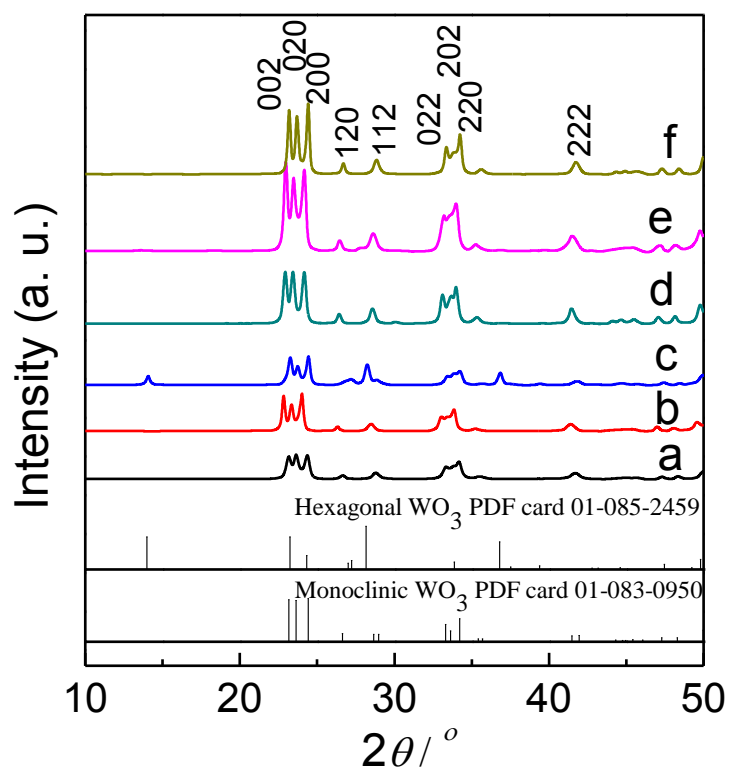


Figure 5-2 XRD patterns of (a and d) neat WO_3 , N_2H_4 -derived $\text{N}_2 \cdot \text{WO}_3$ (b and e) and (c and f) NH_3 -derived $\text{N}_2 \cdot \text{WO}_3$ samples calcined at (a, b and c) 420°C and (d, e and f) 550°C .

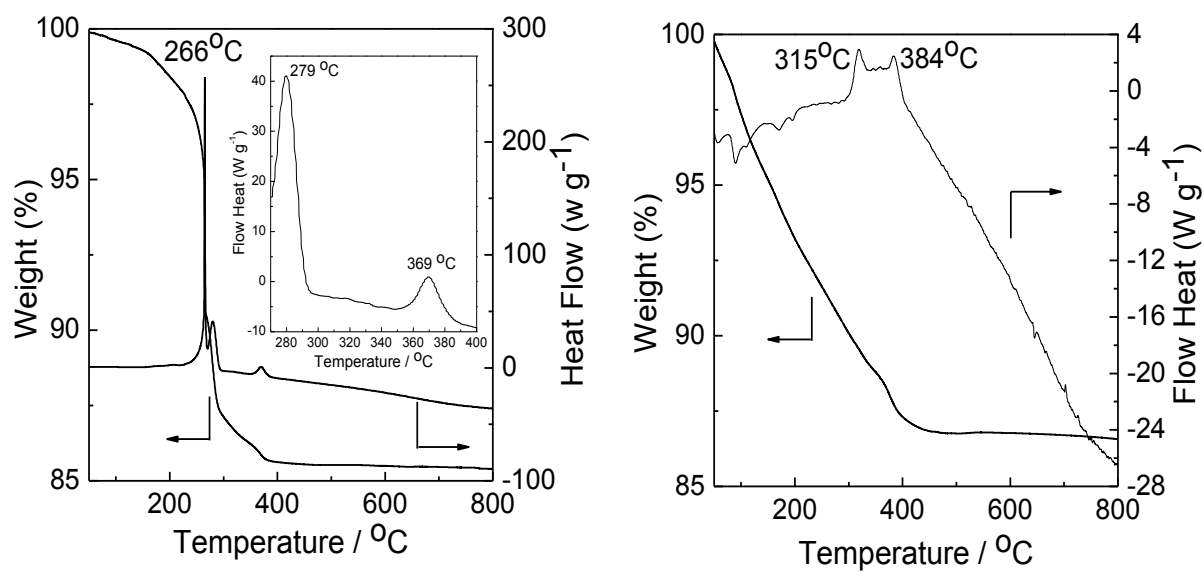


Figure 5-3 Thermogravimetric (TG) curves of (left) N₂H₄-derived precursor and (right) NH₃-derived precursor.

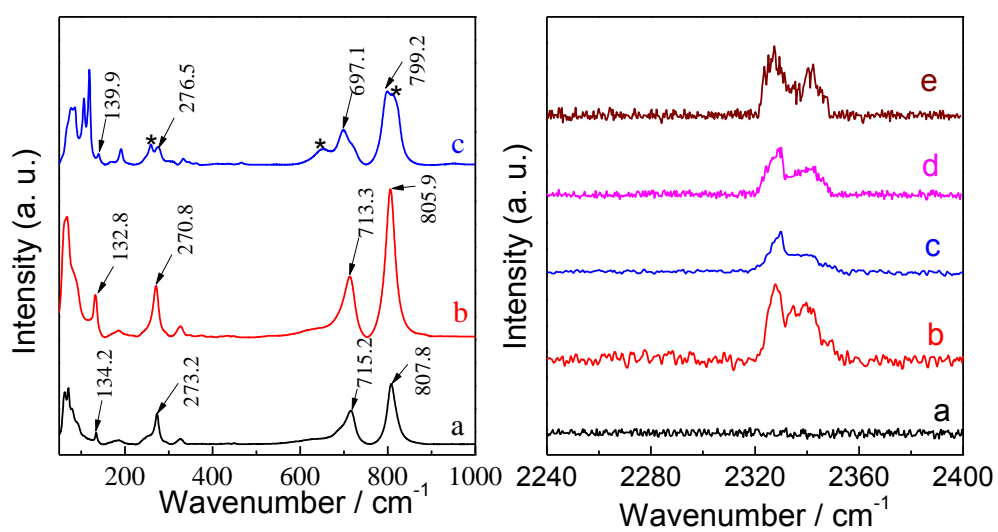


Figure 5-4 Raman spectra of (a) neat WO_3 , (b and d) N_2H_4 -derived $\text{N}_2 \cdot \text{WO}_3$ and (c and e) NH_3 -derived $\text{N}_2 \cdot \text{WO}_3$ samples at (left) low wavenumber and (right) high Wavenumber after being calcined at (a, b and c) 420°C and (d and e) 550°C .

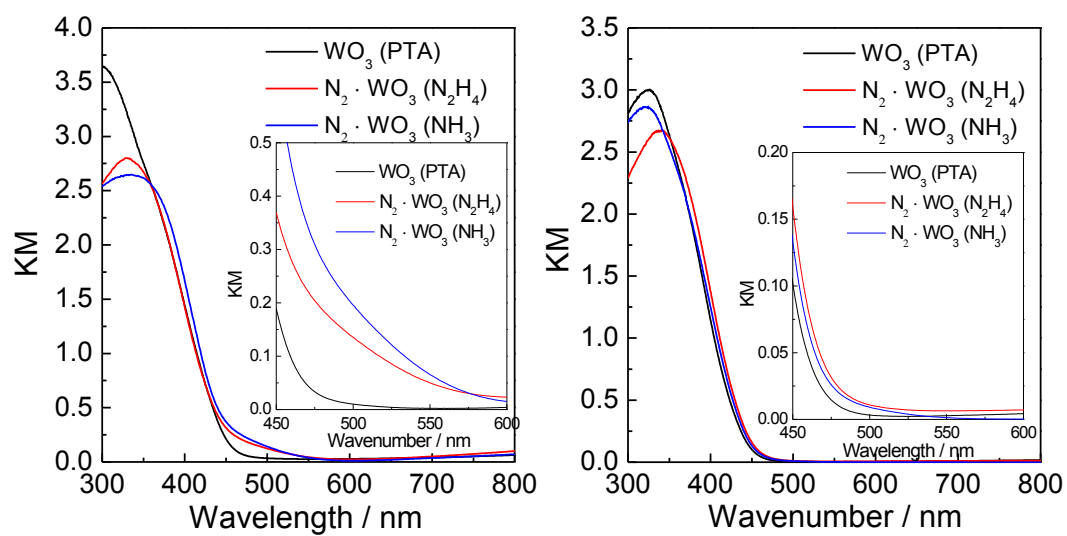


Figure 5-5 UV-vis diffuse reflectance spectra (DRS) of WO_3 samples calcined at (left) 420°C and (right) 550°C.

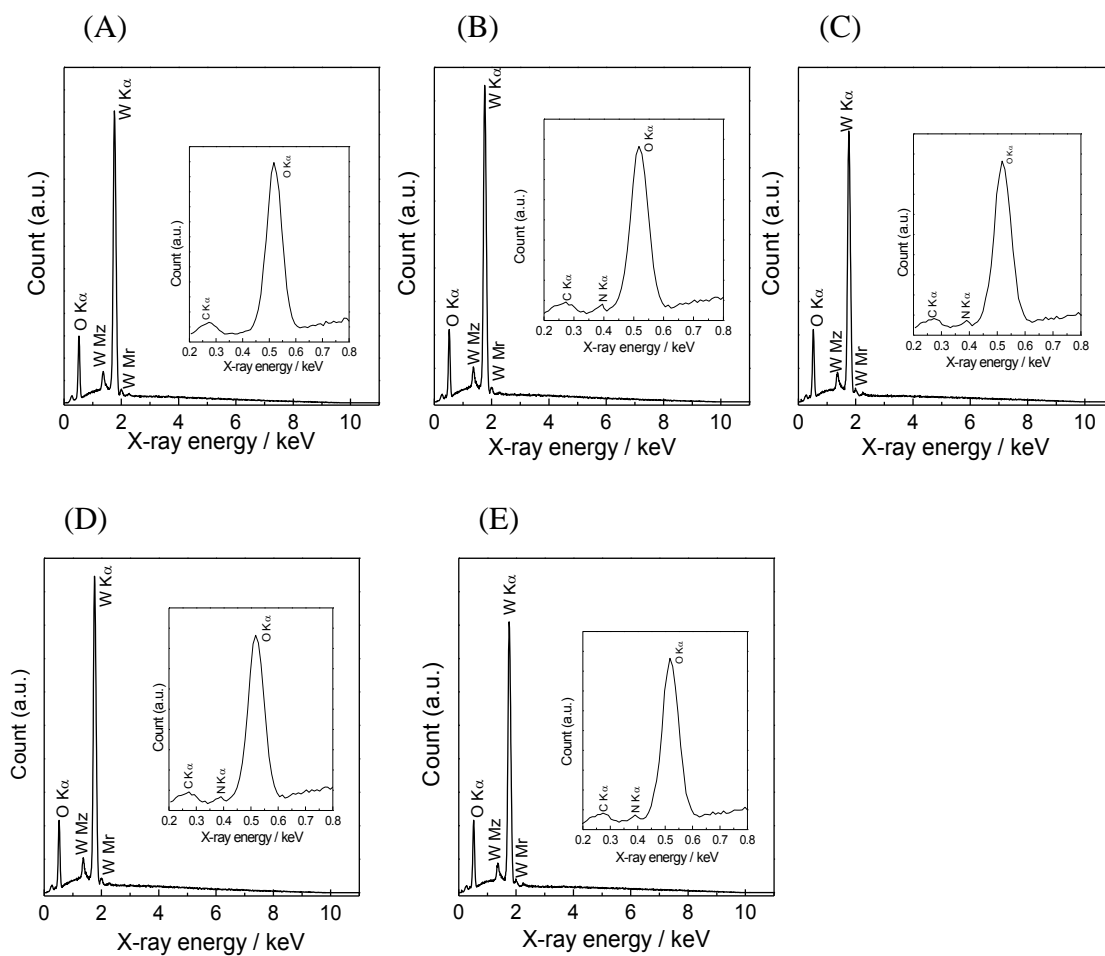


Figure 5-6 Energy dispersive X-ray spectroscopic (EDS) data of (A) neat WO_3 , (B and D) N_2H_4 -derived $\text{N}_2 \cdot \text{WO}_3$ and (C and E) NH_3 -derived $\text{N}_2 \cdot \text{WO}_3$ samples calcined at (A, B and C) 420°C and (D and E) 550°C .

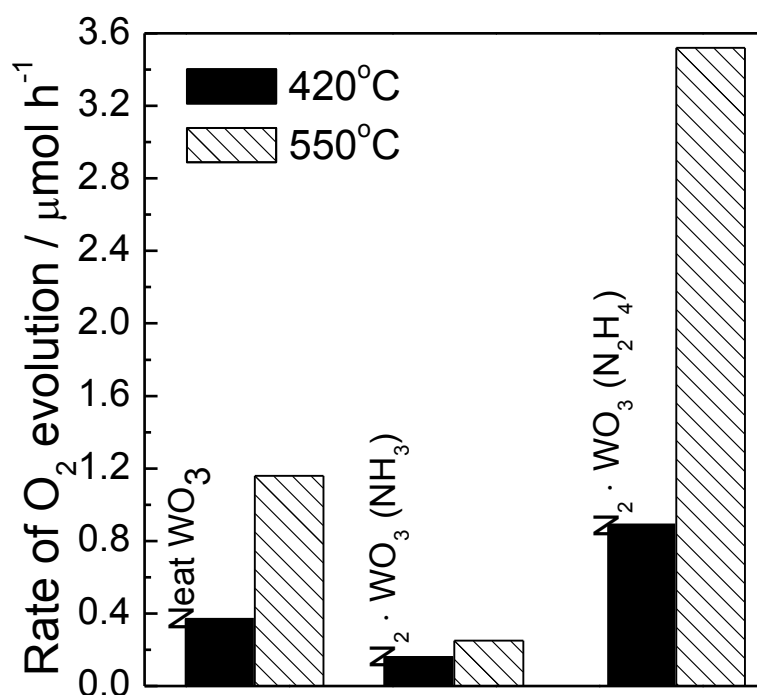


Figure 5-7 Comparison of the rate of O₂ over different WO₃ catalysts calcined at (left column) 420°C and (right column) 550°C. *Reaction conditions:* catalyst, 40 mg; aqueous Fe₂(SO₄)₃ solution, 40 mL (2.1 mM); Light source: 300 W Xe lamp with a cut filter (L39); Light intensity: 100 mW cm⁻²; Reaction vessel: Quartz top-irradiation type.

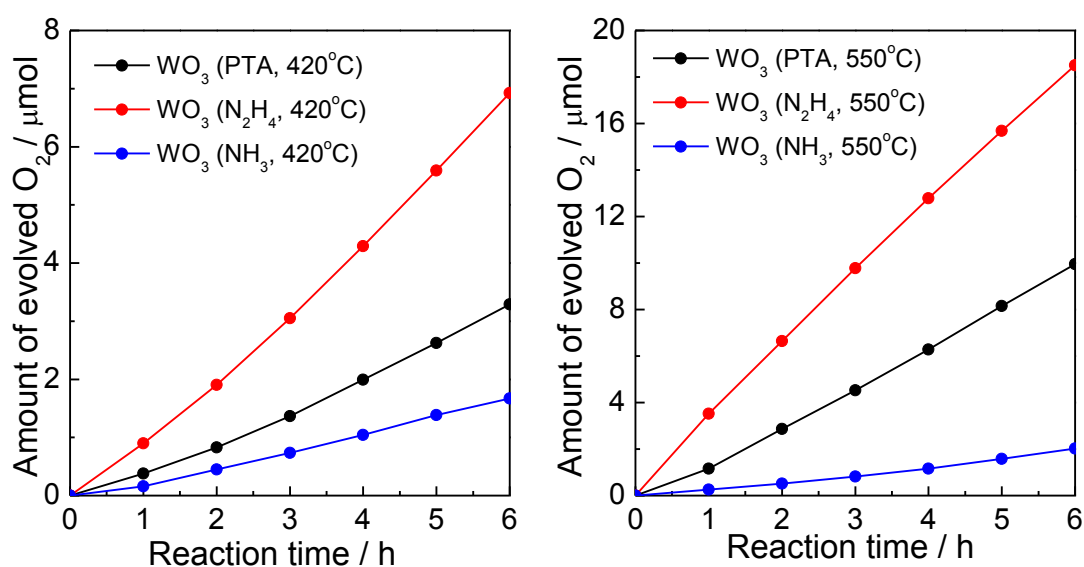


Figure 5-8 Photocatalytic O₂ evolution over (black) neat WO₃, (red) N₂H₄-derived N₂ WO₃ and (blue) NH₃-derived N₂ WO₃ samples calcined at (left) 420°C and (right) 550°C. *Reaction conditions:* catalyst, 40 mg; aqueous Fe₂(SO₄)₃ solution, 40 mL (2.1 mM); Light source: 300 W Xe lamp with a cut filter (L39); Light intensity: 100 mW cm⁻²; Reaction vessel: Quartz top-irradiation type.

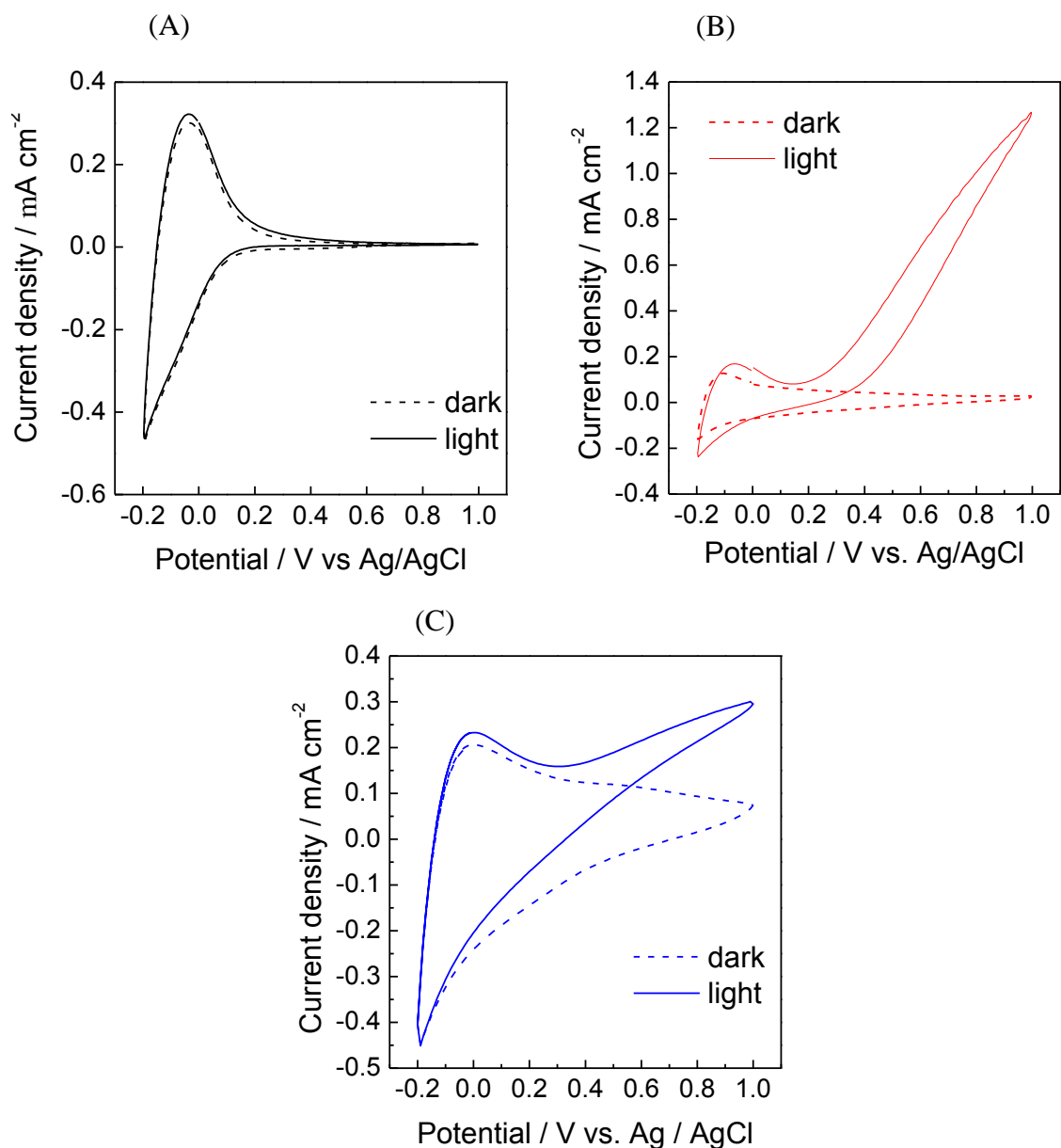


Figure 5-9 Cyclic voltammograms (CVs) for the samples calcined at 420 °C of the (A) ITO/neat WO_3 , (B) ITO/ N_2H_4 -derived $\text{N}_2 \cdot \text{WO}_3$ and (C) ITO/ NH_3 -derived $\text{N}_2 \cdot \text{WO}_3$ electrodes in a 0.1 M phosphate buffer solution of pH = 6.0. The dashed and solid lines represents CV measured in the dark and on irradiation of visible light ($\lambda > 390$ nm, 100 mW cm^{-2}), respectively.

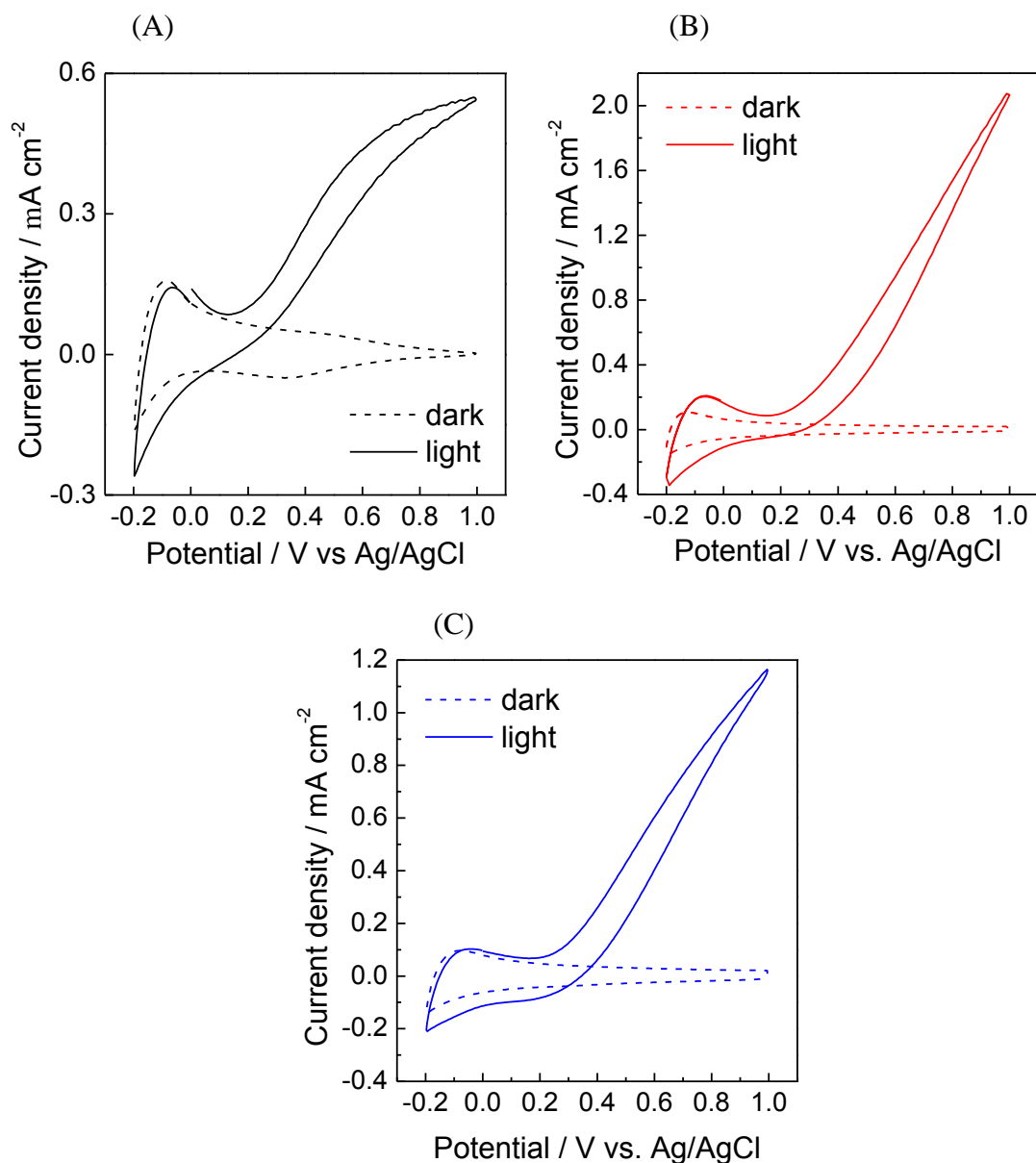


Figure 5-10 Cyclic voltammograms (CVs) for the samples calcined at 550 °C of the (A) ITO/neat WO_3 , (B) ITO/ N_2H_4 -derived N_2WO_3 and (C) ITO/ NH_3 -derived N_2WO_3 electrodes in a 0.1 M phosphate buffer solution of pH = 6.0. The dashed and solid lines represents CV measured in the dark and on irradiation of visible light ($\lambda > 390 \text{ nm}$, 100 mW cm^{-2}), respectively.

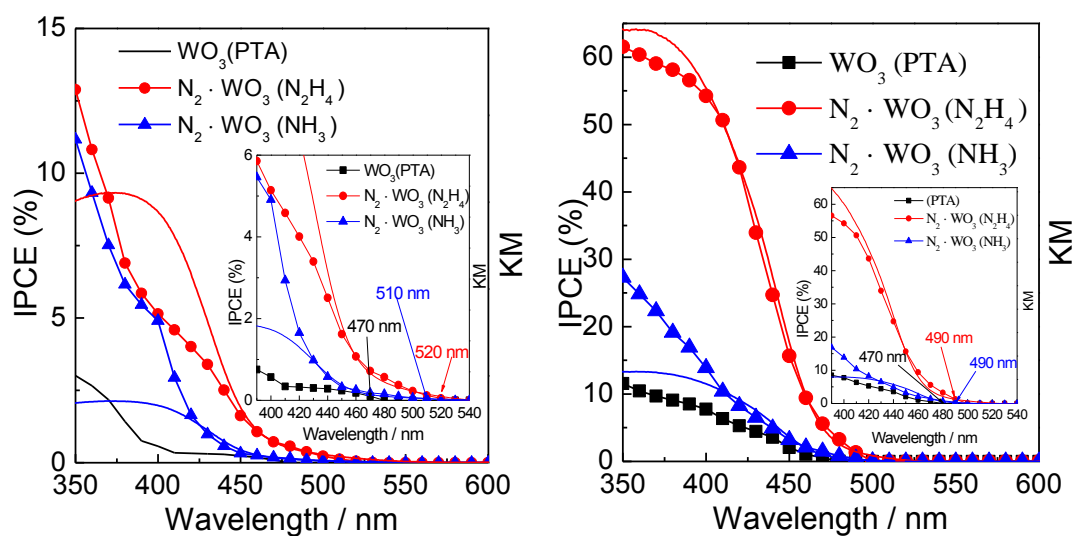


Figure 5-11 Action spectra of IPCE of (black) ITO/neat WO_3 , (red) ITO/hydrazine-derived $\text{N}_2 \cdot \text{WO}_3$, and (blue) ITO/ammonia-derived $\text{N}_2 \cdot \text{WO}_3$ electrodes calcined at (left) 420°C and (right) 550°C. IPCE was measured in a phosphate buffer (0.1 M, pH = 6.0) at 0.5 V vs. Ag/AgCl.

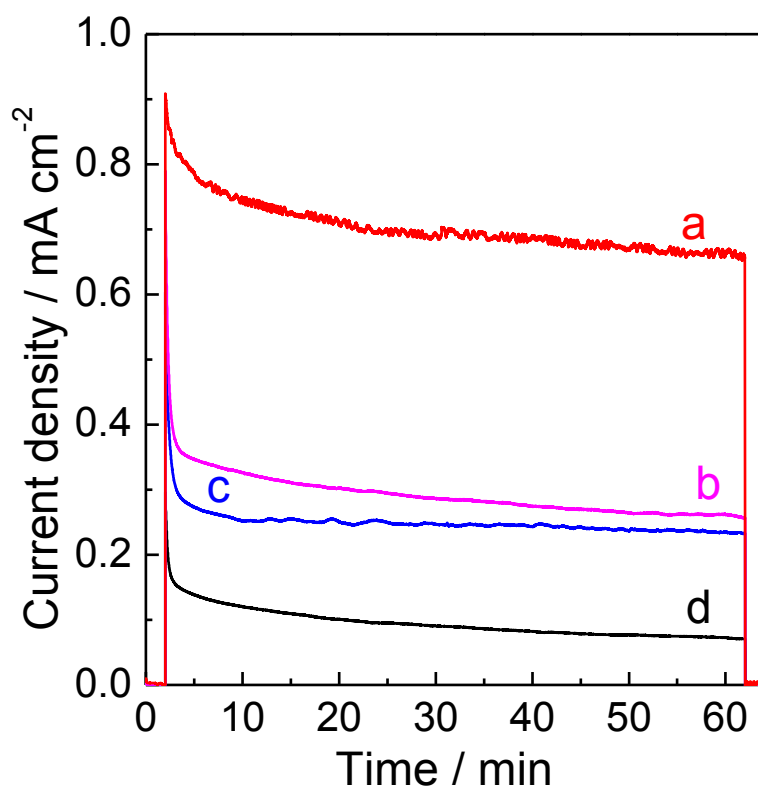


Figure 5-12 Photocurrent density-time profiles for the (d) ITO/neat WO_3 , (a and b) ITO/hydrazine-derived $\text{N}_2 \cdot \text{WO}_3$, and (c) ITO/ammonia-derived $\text{N}_2 \cdot \text{WO}_3$ electrodes calcined at 550°C in the (a) presence and (b-d) absence of 0.1 mM Co^{2+} ions in a 0.1 M phosphate buffer solution of pH 6.0 at 0.5 V vs. Ag/AgCl.

Chapter 6

**Preparation of a nano-structure N₂-Intercalated WO₃
photoanode having highly efficient for
Visible-Light-Driven Water oxidation**

Chapter 6

Preparation of a nano-structure N₂-Intercalated WO₃ photoanode having highly efficient for Visible-Light-Driven Water oxidation

6.1 Introduction

Water splitting by solar light to oxygen and hydrogen in photoelectrochemical (PEC) cells is an attractive but challenging task,^{1,2} following the pioneer work on a TiO₂ photoanode for water splitting by Honda and Fujishima.³ Unfortunately a wide band gap of TiO₂ (3.0-3.2 eV) causes to absorb only an ultraviolet fraction of a solar spectrum (accounts for just 4% of solar irradiation) and consequently responsible for low efficiency in utilization of solar light.⁴⁻⁶ Therefore, intensive researches have been focused on materials with a relatively narrower band gap than TiO₂ to expand light absorption to a visible region. Several single component and composite materials (WO₃, Fe₂O₃, Ta₃N₅, TaON, BaZrO₃-BaTaO₂N, etc.) have been investigated to achieve efficient visible-light-driven water splitting.⁷⁻¹³

WO₃, an n-type semiconductor has attracted immense attention as a photoanode material for water oxidation in PEC cells because of its visible light response (band gap, $E_g = 2.6\text{-}2.8$ eV), a thermodynamically possible valence band edge position for water oxidation (3 V versus the normal hydrogen electrode) and good photochemical stability.¹⁴⁻²⁰ WO₃ has been extensively investigated as promising visible-light-driven photoanode materials for PEC cells since 1976.²¹ So far, a lot of works to narrow the band gap of WO₃ by adding dopants of transition metal (Ti, Fe, Co, Ni, Cu, Zn)^{22,23} other metals (Ga, Dy, Te, Ta, V, Ce)²⁴⁻²⁵⁻²⁹ and representative elements (N, C, S)³⁰⁻³² have been reported to improve the photocatalytic properties of WO₃.

We earlier reported facile preparation of a WO₃ film composed of nano-structured platelets as efficient photoanode materials for visible-light driven

water oxidation by calcination from an ammonium tungstate precursor given by an acid-base reaction of tungstic acid and an ammonium solution followed by deposition with ethanol addition.³³ Recently, Lewis et al. reported a unique WO₃ powder with nitrogen molecules (N₂) intercalated into the crystalline lattice by a similar technique using commercially available ammonium metatungstate ((NH₄)₆H₂W₁₂O₄₀ · xH₂O) and ammonium paratungstate ((NH₄)₁₀H₂W₁₂O₄₂ · 4H₂O) as well as ¹⁵N-labeled ammonium paratungstate synthesized from tungstic acid and aqueous ¹⁵NH₄OH.³⁴ The N₂-intercalated WO₃ provides longer wavelength absorption compared with neat WO₃ due to narrowing the band gap by contribution of N 2p in N₂ to the valence band dominated by O 2p of WO₃. This led to a longer wavelength shift of the photoresponse of the N₂-intercalated WO₃ anode due to photoelectrochemical oxidation of Cl⁻ to Cl₂ in 1.0 M HCl solution. The reported N₂-intercalated WO₃ exhibits mainly monoclinic phase with considerable hexagonal phase, which is an undesirable feature because the photoelectrocatalytic activity of hexagonal WO₃ for water oxidation is well-known to be lower than that of the monoclinic phase.³⁵ Moreover, nanostructure control is effective to improve the photoelectrocatalytic activity of N₂-intercalated WO₃. However, the nano- and micro structure of the N₂-intercalated WO₃ has not been reported yet.

Lewis et al have presumed as an intercalation mechanism of N₂ into WO₃ that NH₄⁺ ions in the solid state can be oxidized to N₂ gas, being catalyzed by tungsten, under O₂ atmosphere, and the N₂ enclosed in solid state is trapped in the hollow center of the crystallized WO₃ lattice during phase transition to orthorhombic WO₃ at ~ 410 °C.³⁴ The N₂-intercalation into the WO₃ lattice could balance N₂ formation with phase transition of WO₃. The nano- and micro structure of the N₂-intercalated WO₃ is significantly influenced by the structure of the precursor because it is formed in a

solid state reaction. On the basis of such notion, we conceive the use of hydrazine as another nitrogen source instead of NH_4^+ . N_2 formation could complete prior to phase transition of WO_3 by use of hydrazine which is easily oxidized to N_2 than ammonia, expecting that a simple crystalline phase of N_2 -intercalated WO_3 . Hydrazine exists mainly as a N_2H_5^+ form in acidic conditions ($\text{p}K_a$ values of $\text{N}_2\text{H}_6^{2+}$ and N_3H_5^+ , -0.9 and 8.1) N_2H_5^+ cations could provide a different structure of a salt precursor with tungstate anions from that of NH_4^+ , resulting in the different structure of N_2 -intercalated WO_3 . Herein, we report the synthesis of N_2 -intercalated WO_3 (denoted as $\text{N}_2 \cdot \text{WO}_3$) using hydrazine as a nitrogen source instead of NH_4^+ . The hydrazine-derived $\text{N}_2 \cdot \text{WO}_3$ exhibits the single phase of a monoclinic crystalline as well as a nano-rodlike structure in contrast to the micro-scale block structure of ammonia-derived $\text{N}_2 \cdot \text{WO}_3$. The hydrazine-derived $\text{N}_2 \cdot \text{WO}_3$ photoanode works efficiently for visible-light driven water oxidation.

6.2 Experimental Section

Materials. The purest grades of tungstic acid (Kanto Chemical Co. Inc.), ammonia aqueous solution, Hydrogen Peroxide (Junsei Chemical Co., Ltd.), and polyethylene glycol (PEG) (Mw=20,000), Tungstgen powder, Hydrozine monohydrate (Wako Pure Chemical Ind., Ltd.), and Marpoloser 60 Mp-50 (Matsumoto Yushi-Seiyaku Co., Ltd.) were purchased and used as received. An indium tin oxide (ITO)-coated glass with 10 Ω/sq of a sheet resistance was purchased from Asahi Glass Co.

Preparations.

Preparation of $\text{N}_2 \cdot \text{WO}_3$ powders and neat WO_3 powder

In a typical synthesis, Tungstic acid (0.3 g, 1.2 mmol) was suspended in 1.5 mL de-ionized water. According to molar ratio of 1:0.08 to 1:10 between H_2WO_4 and N_2H_4 , 4.56-584 μL of $\text{N}_2\text{H}_4 \cdot \text{H}_2\text{O}$ was drop by drop added (0.07-12.0 mmol) to the

above suspension with vigorous stirring to give the white suspensions. After continuous stirring for 30 min, solvent was slowly evaporated to yield various hydrazine-derived precursors. Moreover, a WO_3 was also prepared from a H_2WO_4 synthesized without adding N_2H_4 . An ammonia-derived precursor was synthesized using $\text{NH}_3 \cdot \text{H}_2\text{O}$ (204.0 μL , 3.0 mmol) in a similar manner to the hydrazine-derived precursor. The peroxo-tungstic acid (PTA) as a precursor for neat WO_3 power preparation was synthesized according to the reported method by Sayama.³⁶ 1.46 g (8 mmol) of tungsten powder was carefully dissolved by slow addition of 15 mL aqueous H_2O_2 (30%) in an ice-cold bath and with stirring. The transparent colorless solution was evaporated quickly on a hot stir-plate to decompose excess H_2O_2 and give PTA powder. The PTA powder was re-dissolved in 10 mL hot water and then evaporated to dryness at 70 $^\circ\text{C}$ to yield a PTA precursor. The hydrazine- and ammonia-derived precursors and the PTA precursor were calcined in an electric furnace at 400 ~ 550 $^\circ\text{C}$ with rate of 1 $^\circ\text{C min}^{-1}$ in flowing oxygen atmosphere and then maintained for 1h at this atmosphere to obtain the hydrazine- and ammonium-derived $\text{N}_2 \cdot \text{WO}_3$ powders and neat WO_3 powder.

Fabrication of $\text{N}_2 \cdot \text{WO}_3$ - or WO_3 -coated electrodes

The hydrazine- or ammonia-derived precursor powder (0.2 g), PEG (0.1 g) and Marpolose (20.0 mg) were mixed in water (0.5 mL) with stirring for preparation of a precursor paste. It was coated on an ITO substrate by a squeezing technique and then air-dried for 15 min. The precursor-coated ITO substrate was calcined at 350-550 $^\circ\text{C}$ under oxygen atmosphere to give the hydrazine- or ammonia- $\text{N}_2 \cdot \text{WO}_3$ -coated electrode. The WO_3 -coated electrode was prepared by the same method using a PTA

precursor.

Measurements

XRD data were recorded using an X-ray diffraction spectrometer (Rigaku, MiniFlex 600) using monochromated Cu K α ($\lambda = 1.54 \text{ \AA}$) radiation. SEM images were taken using a scanning electron microscope (JEOL, TSM-6510LV) operated at an accelerating voltage of 10 kV. Nitrogen adsorption-desorption isotherm were measured using a BELSORP-mini II (BEL, Japan) at 77 K. Prior to gas adsorption, the sample powders were degassed in vacuum for 3h at 150 °C. The Brunauer-Emmett-Teller (BET) method was used to calculate the surface areas of the sample powders. Raman spectra were recorded using a Raman microspectroscopic apparatus (Horiba-Jobin-Yvon, LabRAM HR). UV-visible diffuse reflectance spectra (DRS) were recorded on a spectrophotometer (JASCO, V-670) in a DR mode. Thermogravimetric (TG) and Differential Thermal Analysis (DTA) data were taken using a TG analyzer (Rigaku, TG 8120) from 25 to 800 °C with a heating rate of 5 °C min⁻¹ under air.

Photoelectrochemical measurements were conducted using an electrochemical analyzer (HZ-3000, Hokuto Denko Co. Ltd., Tokyo, Japan) and two-compartment photoelectrochemical cell at 25 °C. Three electrode system has been employed using the N₂WO₃-coated electrode and an Ag/AgCl electrode in one compartment as the working and reference electrode, respectively and platinum wire in the other compartment as a counter electrode. A 500 W xenon lamp (Optical ModuleX; Ushio Inc., Japan) as a light source with a UV-cut-filter (L39) and liquid filter (0.2 M CuSO₄) for Photoelectrochemical measurements. A monochromic light with 10 nm of bandwidth was given from a 500 W xenon lamp using a monochromator for incident photon-to-current conversion efficiency (IPCE) measurements. All the

electrochemical and photoelectrochemical experiments were carried out under argon atmosphere in an aqueous 0.1 M phosphate buffer solution (PBS, pH \approx 6.0).

6.3 Results and Discussion

The used amount of N_2H_4 to synthesize precursor was found to have noticeable influence on the morphology of WO_3 sample. Figure 1 shows SEM images of WO_3 samples prepared at 420°C from different precursors powder with different molar ratio between H_2WO_4 and N_2H_4 , from 1:0 to 1:10. The hydrazine-derived $\text{N}_2 \cdot \text{WO}_3$ with nanoflakes structure were observed when the ratio was less than 1:0.08 (Figure 1a, b). It was interesting to note that the nanorod with ~ 200 nm width was started to observe for hydrazine-derived $\text{N}_2 \cdot \text{WO}_3$ prepared with ratio of 1:0.625, though the nanoflake structure was observed simultaneous, as seen from Figure 1c. The clear nanorod with 20-100 nm width was observed when the ratio was 1:2.5 (Figure 1d). With increasing the ratio increased to 1:5 (Figure 1e) and 1:10 (Figure 1f), the sizes of the nanorods became larger due to aggregation of nanorods, as summarized in Table 1.

Compared to WO_3 prepared without using N_2H_4 , the Energy dispersive X-ray spectroscopic (EDS) results clearly showed the presence of nitrogen. The molar ratio of W:N for WO_3 samples prepared at 420°C increased from 1:0.003 to 1:0.121 with increasing the amount of N_2H_4 , as outlined in Table 1.

N_2H_4 amount-dependent XRD experiments (Figure 2) have revealed that the sharp and intensity peaks were observed with increasing the amount of N_2H_4 , suggesting that N_2H_4 is beneficial to promote the growth of crystallinity, and all of WO_3 samples exhibited a monoclinic structure (JCPDS No. 01-083-0950) after

calcination at 420°C.

Figure 3 shows the Raman spectra of WO₃ samples prepared at 420°C from the precursors powder with different amount of N₂H₄. The characteristic signals of the monoclinic phase of peaks at 134.4 cm⁻¹ (lattice vibration), 270.6 cm⁻¹ (δ (O-W-O) deformation vibration), 713.2 cm⁻¹ and 807.1 cm⁻¹ ($\square \square$ (O-W-O) stretching vibration) in a range of Raman shift from 100-1000 cm⁻¹ were observed for all WO₃ samples. These results are consistent with the N₂H₄ amount-dependent XRD experiment. In a region of 2200-2400 cm⁻¹, there was no signal to observe for the WO₃ sample prepared according to the ratio of 1:0. However, a peak at 2330 cm⁻¹ of N₂ molecule (denoted as N₂-mode I) assigned to the N \equiv N vibration intercalated into the WO₃ lattice³⁷⁻³⁹ was began to observe when the hydrazine-derived N₂·WO₃ sample was prepared according to the ratio of 1:0.08 between H₂WO₄ and N₂H₄. As the ratio increased, another broad peak was observed at 2340cm⁻¹ of N₂ molecule (denoted as N₂-mode II) over the ratio of 1:0.625. The earlier report points out that the broad peak is assigned to the N \equiv N vibration of N₂ molecule intercalated in the WO₃ lattice in the different mode.³⁴ Moreover, there was a observable increase for the peak intensity of N₂-mode I and N₂-mode II, especially N₂-mode II, with increasing amount of N₂H₄.

Figure 4 shows the UV-visible diffuse reflectance spectra (DRS) of WO₃ samples prepared at 420°C form different precursors powder which were synthesized with/without utilizing N₂H₄. All the hydrazine-derived N₂·WO₃ samples showed red-shift absorption edges compared to the WO₃ sample prepared from H₂WO₄. The

hydrazine-derived $N_2 \cdot WO_3$ sample prepared from precursors powder with the ratio of 1:0.08 shows a slight red-shift for predominant absorption edge compared to the WO_3 sample prepared from H_2WO_4 due to N_2 intercalation. As the amount of N_2H_4 increased, the absorption shoulders around 480 nm were observed over 1:0.625. The maximum red-shift for predominant absorption edge was found when the ratio of 1:2.5 was used. After that the red-shift for predominant absorption edge exhibited a decrease, but the absorption shoulders around 480 nm increased as the amount of N_2H_4 increased.

To investigate the effect of amount of N_2H_4 on the WO_3 crystal lattice, the lattice parameters of WO_3 prepared without using N_2H_4 and hydrazine-derived $N_2 \cdot WO_3$ samples prepared at 420°C from various precursors powder with different amount of N_2H_4 were analyzed, as shown in Figure 5. The 002, 020, and 200 peak positions, suggested by XRD patterns (Figure 2), reflect the a, b, and c lattice parameter, respectively. The a:b ratio of $N_2 \cdot WO_3$ increased from 0.9746 to 0.9813 with the N_2H_4 amount increased, while also the contents of nitrogen increased, and all of these values exceed that (0.9695) of WO_3 prepared from H_2WO_4 , suggesting the N_2 was intercalated into WO_3 even using less amount of N_2H_4 . Also, Figure 5 shows the dependency of N_2H_4 amount on the N_2 -Mode II: N_2 -Mode I ratio of $N_2 \cdot WO_3$ and the Kubelka-Munk (KM) values at 500 nm, corresponding to absorption shoulders in DRS. The N_2 -Mode II: N_2 -Mode I ratio of $N_2 \cdot WO_3$ was 0 when $N_2 \cdot WO_3$ was prepared according to the ratio of 1:0.08, however, this ratio increased from 0.49 to 0.78 with increasing the amount of N_2H_4 , signifying that N_2 -mode I form prior, and

N₂-mode II is generated at such necessary condition that the existence of high nitrogen contents into WO₃ lattice. Simultaneously, an increase tendency was observed for the KM values at 500 nm of N₂·WO₃, which increased from 0.003 to 0.147, with increasing the amount of N₂H₄. The results of the N₂-Mode II: N₂-Mode I ratio and the Kubelka-Munk (KM) values at 500 nm demonstrate that the absorption shoulder is depended by the formation of N₂-Mode II whether or not.

A SEM technique was used to characterize the nano- and micro- structures of the precursors, N₂·WO₃ and WO₃ powers. The SEM image (Figure 6a) shows that the PTA precursor is composed of the particles with 10 – 50 nm in diameter, being well-connected to each other. In a few places, the spherical particles agglomerate to form large particles. For the ammonia-derived precursor (prepared by a reaction of tungstic acid with an aqueous ammonia solution), the massive blocks in a micro-scale are observed (Figure 6b), instead, the nano-rodlike precursor with 100 nm wide and 500 nm length in average is formed for hydrazine-derived precursor, as shown in Figure 6c. Hydrazine exists mainly as a N₂H₅⁺ form in acidic conditions (pK_a values of N₂H₆²⁺ and N₃H₅⁺, -0.9 and 8.1). The larger size and anisotropic nature of N₂H₅⁺ cations (non-sphere shape; one of nitrogen atoms is protonated) compared with NH₄⁺ cations could be responsible for formation of nano-rodlike precursor. When these precursors were calcined at 550 °C for 1 h for the formation of N₂·WO₃ and WO₃ powers, the nano- and micro-structure is retained for respective precursors, as shown in Figure 6d-f This indicates that the structure controls of the precursors is important for those of N₂·WO₃ and WO₃ powers.

Isotherm of the samples calcined at 420 °C show predominantly type II nature, with some interparticle porosity and the H₂ hysteresis loop in the isotherm (Figure. 7A)

may be caused by roughness of pore and particle surface⁴⁰. The surface area of the samples was calculated by the BET method, as displayed in Table 2. The surface area ($2.27 \text{ m}^2\text{g}^{-1}$) of ammonia-derived $\text{N}_2 \cdot \text{WO}_3$ sample was 9.0 and 7.6 times lower than those of the hydrazine-derived $\text{N}_2 \cdot \text{WO}_3$ sample ($20.6 \text{ m}^2\text{g}^{-1}$) and the neat WO_3 sample ($17.3 \text{ m}^2\text{g}^{-1}$). The formation of the H_2 hysteresis loop for neat WO_3 and hydrazine-derived $\text{N}_2 \cdot \text{WO}_3$ might be possible as an explanation of the higher surface area than ammonia-derived $\text{N}_2 \cdot \text{WO}_3$ sample. The surface area data were summarized in Table 2. N_2 sorption isotherm of the samples calcined at 550°C exhibited type-II characteristics of macroporous materials⁴¹ (Figure 7B). The surface area of the hydrazine-derived $\text{N}_2 \cdot \text{WO}_3$ sample and the neat WO_3 sample reduced to $9.64 \text{ m}^2\text{g}^{-1}$ and $11.1 \text{ m}^2\text{g}^{-1}$, respectively due to the particle size of the samples became larger and the surface of the particle surface became smoother than those of samples calcined at 420°C . The surface of ($2.45 \text{ m}^2\text{g}^{-1}$) of ammonia-derived $\text{N}_2 \cdot \text{WO}_3$ sample was 4.5 and 3.9 times lower than those of the hydrazine-derived $\text{N}_2 \cdot \text{WO}_3$ sample ($11.1 \text{ m}^2\text{g}^{-1}$) and the neat WO_3 sample ($9.64 \text{ m}^2\text{g}^{-1}$). This is consistent with the SEM observation of the massive blocks in a micro-scale of ammonia-derived $\text{N}_2 \cdot \text{WO}_3$ (Figure 6e).

Energy dispersive X-ray spectroscopic (EDS) data (Figure 8) clearly showed the presence of nitrogen for the ammonia- and hydrazine-derived $\text{N}_2 \cdot \text{WO}_3$ samples in comparison with neat WO_3 powers (Figure 8G). The molar ratio of W : N for the hydrazine-derived $\text{N}_2 \cdot \text{WO}_3$ sample after being calcined at 350°C was 1 : 0.005, which is lower compared to the ammonia-derived $\text{N}_2 \cdot \text{WO}_3$ sample (1:0.12). However, the molar ratio of W : N for the hydrazine-derived $\text{N}_2 \cdot \text{WO}_3$ sample calcined at 420°C was 1 : 0.097, which is higher than that (1:0.06) of the the ammonia-derived $\text{N}_2 \cdot \text{WO}_3$ sample calcined at the same temperature. The EDS data were summarized in Table 3. Though these ratios decreased with the calcination temperature for both the $\text{N}_2 \cdot \text{WO}_3$

samples, the ratio (1 : 0.01) for the hydrazine-derived $N_2 \cdot WO_3$ sample is still higher than that (1 : 0.008) for ammonia-derived $N_2 \cdot WO_3$ sample under 550 °C calcination conditions.

XRD data of neat WO_3 and the ammonia- and hydrazine-derived $N_2 \cdot WO_3$ samples prepared at various calcination temperatures are shown in Figure 9. For the neat WO_3 powder, WO_3 with both the monoclinic and hexagonal (peak at $2\theta = 13.9^\circ$; 28.1° and 36.7° assigned to 100, 200 and 201) phases was formed at less than 400 °C though the peaks are relatively broad. The crystallite diameters for monoclinic and hexagonal phase were calculated from the peaks at 24.3° and 13.9° by Scherrer equation using D_{200} , D_{100} parameter (13 nm, 16 nm), respectively. When the calcination temperature increased from 400 to 550 °C, the monoclinic phase was predominantly formed with the crystallite diameter increased (Table 4). For the ammonia-derived $N_2 \cdot WO_3$ sample, the hexagonal phase was observed with the monoclinic phase less than 500 °C, being consistent with the XRD data reported earlier.³⁴ This result shows that hexagonal phase of ammonia-derived $N_2 \cdot WO_3$ sample is more stabilized compared with the neat WO_3 sample. For the hydrazine-derived $N_2 \cdot WO_3$ sample, clear monoclinic phase was observed even at 400 °C (no hexagonal phase). This result shows that the monoclinic phase of hydrazine-derived $N_2 \cdot WO_3$ sample is more stable compared to the neat WO_3 sample, in contrast to the ammonia-derived $N_2 \cdot WO_3$ sample. It is notified that the crystallite diameter (21 nm) of the monoclinic phase for hydrazine-derived $N_2 \cdot WO_3$ sample calcined at 400 °C is larger than those of the ammonia-derived $N_2 \cdot WO_3$ sample (19 nm) and the neat WO_3 sample (15 nm) calcined at 400 °C. This shows that crystallization of the monoclinic phase facilitates for the hydrazine-derived $N_2 \cdot WO_3$ sample compared with the other samples.

In order to reveal the effect of N_2 intercalation on the a, b, and c lattice parameter of neat WO_3 , ammonia- and hydrazine-derived $N_2 \cdot WO_3$ samples after being calcined at various temperatures were analyzed as shown in Figure 10A. For neat WO_3 sample, there was no noticeable change for the a:b ratio of 0.969 at each of temperature. The a:b ratio of ammonia-derived $N_2 \cdot WO_3$ sample decreased from 0.9738 to 0.9702 with the calcination temperatures increased. However, the a:b ratio of hydrazine-derived $N_2 \cdot WO_3$ sample increased from 0.9734 to 0.9798 with temperature increased from 350 °C to 420 °C, and then the ratio decreased from 0.9773 to 0.9736 with increasing the temperatures from 430 °C to 550 °C. The difference increase mode of the a:b ratio for ammonia- and hydrazine-derived $N_2 \cdot WO_3$ samples indicate the mode of crystallite growth for $N_2 \cdot WO_3$ samples are different. The crystallite growth proceeded along the b axis at all temperatures for the ammonia-derived $N_2 \cdot WO_3$. However, the growth of $N_2 \cdot WO_3$ crystallite proceeded along the a and b axes, especially the a axis growth is predominant for hydrazine-derived $N_2 \cdot WO_3$ samples prepared from 350 °C to 420 °C, the growth of the crystallite proceeded along the b axis with the temperature increased from 430 °C to 550 °C. In addition, the a:b ratio values for both ammonia- and hydrazine-derived $N_2 \cdot WO_3$ samples exceeded that of neat WO_3 samples, indicating that the N_2 molecule was intercalated into the WO_3 at all temperatures and improve the symmetry of the WO_3 lattice. The hydrazine-derived $N_2 \cdot WO_3$ sample possesses the highest symmetry than those of ammonia-derived $N_2 \cdot WO_3$ and neat WO_3 samples. The difference of crystallite growth mode suggests the patterns of embedding N_2 molecule are different in WO_3 lattice. The N_2 molecule might be intercalated into WO_3 lattice alone the b axis for ammonia-derived $N_2 \cdot WO_3$. On the contrary, the N_2 molecule would be intercalated into WO_3 lattice alone a axis below 420 °C and alone the b axis over 420 °C for hydrazine-derived $N_2 \cdot WO_3$ sample.

To reveal the dependency of calcination temperature on trapped amount of N_2 into WO_3 lattice, the effect of calcination temperature on the WO_3 lattice volume was investigated, as shown in Figure 10B. There was no observable change for the lattice volume of neat WO_3 (135 \AA^3) at each temperature. The lattice volume of ammonia-derived $N_2 \cdot WO_3$ sample decreased from 170 to 139 \AA^3 with the increased the annealing temperatures due to the decrease of N_2 molecule into WO_3 lattice. However, the lattice volume of hydrazine-derived $N_2 \cdot WO_3$ sample show an increase tendency at a region of 350 to 420°C , while the the lattice volume increased from 137 to 165 \AA^3 , which indicates that the amount of trapped N_2 into WO_3 lattice was maximum as hydrazine-derived $N_2 \cdot WO_3$ sample after being calcined at 420°C . This tendency is agreement with the EDS data. The lattice volume decreased from 164 to 143 \AA^3 with increasing the temperature from 430 to 550°C . Figure 10 suggests that the crystallite growth proceed alone a axis, corresponding to intercalating N_2 molecule alone the a axis, is benefit to trap N_2 molecule into lattice.

Raman spectra of the ammonia-derived $N_2 \cdot WO_3$ samples prepared at various calcination temperatures are shown in Figure 11. Raman spectra of the ammonia-derived $N_2 \cdot WO_3$ sample calcined at 550°C exhibited the characteristic signals of the monoclinic phase at 139.9 cm^{-1} (lattice vibration), 276.5 cm^{-1} (δ (O-W-O) deformation vibration), 697.1 cm^{-1} and 799.2 cm^{-1} ($\square \square$ (O-W-O) stretching vibration) in a range of Raman shift from $100 \sim 1000 \text{ cm}^{-1}$. In calcination at less than 500°C , the characteristic signals of the hexagonal phase of peaks marked by asterisk in Figure 12A (132.8 cm^{-1} (lattice vibration), 270.8 cm^{-1} (δ (O-W-O) deformation vibration), 713.3 cm^{-1} , and 805.9 cm^{-1} (\square (O-W-O) stretching vibration) were observed in addition to the characteristic signals of the monoclinic phase. This result is agreement with the XRD patterns of the ammonia-derived $N_2 \cdot WO_3$ sample measured by various

calcination temperature. In a region of 2200 ~2400 cm^{-1} (Figure 12) a peak was observed at 2328 ~ 2330 cm^{-1} assigned to the $\text{N}\equiv\text{N}$ vibration intercalated into the WO_3 lattice³⁷⁻³⁹ for the ammonia-derived $\text{N}_2 \cdot \text{WO}_3$ sample calcined at less than 400 $^{\circ}\text{C}$. As the calcination temperature increased, the additional N_2 molecule broad peak assigned to the $\text{N}\equiv\text{N}$ vibration in the different mode was observed at 2340 cm^{-1} over 420 $^{\circ}\text{C}$. Figure 12B suggests that the N_2 -mode I intercalated in the WO_3 lattice is predominantly generated at lower calcination temperature and N_2 -mode II intercalated is then generated as the crystallization proceeds at more than 420 $^{\circ}\text{C}$.

Raman spectra of the hydrazine-derived $\text{N}_2 \cdot \text{WO}_3$ sample exhibited the characteristic signals of the monoclinic phase alone in a range of 100 ~ 1000 cm^{-1} (Figure 13), being consistent with the XRD data. In a region of 2200 ~2400 cm^{-1} (Figure 13B), the peaks at 2328 ~ 2330 cm^{-1} and 2340 cm^{-1} , assigned to the $\text{N}\equiv\text{N}$ vibration of both N_2 -mode I and II were observed at more than 400 $^{\circ}\text{C}$. The observation of both N_2 -mode I and II compared with N_2 -mode I alone for the ammonia-derived $\text{N}_2 \cdot \text{WO}_3$ sample at 400 $^{\circ}\text{C}$ is ascribed to crystallization at the low temperature for the hydrazine-derived $\text{N}_2 \cdot \text{WO}_3$ sample as indicated in the XRD data (Figure 9C).

Figure 14 shows the effect of crystallization temperature on the N_2 -mode II: N_2 -mode I ratio of ammonia- and hydrazine-derived $\text{N}_2 \cdot \text{WO}_3$ samples. The N_2 -mode II: N_2 -mode I ratio of hydrazine-derived $\text{N}_2 \cdot \text{WO}_3$ sample exhibited an increase less than 420 $^{\circ}\text{C}$ and a decrease over 420 $^{\circ}\text{C}$, which implies that the intensity of N_2 -mode II is dependent on trapped contents of nitrogen. In contrast of hydrazine-derived $\text{N}_2 \cdot \text{WO}_3$ sample, the N_2 -mode II: N_2 -mode I ratios of ammonia- $\text{N}_2 \cdot \text{WO}_3$ were 0 below annealing temperature of 420 $^{\circ}\text{C}$ in spite of existence of high N_2 contents. It is attributed to that the crystallization of ammonia- $\text{N}_2 \cdot \text{WO}_3$ is

predominant rather than formation of N₂-mode II at low calcination temperature. The decrease of N₂-mode II:N₂-mode I ratios of ammonia- N₂ ·WO₃ were observed from 420 °C to 550 °C. The results of N₂-mode II:N₂-mode I indicate that the intensity of N₂-mode II is not only dependent on trapped contents of nitrogen but also the crystallinity of sample.

DRS data of neat WO₃ and the ammonia- and hydrazine-derived N₂ ·WO₃ samples prepared at 420°C are shown in Figure 15. There were noticeable change in color for both N₂ ·WO₃ samples after being calcined at 420°C, while the color changed from the pale green of neat WO₃ sample to the orange and dark yellow for hydrazine-derived N₂ ·WO₃ and ammonia-derived N₂ ·WO₃ samples, respectively. The neat WO₃ sample exhibited the wavelength of onset of light absorption was around at 470 nm, which is equivalent to 2.7 eV of band gap energy. Compared to the neat WO₃, the UV-vis reflectance of ammonia- and hydrazine-derived N₂ ·WO₃ samples prepared at 420°C, red-shift of predominant absorption edges were observed, and the absorption shoulders were observed around at 480 nm simultaneously. Though the red-shift of predominant absorption edges were still observed for both the ammonia- and hydrazine-derived N₂ ·WO₃ samples calcined at 550°C, as shown in Figure 15 inset, the absorption shoulders of both N₂ ·WO₃ samples were not observed due to the decrease of N₂ contents into WO₃ lattice, and thus, the color of both the ammonia- and hydrazine-derived N₂ ·WO₃ samples changed to yellow green, similar to that of neat WO₃ sample.

Figure 16 shows the dependence of calcination temperatures on Kubelka-Munk (KM) values at 500 nm. KM values at 500 nm of the neat WO₃ samples almost no changes were observed at all temperatures. But for ammonia-derived N₂ ·WO₃ sample, KM values decreased with increasing the annealing temperature due to the contents of

N_2 molecule in WO_3 lattice gradually decreased with the temperature increased. On the other hand, the KM values at 500 nm of hydrazine-derived $N_2 \cdot WO_3$ sample increased as the temperatures increased in the range from 350 to 420°C, owing to amount of the N_2 in WO_3 lattice increased with increasing the temperature. After 420°C, these values decreased with the amount of the N_2 decreased until the value was closed to that of neat WO_3 sample prepared at 550°C.

What is more, the tendency of the plots of KM values for ammonia- and hydrazine-derived $N_2 \cdot WO_3$ samples are similar to those data shown in Figure 10, indicating the KM values at 500 nm, corresponding to the absorption shoulders in DRS spectra, depend on the amount of embedded N_2 into WO_3 lattice.

The TG curve shows that the ammonia-derived precursor is gradually converted to $N_2 \cdot WO_3$ from room temperature to 400 °C with 13% weight loss, and the DTA curve shows endothermic peaks over 320 ~ 385 °C. (Figure 17A) This involves convoluted processes involving 1) oxidation of NH_3^+ to N_2 catalyzed by tungsten species, 2) conversion of the producer to WO_3 and N_2 intercalation to form $N_2 \cdot WO_3$ and 3) subsequent crystallization of $N_2 \cdot WO_3$.

Contrastively, the hydrazine-derived precursor is precipitously converted to WO_3 at 266 °C with 14% weight loss, as shown in Figure 17B. The DTA curve shows three endothermic peaks: a very sharp and intense peak at 270 °C, a relatively broad peak at 285 °C and a weak peak at 367 °C. The precipitous weight loss with an endothermic process could be ascribed to oxidation of $N_2H_5^+$ to N_2 catalyzed by tungsten species and conversion of the producer to WO_3 , and crystallization. This indicates that intense endothermic process is involved in the WO_3 formation.

The PEC properties of the ITO/ WO_3 electrodes prepared at 550°C were studied

in a 0.1 M phosphate solution with pH adjusted to 6.0. Cyclic voltammograms (CVs) of the neat WO_3 , ammonia- and hydrazine-derived $\text{N}_2 \cdot \text{WO}_3$ electrodes are shown in Figure 18, where the redox response of $\text{H}_x\text{WO}_3 / \text{WO}_3$ were observed below 0.2 V vs. Ag/AgCl, however, no anodic currents were observed under the dark condition in a potential range of 0.2 ~ 1.0 V vs. Ag/AgCl for all of electrodes due to n-type Schottky barrier at the interfacial heterojunction between the electrodes surface and the electrolyte solution. Upon irradiation of visible light, the photoanodic currents were observed over 0.2 V vs. Ag/AgCl due to water oxidation for all electrodes. The photoanodic current of 2.1 mA cm^{-2} at 1.0 V vs. Ag/AgCl was observed for hydrazine-derived $\text{N}_2 \cdot \text{WO}_3$ electrode (Figure 18C), which is about 2 and 4 times higher than that of ammonia-derived $\text{N}_2 \cdot \text{WO}_3$ electrode (1.1 mA cm^{-2} at 1.0 V vs. Ag/AgCl, Figure 18B) and neat WO_3 electrode (0.35 mA cm^{-2} at 1.0 V vs. Ag/AgCl, Figure 18A).

In order to reveal the effect of the calcination temperature on the PEC activity, the photocurrents were measured by using the neat WO_3 , ammonia- and hydrazine-derived $\text{N}_2 \cdot \text{WO}_3$ electrodes after being calcined at 350-550°C (Figure 19). The anodic current ($0.02 \sim 0.05 \text{ mA cm}^{-2}$ at 1.0 V vs. Ag/AgCl) were hardly generated for both neat WO_3 and $\text{N}_2 \cdot \text{WO}_3$ electrodes calcined at 350 °C due to their insufficient crystallinity. Crystallinity rather than N_2 intercalation for $\text{N}_2 \cdot \text{WO}_3$ samples calcined at 350 °C is a dominant factor for the PEC performance of the WO_3 -based photoanode.^{14,19} The photoanodic currents were begun to observed for $\text{N}_2 \cdot \text{WO}_3$ electrodes after being calcined at 400 °C. The photoanodic current ($0.16 \pm 0.02 \text{ mA}$

cm^{-2} at 1.0 V vs. Ag/AgCl) of hydrazine-derived $\text{N}_2 \cdot \text{WO}_3$ sample is about 4.2 and 10.8 times higher compared to those of ammonia-derived $\text{N}_2 \cdot \text{WO}_3$ ($0.038 \pm 0.01 \text{ mA cm}^{-2}$ at 1.0 V vs. Ag/AgCl) and neat WO_3 sample ($0.014 \pm 0.004 \text{ mA cm}^{-2}$ at 1.0 V vs. Ag/AgCl) due to crystallization of clear monoclinic phase even calcination at the low temperature. Moreover, only N_2 -mode I was observed for ammonia-derived $\text{N}_2 \cdot \text{WO}_3$ sample calcined at 400 $^{\circ}\text{C}$, however, the formation of N_2 -mode II was found in Raman spectra for hydrazine-derived $\text{N}_2 \cdot \text{WO}_3$ sample, suggesting that N_2 -mode II is contribute to generating photoanodic current. After being calcined at 420 $^{\circ}\text{C}$, the photoanodic current of the hydrazine-derived $\text{N}_2 \cdot \text{WO}_3$ electrode was reached at $1.0 \pm 0.098 \text{ mA cm}^{-2}$ at 1.0 V vs. Ag/AgCl, which is about 3.6 times 20 times higher compared to the ammonia-derived $\text{N}_2 \cdot \text{WO}_3$ sample ($0.28 \pm 0.008 \text{ mA cm}^{-2}$ at 1.0 V vs. Ag/AgCl) and neat sample ($0.05 \pm 0.005 \text{ mA cm}^{-2}$ at 1.0 V vs. Ag/AgCl), respectively. The high PEC water oxidation performance of hydrazine-derived $\text{N}_2 \cdot \text{WO}_3$ electrode calcined at 420 $^{\circ}\text{C}$ due to its high crystallinity, nanorod structure which offer high surface area and expeditious electron migration along a rod axis, and high content of N_2 molecule in WO_3 lattice. The significant high photocurrents were observed for both neat WO_3 electrode and $\text{N}_2 \cdot \text{WO}_3$ electrodes due to the formation of sufficient crystallinity with increasing the temperature. The $\text{N}_2 \cdot \text{WO}_3$ electrodes exhibited higher photocurrents than that of neat WO_3 electrode, especially the best photocurrent of $2.2 \pm 0.1 \text{ mA cm}^{-2}$ at 1.0 V was obtained for the hydrazine-derived $\text{N}_2 \cdot \text{WO}_3$ sample 550 $^{\circ}\text{C}$. At this condition, though the decrease of content of N_2 molecule was observed from the EDS data, the content of N_2 molecule for hydrazine-derived $\text{N}_2 \cdot \text{WO}_3$ electrode is

still higher compared to the ammonia-derived $N_2 \cdot WO_3$ sample, which would utilize visible light efficiently to enhance the PEC water oxidation performance. Furthermore, the higher crystallinity and morphology of nanorod or hydrazine-derived $N_2 \cdot WO_3$ electrode are also the essential factors to generate higher photocurrent.

In Figure 20, the action spectra of IPCE at 0.5 V versus Ag/AgCl was measured with changing wavelength of illumination monochromatic light using different ITO/ WO_3 photoanodes. For neat WO_3 electrode, the photocurrent was generated below 470 nm with band gap energy of 2.63 eV. This indicates that the photocurrent is generated by the band gap excitation of the WO_3 . For ammonium-derived $N_2 \cdot WO_3$ electrode prepared at 420°C, the photocurrent was generated below 510 nm with a band gap energy of 2.43 eV and IPCE at 400 nm was 4.1%. The hydrazine-derived $N_2 \cdot WO_3$ sample showed significant enhancement in photoresponse with the photoresponse position red-shift to 520 nm with a band gap energy of 2.38 eV. The on-set wavelength 520 nm of action spectrum corresponds to the absorption edge of the diffused reflectance spectrum of the hydrazine-derived $N_2 \cdot WO_3$ electrode. This corroborates that the photoanodic current is based on a band gap photoexcitation of $N_2 \cdot WO_3$. The IPCE at 400 nm was 5.3% is about 7.5 times higher than that of pure WO_3 films (0.7%) as depicted in Figure 20A. The IPCE of the different electrodes prepared at 550°C are shown in Figure 20B, where the photoreponse position decreased to 490 nm for both ammonium-derived $N_2 \cdot WO_3$ and hydrazine-derived $N_2 \cdot WO_3$ electrodes due to decrease of the contents of N_2 compare to that of electrodes prepared at 420°C. Though the contents of N_2 decreased, the crystallinity of all WO_3

electrodes increased after being calcined at 550°C. Therefore, the IPCE values for both neat WO₃ and N₂·WO₃ electrodes increased compared to those of electrodes calcined at 420 °C. The IPCE at 400nm of the hydrazine-derived N₂·WO₃ (50%) is about 2.5 and 7 times higher than that of ammonium-derived N₂·WO₃ (20%) and neat WO₃ (7%), respectively.

6.4 References

- (1) Gratzel, M. *Nature* **2001**, *414*, 338.
- (2) Minggu, L. J.; Wan Daud, W. R.; Kassim, M. B. *Int. J. Hydrogen Energy* **2010**, *35*, 5233.
- (3) Fujishima, A.; Honda, K. *Nature* **1972**, *238*, 37.
- (4) Kudo, A.; Miseki, Y. *Chem. Soc. Rev.* **2009**, *38*, 253.
- (5) Ho, W.; Yu, J. C.; Lee, S. *Chem. Commun.* **2006**, 1115.
- (6) Cong, Y.; Zhang, J.; Chen, F.; Anpo, M. *J. Phys. Chem. C* **2007**, *111*, 6976.
- (7) Chandra, D.; Saito, K.; Yui, T.; Yagi, M. *Angew. Chem. Int. Ed.* **2013**, *52*, 12606.
- (8) Satsangi, V.; Kumari, S.; Singh, A.; Shrivastav, R.; Dass, S. *Int. J. Hydrogen Energy* **2008**, *33*, 312.
- (9) Li, Y.; Takata, T.; Cha, D.; Takanabe, K.; Minegishi, T.; Kubota, J.; Domen, K. *Adv. Mater.* **2013**, *25*, 125.
- (10) Abe, R.; Takata, T.; Sugihara, H.; Domen, K. *Chem. Commun.* **2005**, 3829.
- (11) Maeda, K.; Domen, K. *Angew. Chem. Int. Ed.* **2012**, *51*, 9865.
- (12) Chatchai, P.; Murakami, Y.; Kishioka, S.-y.; Nosaka, A. Y.; Nosaka, Y.

Electrochim. Acta **2009**, *54*, 1147.

(13) Hisatomi, T.; Dotan, H.; Stefik, M.; Sivula, K.; Rothschild, A.; Grätzel, M.; Mathews, N. *Adv. Mater.* **2012**, *24*, 2699.

(14) Santato, C.; Odziemkowski, M.; Ulmann, M.; Augustynski, J. *J. Am. Chem. Soc.* **2001**, *123*, 10639.

(15) Santato, C.; Ulmann, M.; Augustynski, J. *J. Phys. Chem. B* **2001**, *105*, 936.

(16) Santato, C.; Ulmann, M.; Augustynski, J. *Adv. Mater.* **2001**, *13*, 511.

(17) Baeck, S. H.; Jaramillo, T.; Stucky, G. D.; McFarland, E. W. *Nano Lett.* **2002**, *2*, 831.

(18) Berger, S.; Tsuchiya, H.; Ghicov, A.; Schmuki, P. *Appl. Phys. Lett.* **2006**, *88*.

(19) Yang, B.; Zhang, Y.; Drabarek, E.; Barnes, P. R. F.; Luca, V. *Chem. Mater.* **2007**, *19*, 5664.

(20) Wang, H.; Lindgren, T.; He, J.; Hagfeldt, A.; Lindquist, S.-E. *J. Phys. Chem. B* **2000**, *104*, 5686.

(21) Hodes, G.; Cahen, D.; Manassen, J. *Nature* **1976**, *260*, 312.

(22) Hameed, A.; Gondal, M. A.; Yamani, Z. H. *Catal. Commun.* **2004**, *5*, 715.

(23) Radecka, M.; Sobas, P.; Wierzbicka, M.; Rekas, M. *Phys. B* **2005**, *364*, 85.

(24) Ng, K.; Minggu, L.; Kassim, M. *Int. J. Hydrogen Energy* **2013**, *38*, 9585.

(25) Liu, H.; Peng, T.; Ke, D.; Peng, Z.; Yan, C. *Mater. Chem. Phys.* **2007**, *104*, 377.

(26) Yang, B.; Luca, V. *Chem. Commun.* **2008**, 4454.

(27) Enesca, A.; Duta, A.; Schoonman, J. *Phys. Status Solidi A* **2008**, *205*, 2038.

- (28) Karuppasamy, K. M.; Subrahmanyam, A. *J. Phys. D: Appl. Phys.* **2008**, *41*, 035302.
- (29) Xueting, C.; Shibin, S.; Yun, Z.; Lihua, D.; Yansheng, Y. *Nanotechnology* **2011**, *22*, 265603.
- (30) Cole, B.; Marsen, B.; Miller, E.; Yan, Y.; To, B.; Jones, K.; Al-Jassim, M. *J. Phys. Chem. C* **2008**, *112*, 5213.
- (31) Sun, Y.; Murphy, C. J.; Reyes-Gil, K. R.; Reyes-Garcia, E. A.; Thornton, J. M.; Morris, N. A.; Raftery, D. *Int. J. Hydrogen Energy* **2009**, *34*, 8476.
- (32) Li, W.; Li, J.; Wang, X.; Chen, Q. *Appl. Surf. Sci.* **2012**, *263*, 157.
- (33) Yagi, M.; Maruyama, S.; Sone, K.; Nagai, K.; Norimatsu, T. *J. Solid State Chem.* **2008**, *181*, 175.
- (34) Mi, Q.; Ping, Y.; Li, Y.; Cao, B.; Brunschwig, B. S.; Khalifah, P. G.; Galli, G. A.; Gray, H. B.; Lewis, N. S. *J. Am. Chem. Soc.* **2012**, *134*, 18318.
- (35) Szilágyi, I. M.; Fórizs, B.; Rosseler, O.; Szegedi, Á.; Németh, P.; Király, P.; Tárkányi, G.; Vajna, B.; Varga-Josepovits, K.; László, K.; Tóth, A. L.; Baranyai, P.; Leskelä, M. *J. Catal.* **2012**, *294*, 119.
- (36) Sayama, K.; Hayashi, H.; Arai, T.; Yanagida, M.; Gunji, T.; Sugihara, H. *Appl. Catal. B* **2010**, *94*, 150.
- (37) Tessier, F.; Le Gendre, L.; Cheviré, F.; Marchand, R.; Navrotsky, A. *Chem. Mater.* **2005**, *17*, 3570.
- (38) Rachel, A.; Ebbinghaus, S. G.; Güngerich, M.; Klar, P. J.; Hanss, J.; Weidenkaff, A.; Reller, A. *Thermochim. Acta* **2005**, *438*, 134.

- (39) Bendtsen, J.; Rasmussen, F. *J. Raman Spectrosc.* **2000**, *31*, 433.
- (40) Grosman, A.; Ortega, C. *Langmuir* **2008**, *24*, 3977.
- (41) Hernandez-Uresti, D. B.; Sánchez-Martínez, D.; Martínez-de la Cruz, A.; Sepúlveda-Guzmán, S.; Torres-Martínez, L. M. *Ceram. Int.* **2014**, *40*, 4767.

Table 6-1 The effect of utilizing amount of N_2H_4 on various properties of WO_3 samples after being calcined at 420°C .

H_2WO_4 (mmol)	N_2H_4 (μL)	$n_{\text{H}_2\text{WO}_4} : n_{\text{N}_2\text{H}_4}$	W : N	Type of nanostructure	Dimension of nanorod
1.20	0	1:0	0	Nanoflakes	-
1.20	4.56	1:0.08	1:0.003	Nanoflakes	-
1.20	36.5	1:0.625	1:0.062	Nanoflakes and nanorods	-200 nm
1.20	146.0	1:2.5	1:0.095	Nanorods	20 nm -100 nm
1.20	292.0	1:5	1:0.11	Nanorods	30 nm-120 nm
1.20	584.0	1:10	1:0.121	Nanorods	100 nm-150 nm

Table 6-2 Physicochemical proprieties of Neat WO_3 , NH_3 -derived $\text{N}_2 \cdot \text{WO}_3$, and N_2H_4 -derived $\text{N}_2 \cdot \text{WO}_3$ samples calcined at 420°C and 550 °C.

Sample	Calcination temperature / °C	Surface area ($\text{m}^2 \text{g}^{-1}$)
Neat WO_3	420 °C	17.3
NH_3 -derived $\text{N}_2 \cdot \text{WO}_3$	420 °C	2.26
N_2H_4 -derived $\text{N}_2 \cdot \text{WO}_3$	420 °C	20.6
Neat WO_3	550 °C	9.64
NH_3 -derived $\text{N}_2 \cdot \text{WO}_3$	550 °C	2.25
N_2H_4 -derived $\text{N}_2 \cdot \text{WO}_3$	550 °C	11.1

Table 6-3 EDS data of NH_3 -derived N_2WO_3 and N_2H_4 -derived N_2WO_3 samples calcined at 350 °C, 420°C, and 550 °C.

Sample name	Calcination temperature / °C	Molar ratio of W : N
NH_3 -derived N_2WO_3	350	1:0.12
N_2H_4 -derived N_2WO_3	350	1:0.005
NH_3 -derived N_2WO_3	420	1:0.097
N_2H_4 -derived N_2WO_3	420	1:0.06
NH_3 -derived N_2WO_3	550	1:0.008
N_2H_4 -derived N_2WO_3	550	1:0.01

Table 6-4 The crystallite diameters base on the (200) peak (D_{200}) of Neat WO_3 , NH_3 -derived $\text{N}_2 \cdot \text{WO}_3$, and N_2H_4 -derived $\text{N}_2 \cdot \text{WO}_3$ samples calcined at 350°C-550 °C.

Sample	Neat WO_3	NH_3 -derived $\text{N}_2 \cdot \text{WO}_3$	N_2H_4 -derived $\text{N}_2 \cdot \text{WO}_3$
Temperature	Crystallite diameter (D_{200}) nm		
350 °C	12	18	20
400 °C	15	19	21
420 °C	23	25	31
450 °C	27	28	36
500 °C	28	32	39
550 °C	29	34	42

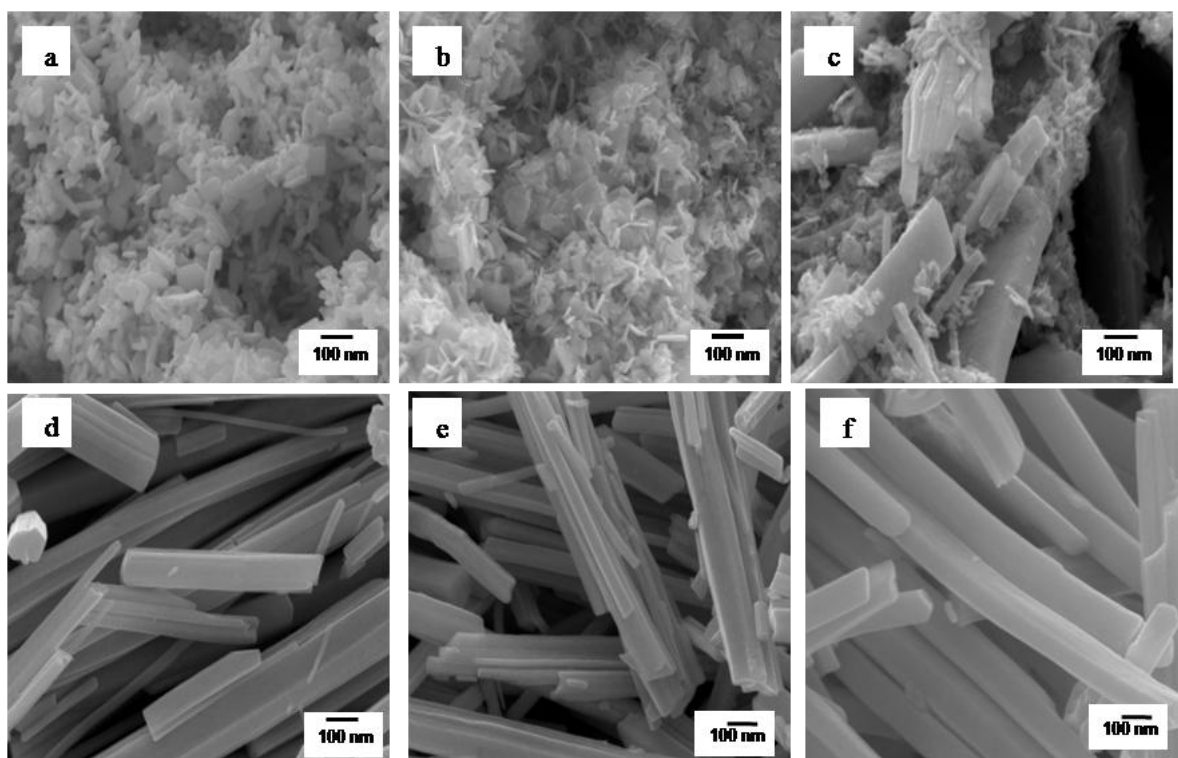


Figure 6-1 Morphology of WO_3 samples prepared at 420°C from different precursors powder which were synthesized according to the molar ratio of (a) 1:0, (b) 1:0.08, (c) 1:0.625, (d) 1:2.5, (e) 1:5, and (f) 1:10 between H_2WO_4 and N_2H_4 .

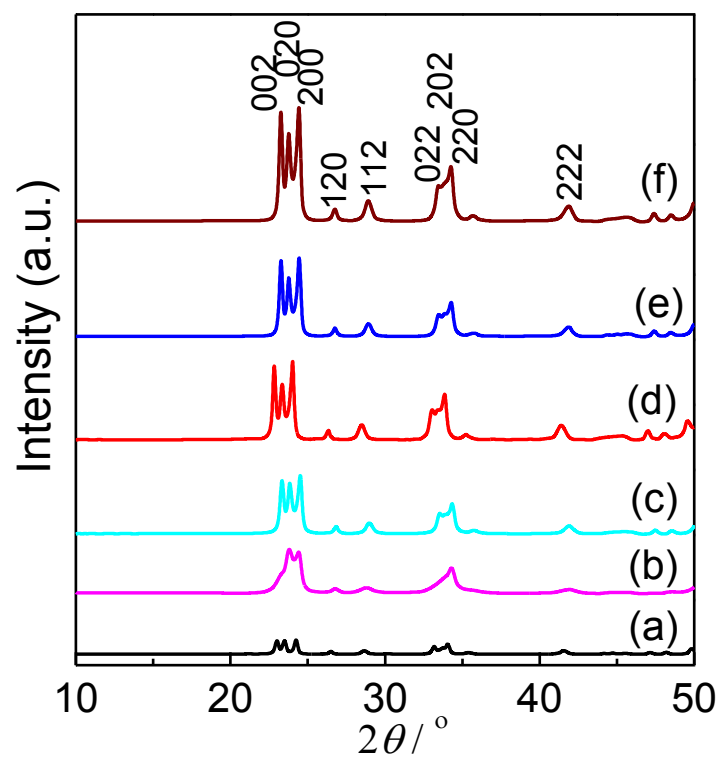


Figure 6-2 XRD patterns of WO_3 samples prepared according to the molar ratio of (a) 1:0, (b) 1:0.08, (c) 1:0.625, (d) 1:2.5, (e) 1:5, and (f) 1:10 between H_2WO_4 and N_2H_4 after being calcined at 420°C .

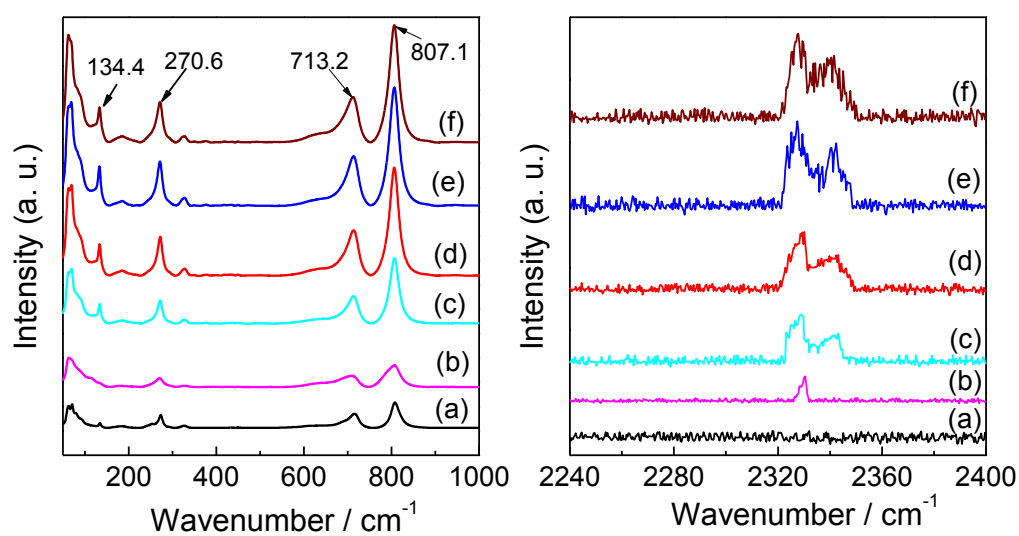


Figure 6-3 Raman spectra of WO_3 samples prepared from different precursors powder with different molar ratio of (a) 1:0, (b) 1:0.08, (c) 1:0.625, (d) 1:2.5, (e) 1:5, and (f) 1:10 between H_2WO_4 and N_2H_4 followed by calcination at 420°C .

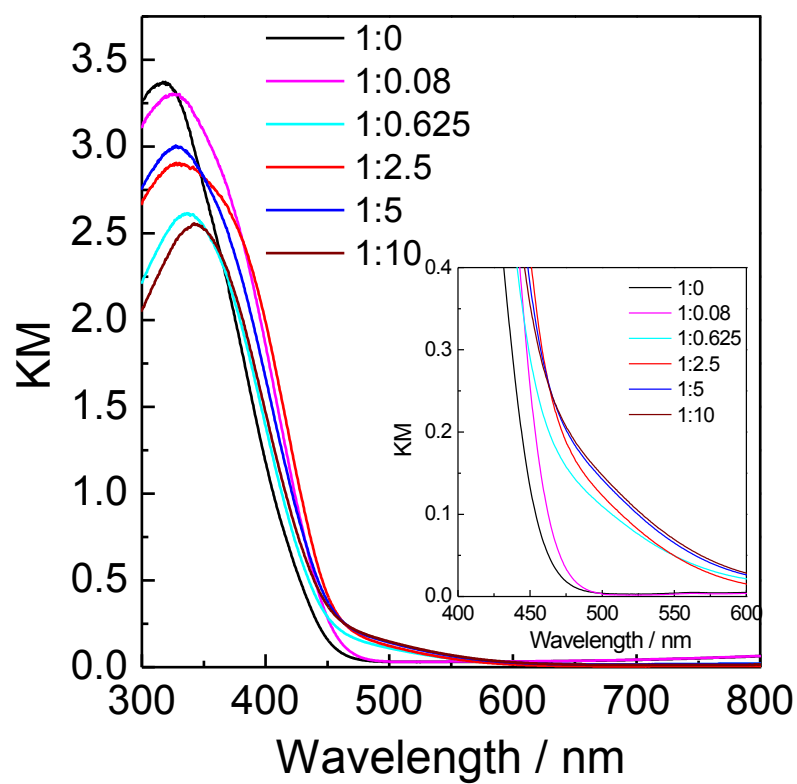


Figure 6-4 UV-vis diffuse reflectance spectra (DRS) of WO_3 samples prepared from different precursors powder with different molar ratio of (a) 1:0, (b) 1:0.08, (c) 1:0.625, (d) 1:2.5, (e) 1:5, and (f) 1:10 between H_2WO_4 and N_2H_4 followed by calcination at 420°C .

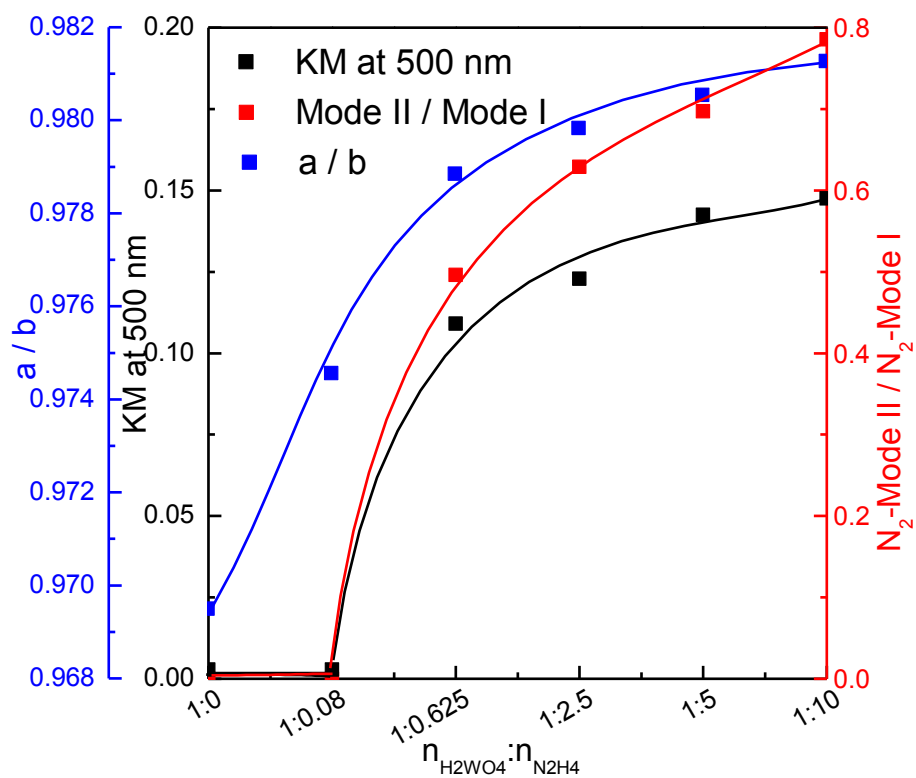


Figure 6-5 The influence of N_2H_4 amount on Kubelka-Munk (KM) value at 500nm, a:b ratio, and $\text{N}_2\text{-ModeII} : \text{N}_2\text{-ModeI}$ ratio for various WO_3 samples calcined at 420°C .

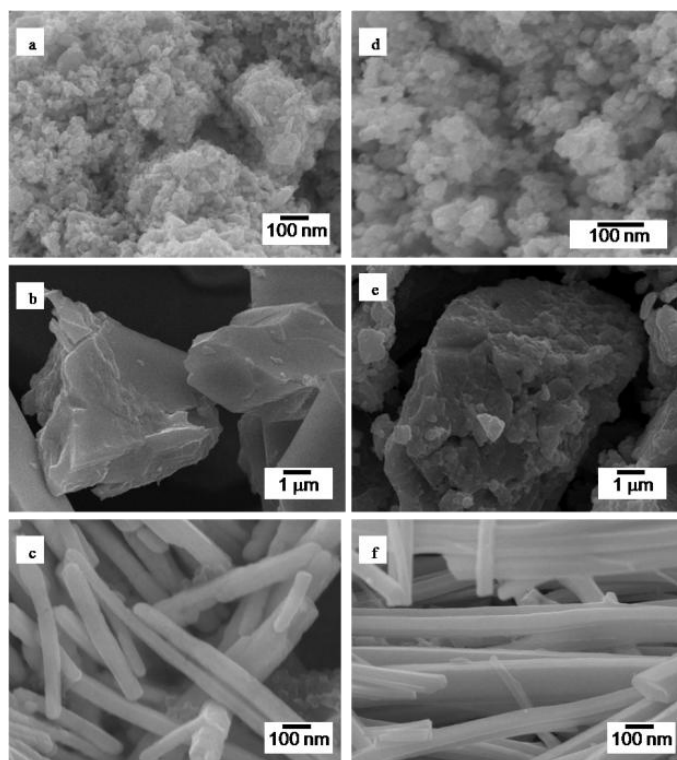


Figure 6-6 SEM images of (a) PTA precursor, (b) ammonia-derived precursor, and (c) hydrazine- derived precursor. (d) Neat WO₃, (e) ammonia-derived N₂·WO₃, and (f) hydrazine-derived N₂·WO₃ prepared at 550 °C.

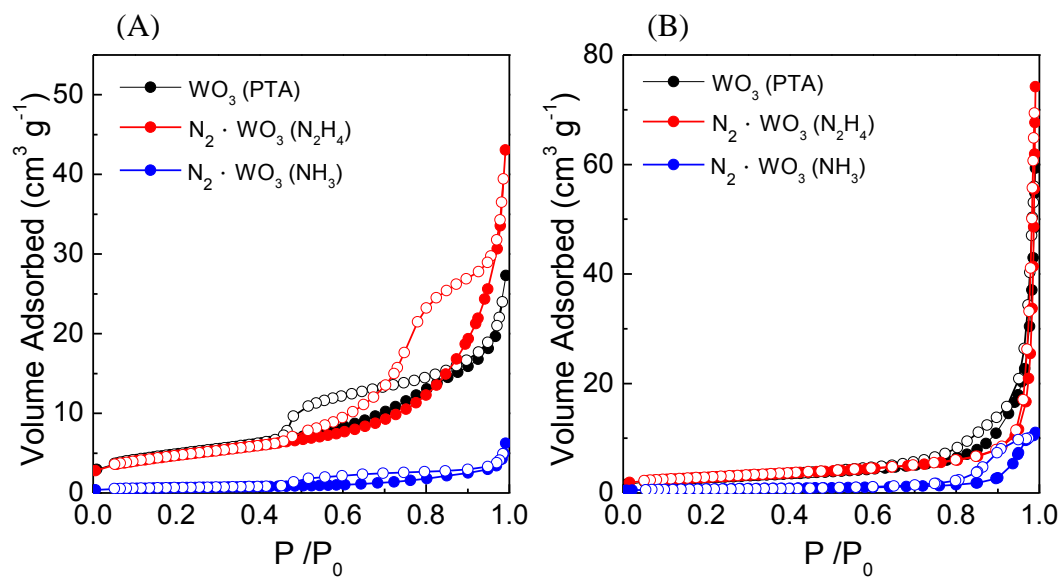


Figure 6-7 N_2 sorption isotherms of neat WO_3 , ammonia-derived $\text{N}_2 \cdot \text{WO}_3$, and hydrazine-derived $\text{N}_2 \cdot \text{WO}_3$ samples calcined at (A) 420°C and (B) 550°C .

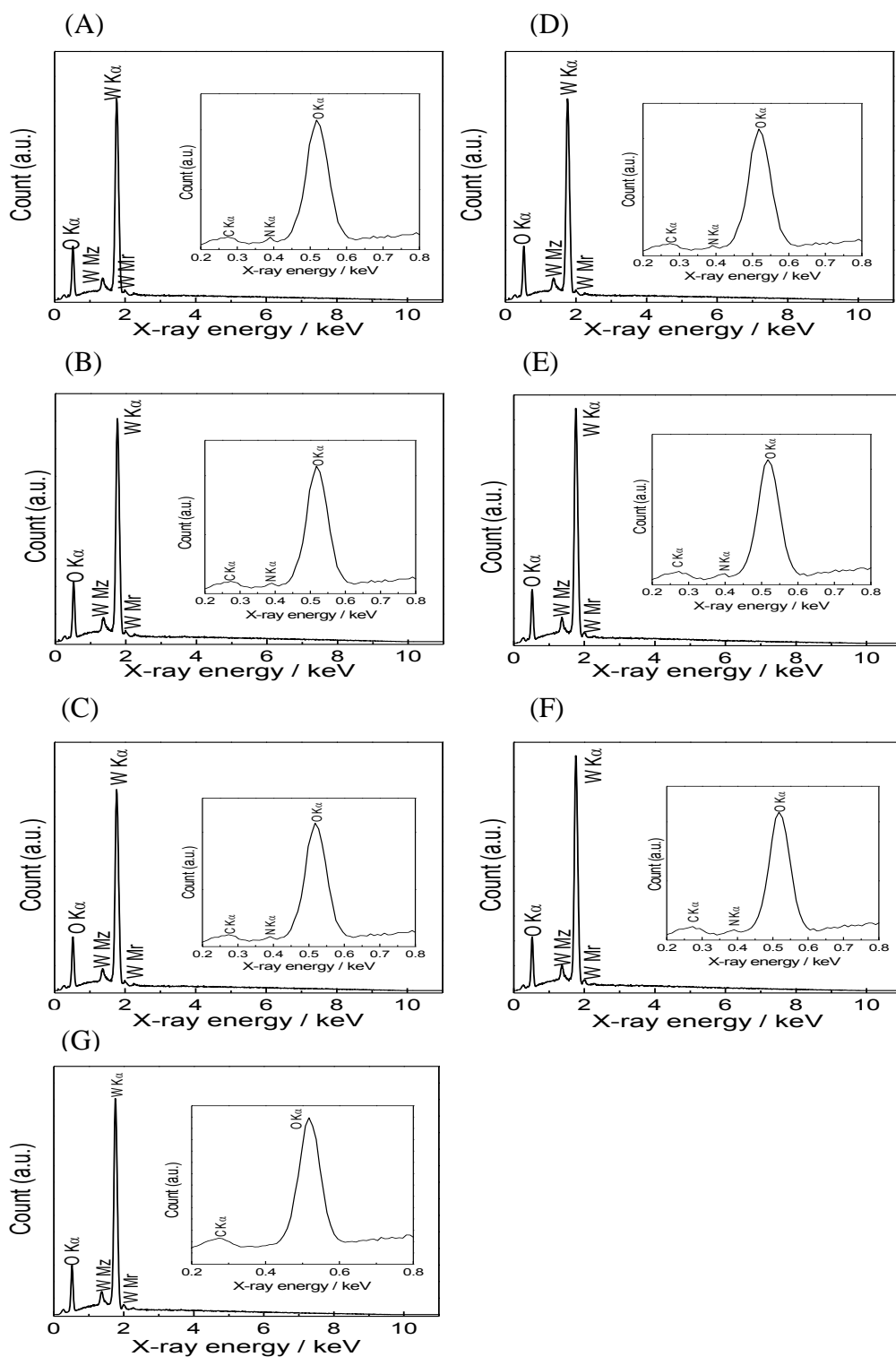


Figure 6-8 EDS data of (A-C) ammonia-derived $N_2.WO_3$ and (D-F) hydrazine-derived $N_2.WO_3$ samples prepared at (A, D) 350 °C, (B, E) 420 °C and (C, F) 550 °C, and (G) Neat WO_3 sample.

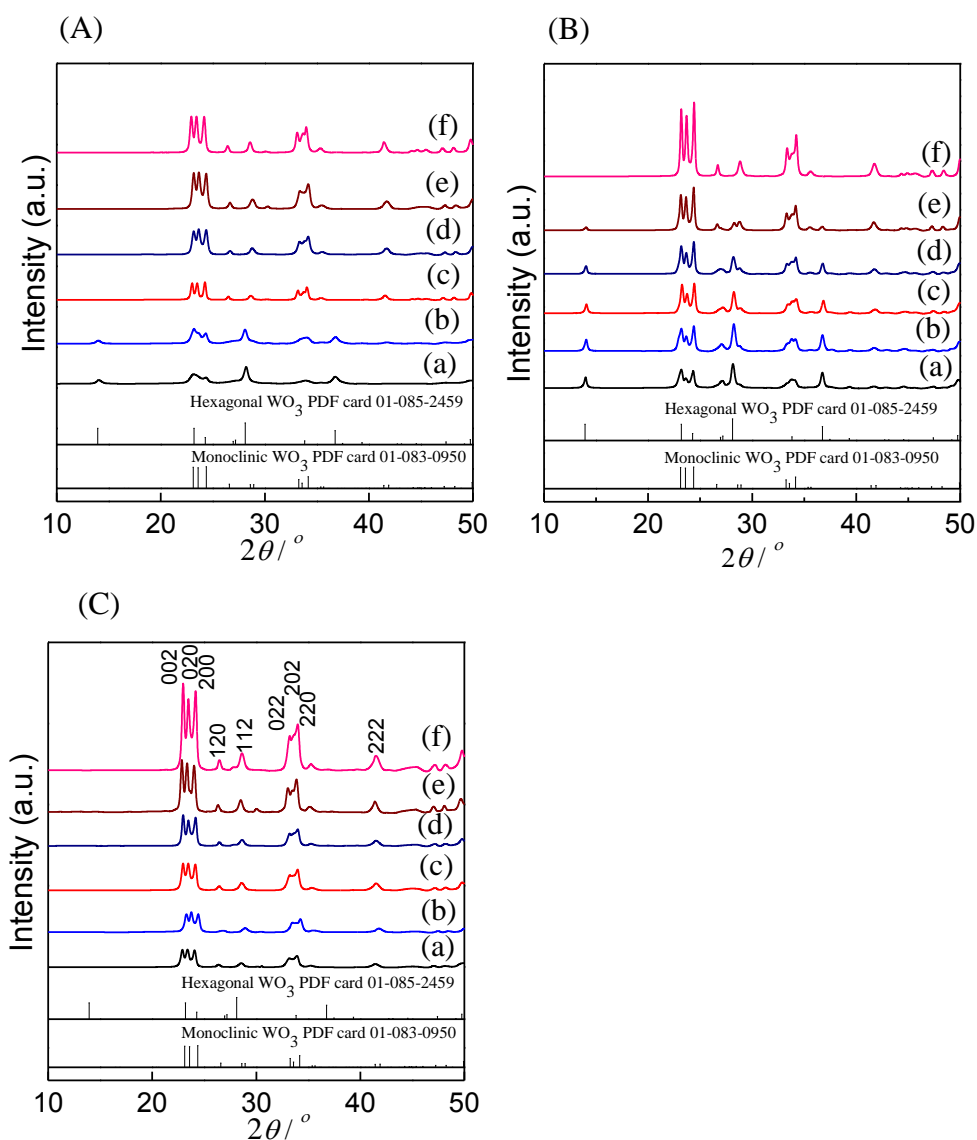


Figure 6-9 XRD patterns of (A) neat WO_3 , (B) ammonia-derived $\text{N}_2 \cdot \text{WO}_3$, and (C) hydrazine-derived $\text{N}_2 \cdot \text{WO}_3$ samples calcined at (a) 350°C, (b) 400°C, (c) 420°C, (d) 450°C, (e) 500°C, and (f) 550°C, respectively.

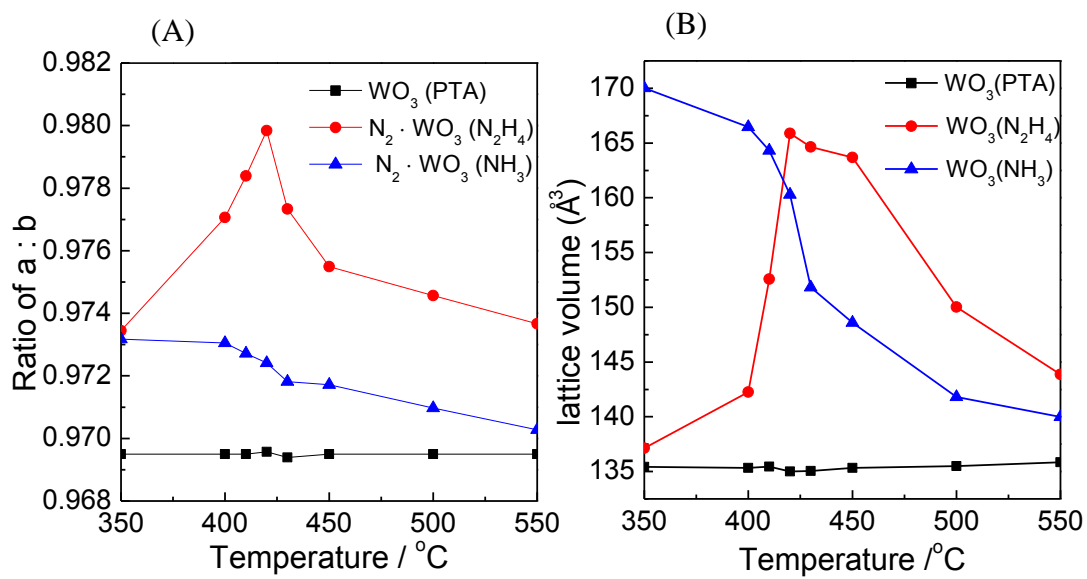


Figure 6-10 The dependency of calcination temperature on (A) the lattice parameters and (B) WO_3 lattice volume. The 002, 020, and 200 peak positions of XRD patterns reflect the a, and b lattice parameters, respectively.

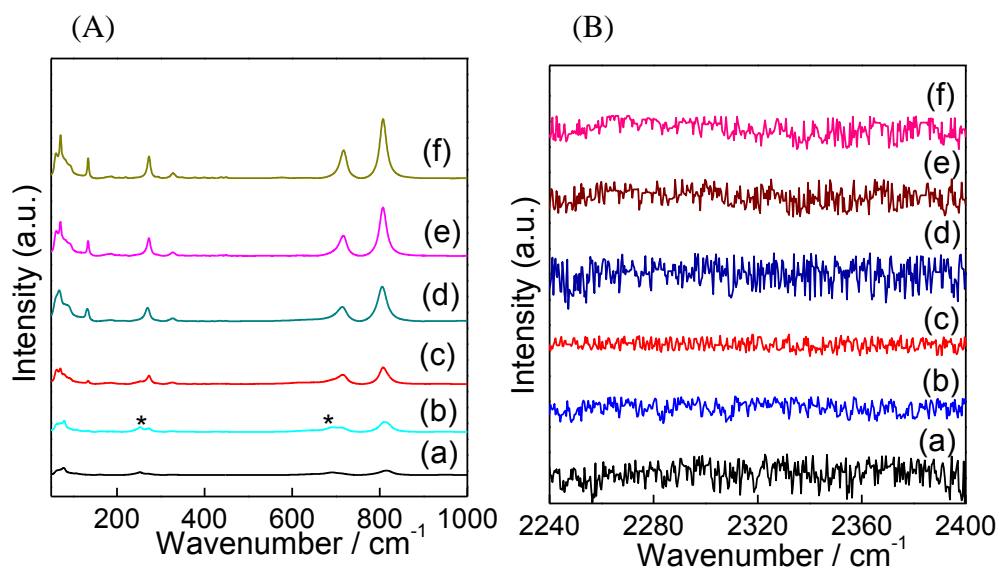


Figure 6-11 Raman spectra of (A) low wavenumber (the peaks marked by asterisk are symbol with hexagonal phase), (B) high wavenumber for neat WO_3 calcined at (a) 350 °C, (b) 400 °C, (c) 420 °C, (d) 450 °C, (e) 500 °C, and (f) 550 °C.

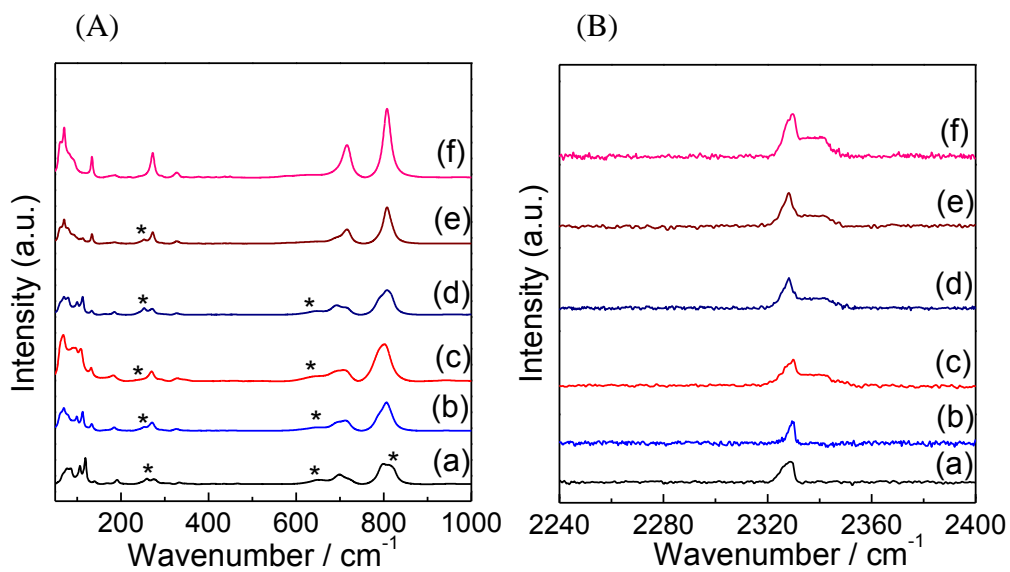


Figure 6-12 Raman spectra of (A) low wavenumber (the peaks marked by asterisk are symbol with hexagonal phase), (B) high wavenumber for ammonia-derived N_2WO_3 calcined at (a) 350 °C, (b) 400 °C, (c) 420 °C, (d) 450 °C, (e) 500 °C, and (f) 550 °C.

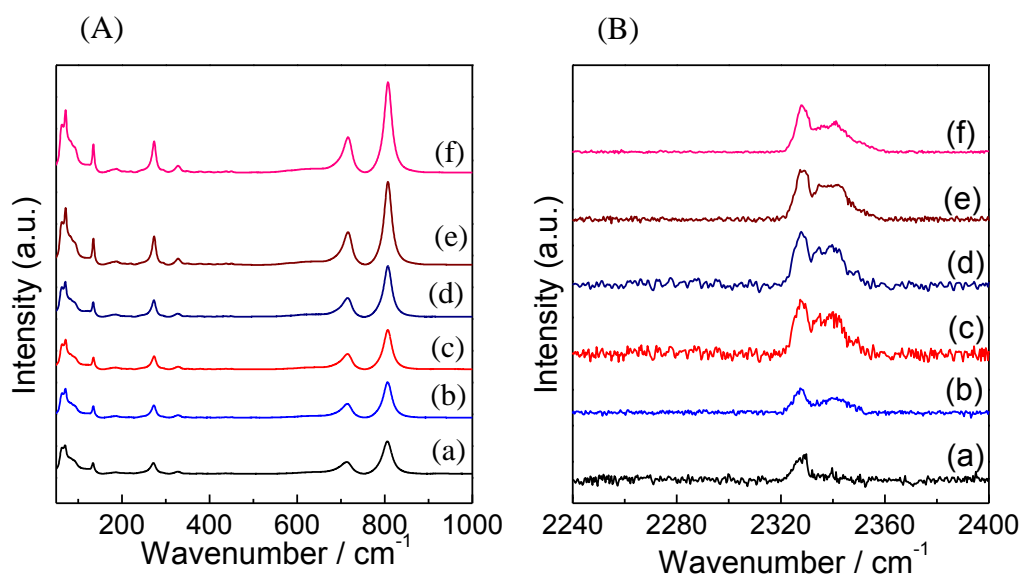


Figure 6-13 Raman spectra (A) low wavenumber, (B) high wavenumber for hydrazine-derived $\text{N}_2 \cdot \text{WO}_3$ samples calcined at (a) 350°C, (b) 400°C, (c) 420°C, (d) 450°C, (e) 500°C, and (f) 550°C.

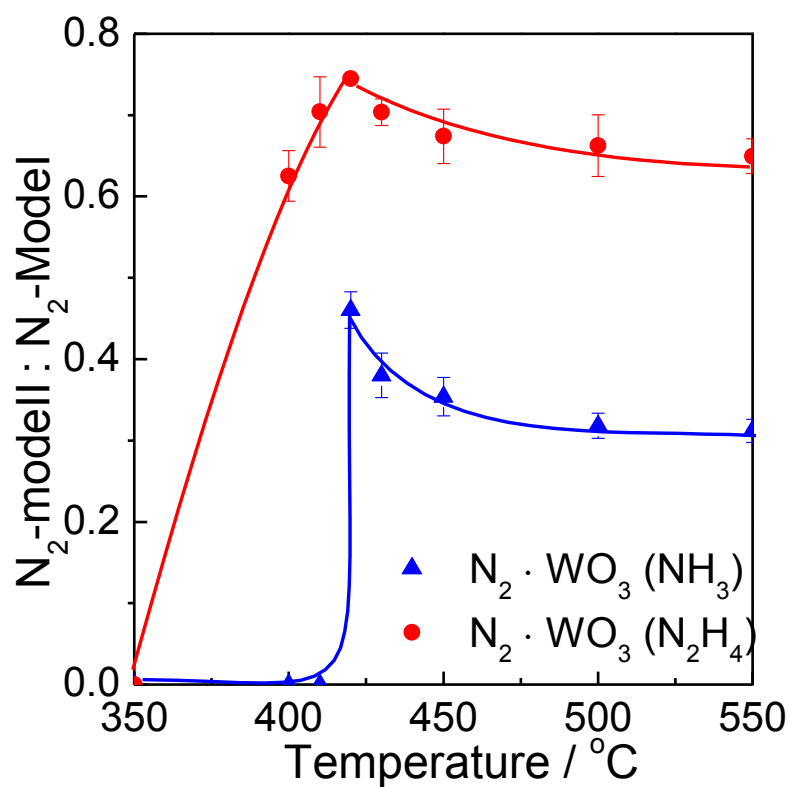


Figure 6-14 The dependency of calcination temperature on the N_2 -ModelII: N_2 -ModelI ratio for ammonia-derived $N_2 \cdot WO_3$ and hydrazine-derived $N_2 \cdot WO_3$ samples. N_2 -ModelII and N_2 -ModelI are corresponding to the peaks at $2328\text{--}2330\text{ cm}^{-1}$ and 2340 cm^{-1} in Raman spectra, respectively. Lines are presented to guide the eye.

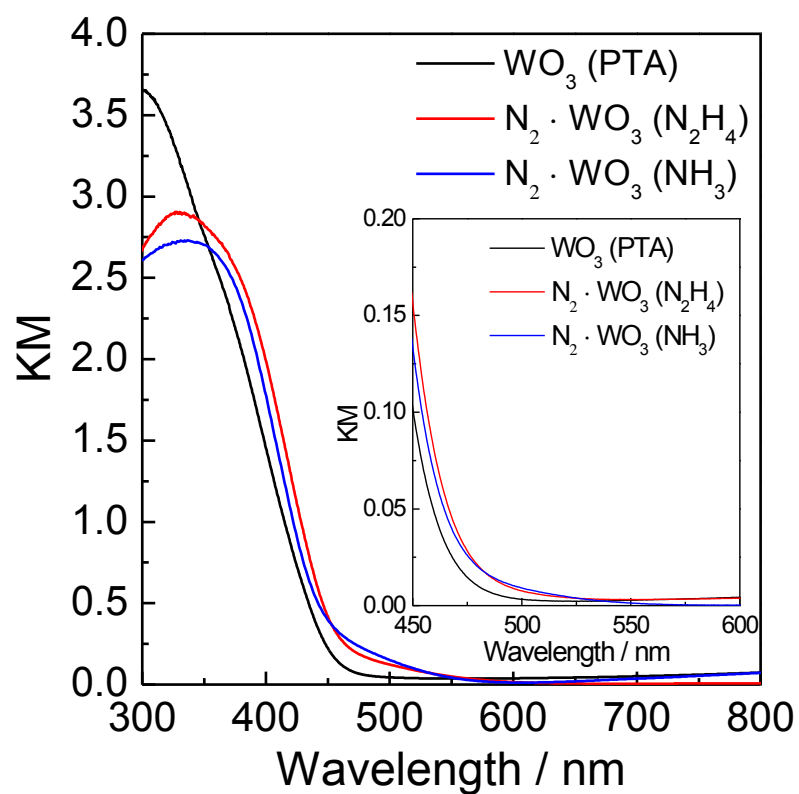


Figure 6-15 DRS of neat WO_3 , ammonia-derived $\text{N}_2 \cdot \text{WO}_3$, and hydrazine-derived $\text{N}_2 \cdot \text{WO}_3$ samples prepared at 420°C and the inset shows the DRS spectra of neat WO_3 , ammonia-derived $\text{N}_2 \cdot \text{WO}_3$, and hydrazine-derived $\text{N}_2 \cdot \text{WO}_3$ samples sintered at 550°C .

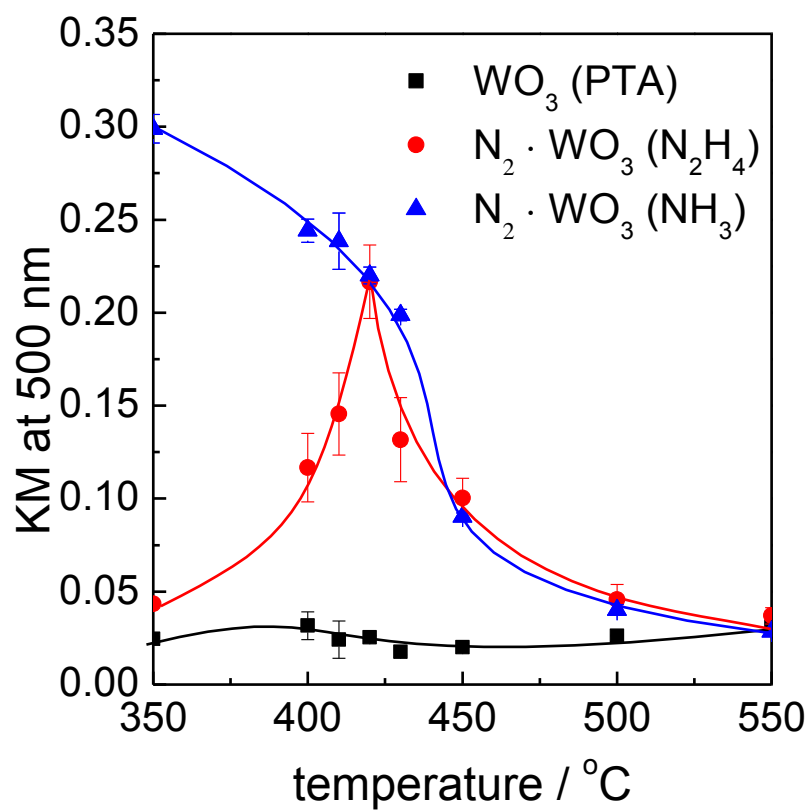


Figure 6-16 Kubelka-Munk (KM) values at 500 nm of neat WO_3 , ammonia-derived $\text{N}_2 \cdot \text{WO}_3$, and hydrazine-derived $\text{N}_2 \cdot \text{WO}_3$ samples sintered at various temperatures. Lines are presented to guide the eye.

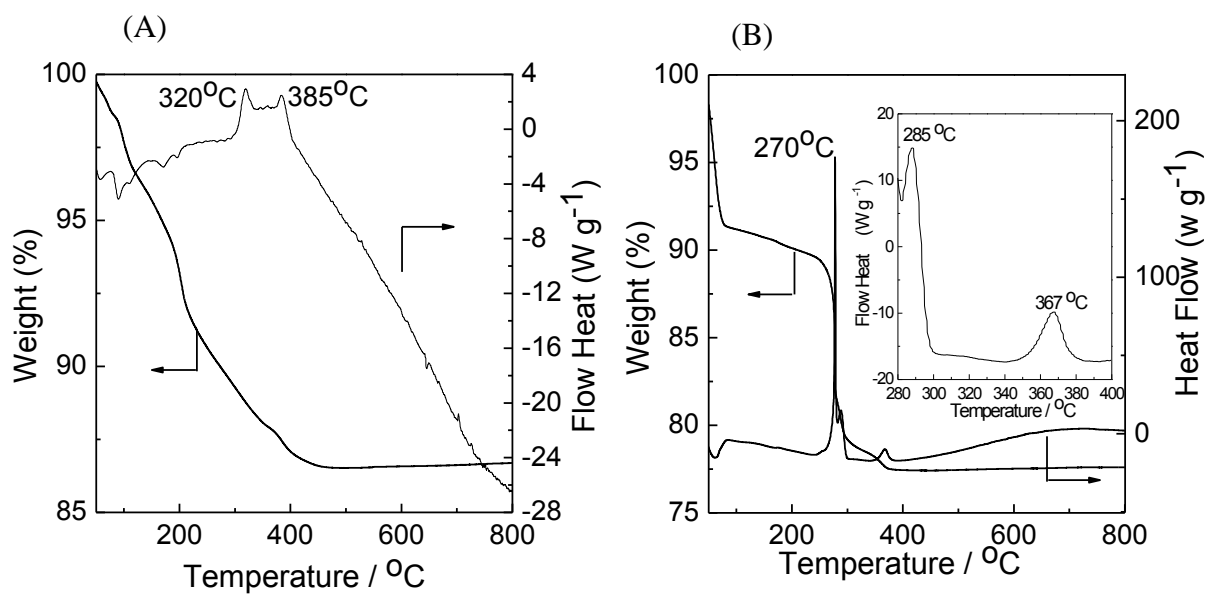


Figure 6-17 TG and DTA curves of (A) ammonia-derived precursor, and (B) hydrazine-derived N_2WO_3 precursor samples.

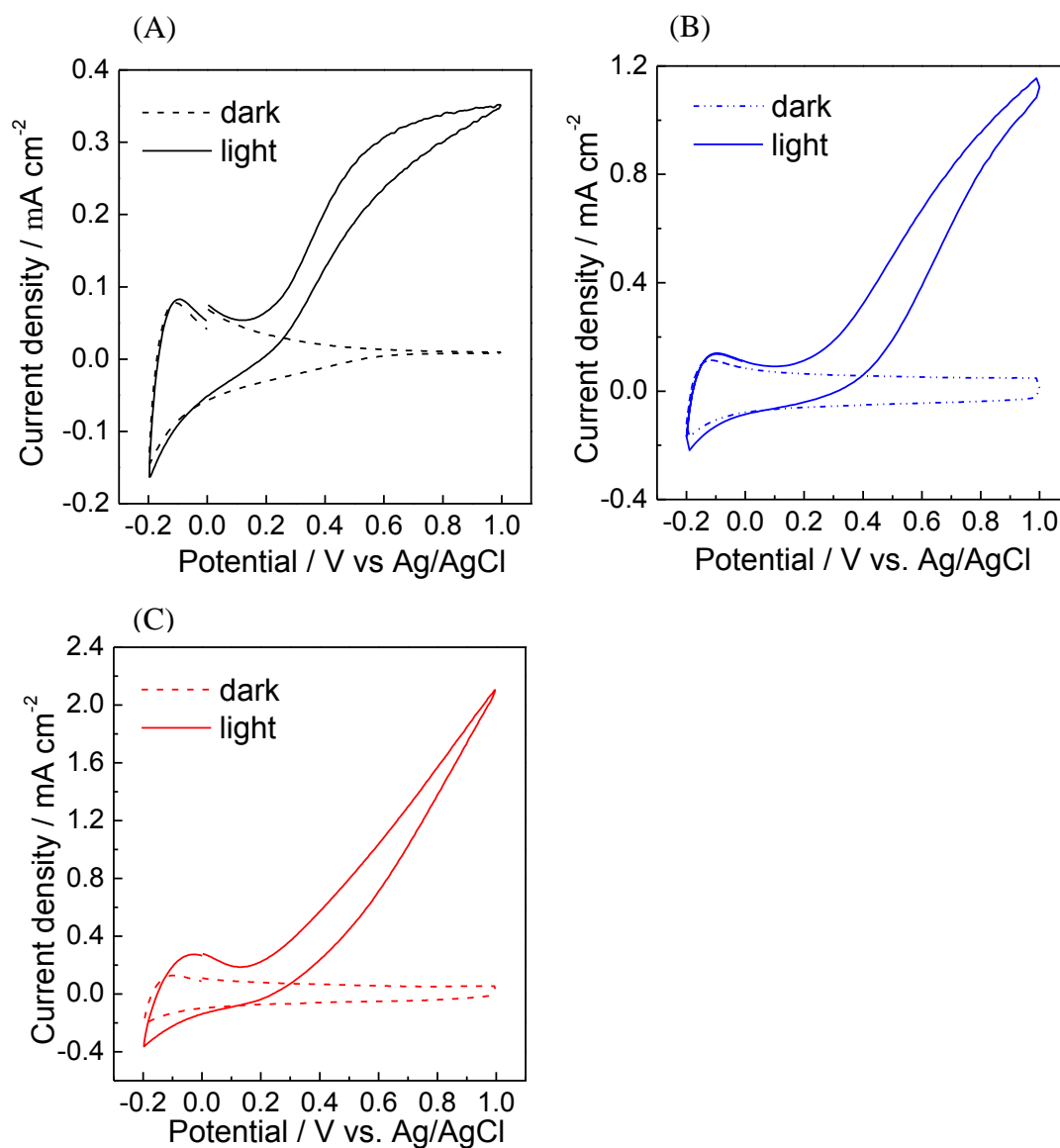


Figure 6-18 Cyclic voltammograms (CVs) of (A) ITO/neat WO_3 , (B) ITO/ammonia-derived $\text{N}_2 \cdot \text{WO}_3$, and (C) ITO/hydrazine-derived $\text{N}_2 \cdot \text{WO}_3$ electrodes calcined at 550°C . CVs were measured in a phosphate buffer (0.1 M, $\text{pH} = 6.0$), the dashed and the solid lines represent CVs measured in the dark conditions and upon illumination of visible light ($\lambda > 390 \text{ nm}$, 100 mW cm^{-2}), respectively.

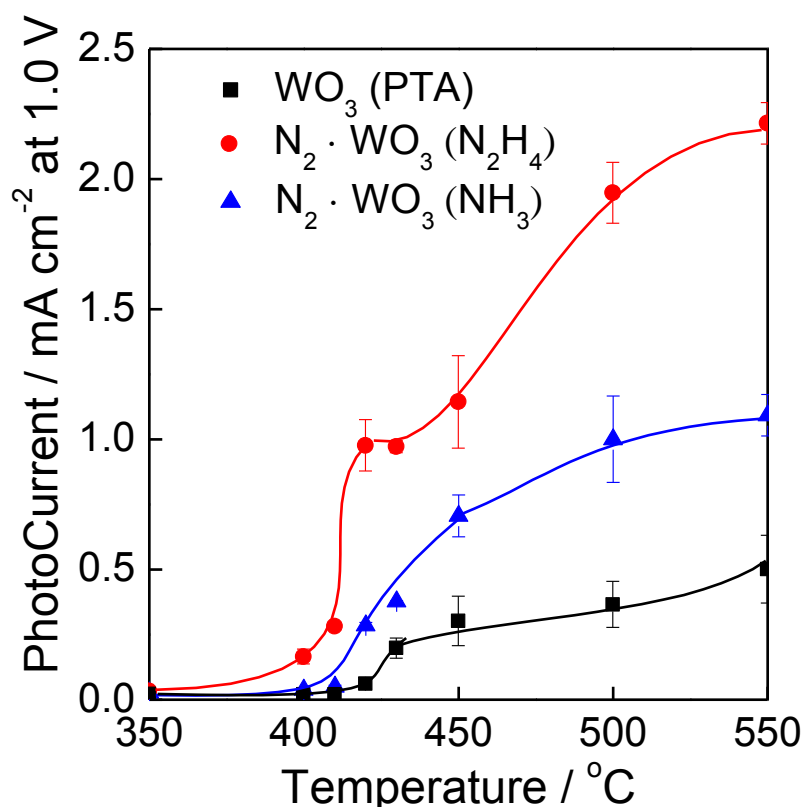


Figure 6-19 The relationship between the calcination temperatures and photocurrent induced by Xe lamp irradiation at 1.0 V vs. Ag/AgCl for ITO/neat WO₃, ITO/ammonia-derived N₂ · WO₃, and ITO/hydrazine-derived N₂ · WO₃ electrodes. Lines are presented to guide the eye.

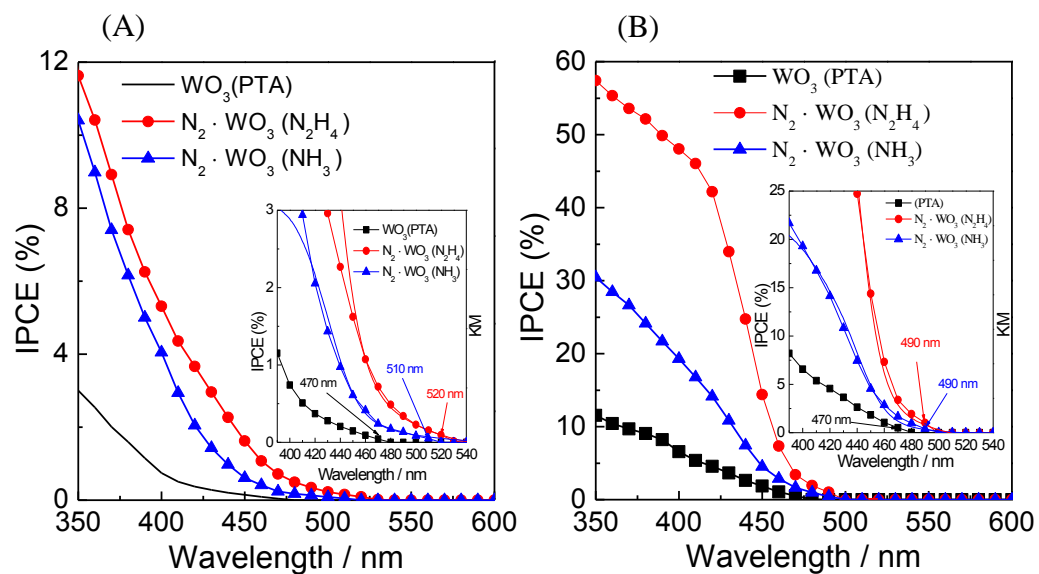


Figure 6-20 Action spectra (plots) of IPCE of ITO/neat WO_3 , ITO/ammonia-derived $\text{N}_2 \cdot \text{WO}_3$, and ITO/hydrazine-derived $\text{N}_2 \cdot \text{WO}_3$ electrodes calcined at (A) 420°C and (B) 550°C. IPCE was measured in a phosphate buffer (0.1 M, pH = 6.0) at 0.5 V vs. Ag/AgCl.

Chapter 7

Concluding remarks

Chapter 7

Concluding remarks

Conclusions Future and prospects

In the first chapter, a nanoporous WO_3 film was prepared on an ITO electrode by a facile, simple and low cost method using commercial WO_3 nanopowder. PEG additive was used as a binder between the WO_3 particles and guided nanoporosity in the film composed of well-connected crystalline WO_3 particles of diameter ~ 100 -200 nm. The WO_3 film worked efficiently as a photoanode for PEC water oxidation and the photoelectrocatalytic performance was further improved by addition of Co^{2+} ions in the electrolyte solution. The WO_3 film is available as a benchmark photoanode for water oxidation required for a PEC water splitting device because a reproducible film is easily prepared without a complicated procedure of precursor preparation, especially for general researcher out of a chemistry field.

In the second chapter, mesoporous WO_3 materials have prepared by a unique and facile solvothermal method using solid H_2WO_4 as a tungsten precursor. DDA was used as a template for the formation of nanostructure, which generates mesoporosity after removing DDA by calcination. The present surfactanttemplate technique is very unique in terms of use of a solid tungsten precursor in a solvothermal method, compared with a common technique using liquid tungsten precursors for interaction with surfactants in principle. The mesoporous network has a disordered arrangement of pores which is composed of well-connected tiny spherical WO_3 particles with a diameter of *ca.* 5 to 20 nm. The DDA-templated WO_3 photoanode showed three times

higher photoanodic current density upon visible light irradiation and provided the efficient performance of PEC water oxidation compared to the untemplated WO_3 , which is promising as an efficient material for high-performance solar energy conversion.

In the fourth chapter, an unique mesoporous N_2 -intercalated WO_3 material was first succeed to synthesize by employing an facile one-step hydrothermal treatment procedure using DDA, which was used as an nitrogen source as well as a surfactant template for formation of mesoporous structure. The N_2 -intercalated mesoporous WO_3 exhibit that this photoanode material was responsive to visible light of $\lambda \leq 490$ nm, which is corroborated the optical band gap (2.5 eV). This band gap of N_2 -intercalated mesoporous WO_3 is narrower compared to the controlled materials (2.8 eV) prepared without a template. And aslo the performance of PEC water oxidation was improved. The action spectra of incident photon-to-current conversion efficiency (IPCE) exhibited that the photoanodic current of N_2 -intercalated mesoporous WO_3 was generated below 490 nm for the N_2 - WO_3 electrodes. This corroborates that the photoanodic current is based on a band gap photoexitation of N 2p-W 5d.

In the fifth and sixth chapter of this thesis, N_2 molecule-Intercalated WO_3 nano-rod photoanodes were successfully prepared by utilizing H_2WO_4 powder and a hydrazine aqueous solution and followed by calcination of the resulted materials. A pure monoclinic N_2 intercalated WO_3 film with higher photocatalytic activity for water oxidation was prepared using a hydrazine aqueous solution as N_2 source instead of an ammonia aqueous solution. Action spectra indicate that the N_2 intercalated WO_3

film prepared from a hydrazine aqueous solution can generate photocurrent below 520 nm. These results could give a guided thought to develop efficient catalysis for water oxidation.

Acknowledgements

First of all, I would like to extend my sincere gratitude to my supervisor, Prof. Masayuki Yagi of Department of Materials Science and Technology, Faculty of Engineering & Center for Transdisciplinary Research, Niigata University, for his instructive advice and useful suggestions on my thesis. Without his patient instruction, insightful criticism and expert guidance, the pletion of this thesis would not have been possible.

I also owe a debt of gratitude to Prof. Tatsuto Yui, and Assistant Prof. Kenji Saito, from whose devoted teaching and enlightening lectures I have benefited a lot and academically prepared for the thesis.

Special thanks should go to Yagi group members who gave me their help and time in listening to me and helping me work out my problems during the difficult course of the thesis. I will always cherish the time we spent together working on various projects.

Dong Li

Appendixes

Publication list

International conference

Publication List

1. **Dong Li**, Debraj Chandra, Kenji Saito, Tatsuto Yui and Masayuki Yagi, Unique and facile solvothermal synthesis of mesoporous WO_3 using a solid precursor and a surfactant template as a photoanode for visible-light-driven water oxidation. *Nanoscale Research Letters*, **2014**, 9:542.
2. Xiaohong Zhang, Debraj Chandra, Masashi Kajita, Hidehito Takahashi, **Li Dong**, Akinori Shoji, Kenji Saito, Tatsuto Yui and Masayuki Yagi, Facile and simple fabrication of an efficient nanoporous WO_3 photoanode for visible-light-driven water splitting. *International Journal of Hydrogen Energy*. **2014**, 39:20736.
3. **Dong Li**, Debraj Chandra, Kenji Saito, Tatsuto Yui, Masayuki Yagi, Preparation of a nano-structure N_2 -Intercalated WO_3 photoanode having highly efficient for Visible-Light-Driven water oxidation. *J. Am. Chem. Soc.*, submitted.
4. **Dong Li**, Debraj Chandra, Kenji Saito, Tatsuto Yui, Masayuki Yagi, Synthesis of N_2 -Intercalated WO_3 using hydrothermal method for water oxidation. *J. Am. Chem. Soc.*, to be submitted.
5. **Dong Li**, Debraj Chandra, Kenji Saito, Tatsuto Yui, Masayuki Yagi, Unique synthesis of mesoporous WO_3 by in-situ N_2 intercalation from surfactant template: Photoanode for Visible-light-driven water oxidation. *J.Mater. Chem.*, to be submitted.
6. **Dong Li**, Debraj Chandra, Kenji Saito, Tatsuto Yui, Masayuki Yagi, Synthesis of a nano-structure WO_3 with high crystalline using a new approach at low temperature for water oxidation. *J.Mater. Chem.*, to be submitted.
7. **Dong Li**, Debraj Chandra, Kenji Saito, Tatsuto Yui, Masayuki Yagi, Unique low temperature crystallization of a mesoporous WO_3 for high efficient visible-light-driven water oxidation. *International Journal of Hydrogen Energy*. to be submitted.

International conference

1) Preparation and efficient visible-light-driven water oxidation of an N₂-intercalation WO₃ nano-structured photoanode (Oral), Dong Li, Debraj Chandra, Kenji Saito, Tatsuto Yui, Masayuki Yagi, Collaborative Conference on Materials Research (CCRM), Incheon (Korea), June 23-27, 2014.

2) Preparation and efficient visible-light-driven water oxidation of an N₂-intercalated WO₃ nano-rod photoanode. (Poster), Dong Li, Debraj Chandra, Kenji Saito, Tatsuto Yui, Masayuki Yagi, 2014 International Conference on Artificial Photosynthesis, Awaji Yumebutai International Conference Center, Awaji City, November 24-28, 2014.